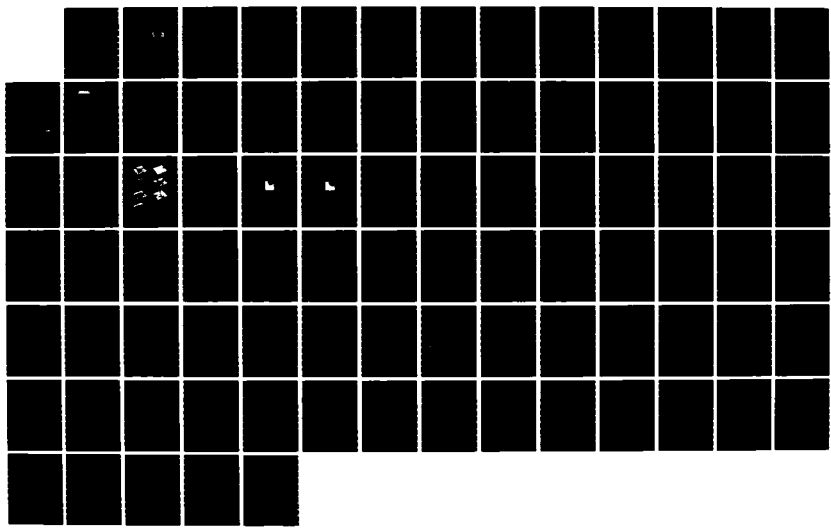


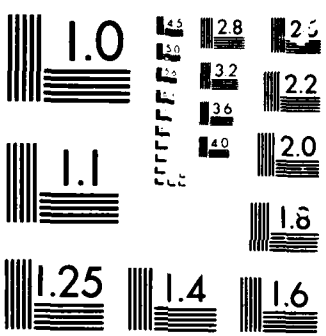
RD-A168 362 A NUMERICAL STUDY OF DIFFRACTION IN REENTRANT GEOLOGIC 1/1
STRUCTURE(U) HEIDLINGER ASSOCIATES PALO ALTO CA
B L MOJCIK ET AL. 15 JUL 85 R-8531 AFGL-TR-85-0158

UNCLASSIFIED F19628-84-C-0182

F/G 8/7

ML





100

AFGL-TR-85-0158

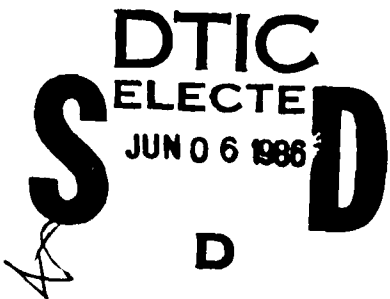
(1)

AD-A168 562

A NUMERICAL STUDY OF DIFFRACTION IN
REENTRANT GEOLOGIC STRUCTURE

Gregory L. Wojcik
Rudolf Mak

Weidlinger Associates
620 Hansen Way
Suite 100
Palo Alto, CA 94304



15 July 1985

Scientific Report No. 1

FILE COPY

APPROVED FOR PUBLIC RELEASE; DISTRIBUTION UNLIMITED.

AIR FORCE GEOPHYSICS LABORATORY
AIR FORCE SYSTEMS COMMAND
UNITED STATES AIR FORCE
HANSCOM AIR FORCE BASE, MASSACHUSETTS 01731

86 6 6 01 Z

CONTRACTOR REPORTS

This technical report has been reviewed and is approved for publication.

Janet C. Johnston

JANET C. JOHNSTON
Contract Manager

H. A. Ossing

HENRY A. OSSING
Chief, Solid Earth Geophysics Branch

FOR THE COMMANDER

D. H. Eckhardt

DONALD H. ECKHARDT
Director
Earth Sciences Division

This report has been reviewed by the ESD Public Affairs Office (PA) and is releasable to the National Technical Information Service (NTIS).

Qualified requestors may obtain additional copies from the Defense Technical Information Center. All others should apply to the National Technical Information Service.

If your address has changed, or if you wish to be removed from the mailing list, or if the addressee is no longer employed by your organization, please notify AFGL/DAA, Hanscom AFB, MA 01731. This will assist us in maintaining a current mailing list.

UNCLASSIFIED

SECURITY CLASSIFICATION OF THIS PAGE

REI

AD-A168 562

Form Approved
OMB No. 0704-0188
Exp. Date: Jun 30, 1986

1a. REPORT SECURITY CLASSIFICATION UNCLASSIFIED		1b. DRAFTING ORGANIZATION REPORT NUMBER(S) R-8531	
2a. SECURITY CLASSIFICATION AUTHORITY		3. DISTRIBUTION/AVAILABILITY OF REPORT Approved public release; distribution unlimited.	
2b. DECLASSIFICATION/DOWNGRADING SCHEDULE		4. PERFORMING ORGANIZATION REPORT NUMBER(S)	
		5. MONITORING ORGANIZATION REPORT NUMBER(S) AFGL-TR-85-0158	
6a. NAME OF PERFORMING ORGANIZATION Weidlinger Associates	6b. OFFICE SYMBOL (If applicable)	7a. NAME OF MONITORING ORGANIZATION Air Force Geophysics Laboratory	
6c. ADDRESS (City, State, and ZIP Code) 620 Hansen Way, Suite 100 Palo Alto, CA 94304		7b. ADDRESS (City, State, and ZIP Code) Hanscom Air Force Base Massachusetts 01731	
8a. NAME OF FUNDING/SPONSORING ORGANIZATION Air Force Geophysics Laboratory	8b. OFFICE SYMBOL (If applicable) AFGL/LW	9. PROCUREMENT INSTRUMENT IDENTIFICATION NUMBER Contract No: F19628-84-C-0102	
8c. ADDRESS (City, State, and ZIP Code) Hanscom Air Force Base Bedford, MA 01731		10. SOURCE OF FUNDING NUMBERS	
		PROGRAM ELEMENT NO. 61102F	PROJECT NO. 2309
		TASK NO. G2	WORK UNIT ASSIGNMENT NO. AR
11. TITLE (Include Security Classification) A Numerical Study of Diffraction in Reentrant Geologic Structure			
12. PERSONAL AUTHOR(S) Gregory L. Wojcik, Rudolf Mak			
13a. TYPE OF REPORT Technical Report No. 1	13b. TIME COVERED FROM 3 Apr 84 to 3 Apr 85	14. DATE OF REPORT (Year, Month, Day) 1985-07-15	15. PAGE COUNT 86
16. SUPPLEMENTARY NOTATION			
17. COSATI CODES		18. SUBJECT TERMS (Continue on reverse if necessary and identify by block number) Reentrant geologic corners; finite element diffraction analysis; topographic structure; mathematical diffraction analysis; mesas and escarpments.	
19. ABSTRACT (Continue on reverse if necessary and identify by block number) <p>The research reported here investigates diffraction effects in complicated geologic and topographic structures of interest to the Air Force Geophysics Laboratory. This first technical report examines diffraction by reentrant corners, i.e., corners with included angle greater than 180 degrees, which idealize the abrupt topographic relief commonly found at the base of escarpments and mesas. Reentrant landforms are also common in tectonic regions, and include fault scarps and other block joints. Approximating these regions of high curvature by perfect edges defines so-called generalized models--where curvature is concentrated at singular points (corners) on the free-surface.</p> <p>Diffraction from a single corner is studied in detail here. Effects of more realistic distributed curvature in local and regional models will be examined in subsequent reports. The principal tool for the study is finite element modeling, since no mathematical solutions presently exist for P-SV wave edge diffraction in even the simplest geologic diffractors. Diffraction of plane P- and SV-waves and a Rayleigh wave are calculated for various</p>			
20. DISTRIBUTION/AVAILABILITY OF ABSTRACT <input type="checkbox"/> UNCLASSIFIED/UNLIMITED <input type="checkbox"/> SAME AS RPT <input type="checkbox"/> DTIC USERS		21. ABSTRACT SECURITY CLASSIFICATION UNCLASSIFIED	
22a. NAME OF RESPONSIBLE INDIVIDUAL Janet C. Johnson		22b. TELEPHONE (Include Area Code) (617) 861-3746	22c. OFFICE SYMBOL AFGL/LWII

UNCLASSIFIED

SECURITY CLASSIFICATION OF THIS PAGE

Abstract (Block 19) Concluded:

reentrant wedges. This necessary emphasis on numerical simulation is balanced in the study by a mathematical analysis of self-similar vector wave diffraction theory. The analysis yields a formal reduction of the general problem to a system of singular integral equations. The resulting integral expressions provide a new calculational basis for solutions to a variety of diffraction problems in mathematical physics.

UNCLASSIFIED

SECURITY CLASSIFICATION OF THIS PAGE

ACKNOWLEDGMENTS

The technical assistance of Patricia George and Penny Slocum (typing), Elizabeth Sevison (graphics) and Myrtle Carey (editing) are gratefully acknowledged.

Accession For	
NTIS CRA&I	<input checked="" type="checkbox"/>
DTIC TAB	<input type="checkbox"/>
Unannounced	<input type="checkbox"/>
Justification	
By _____	
Distribution / _____	
Availability Codes	
Dist	Avail and/or Special
A-1	



CONTENTS

<u>Section</u>		<u>Page</u>
1	INTRODUCTION.....	1
	1.1 INTRODUCTION.....	1
	1.2 BACKGROUND.....	1
	1.3 REPORT PLAN.....	2
2	NUMERICAL STUDY OF DIFFRACTION.....	6
	2.1 INTRODUCTION.....	6
	2.2 FINITE ELEMENT MODEL.....	6
	2.3 DIFFRACTIONS FROM PLANE SH-WAVES.....	7
	2.4 DIFFRACTIONS FROM PLANE SV-WAVES.....	9
	2.5 DIFFRACTIONS FROM RAYLEIGH WAVES.....	10
3	SELF-SIMILAR THEORY OF VECTOR WAVE DIFFRACTION.....	56
	3.1 INTRODUCTION.....	56
	3.2 EQUATIONS GOVERNING THE GENERALIZED DIFFRACTOR.....	56
	3.3 SELF-SIMILARITY AND HOMOGENEOUS VECTOR SOLUTIONS.....	57
	3.4 THE VECTOR BOUNDARY VALUE PROBLEM.....	58
	3.5 CHARACTERISTIC MAPPINGS.....	59
	3.6 REDUCTION OF $F'_+ \pm F'_- = d_\pm$ TO NORMAL FORMS.....	61
	3.7 SOLUTION OF THE NORMAL FORM, $B_+ - B_- = b$	62
	3.8 THE CONSISTENCY CONDITION ON DENSITIES.....	62
	3.9 REDUCTION OF THE BOUNDARY VALUE PROBLEM TO AN INTEGRAL EQUATION.....	63
	3.10 THE CANONICAL PROBLEM, $N = 2$	65
4	DISCUSSION AND CONCLUSION.....	71
	4.1 OVERVIEW.....	71
	4.2 NUMERICAL DIFFRACTION EXPERIMENTS.....	71
	4.3 THEORY OF VECTOR WAVE DIFFRACTION.....	73
	4.4 CONCLUSIONS.....	75
	REFERENCES.....	76

ILLUSTRATIONS

<u>Figure</u>		<u>Page</u>
1-1	Examples of erosional and tectonic landforms with reentrant features.....	3
1-2	Illustrations of a) highland-lowland erosional topography showing a typical mesa cross-section; b) idealized topography showing rays from a surface source on the lowland and its highland geometric shadow zone; c) diffractions from the corners illuminating receivers in the shadow zone.....	4
1-3	A sequence of snapshots from finite element simulations of Rayleigh surface wave reflection, transmission and diffraction in four reentrant corners. The Rayleigh wave is incident from the right, and each sequence shows vector plots of the velocity field at 50 timestep increments, starting when the surface wave reaches the corner at timestep = 250....	5
2-1	Baseline finite element model for 2-D slice of an idealized mesa or escarpment base.....	11
2-2	Diffracted wavefronts for an SH-wave incident from below at times T_1 and T_2 , where $T_2 > T_1$	12
2-3	Comparison of Keller-Blank and FLEX solution for SH-wave incident from below to 90-degree mesa.....	13
2-4	Comparison of Keller-Blank and FLEX solution for SH-wave incident to 70-degree mesa.....	14
2-5	Comparison of Keller-Blank and FLEX solutions for SH-wave incident to 45-degree mesa.....	15
2-6	Comparison of Keller-Blank and FLEX solutions for SH-wave incident to 20-degree mesa.....	16
2-7	Comparison of Keller-Blank and FLEX solutions for SH-wave incident to 90-degree mesa, offset 45 degrees...	17
2-8	Comparison of Keller-Blank and FLEX solutions for SH-wave incident to 90-degree mesa, offset 22.5 degrees..	18
2-9	Surface plots of diffraction for SH-wave incidence on 90-degree mesa, offset 22.5 degrees.....	19
2-10	Comparison of Keller-Blank and FLEX solutions for geometry shown in Fig. 2-8, 40 Hz SH wavelet input....	20
2-11	Comparison of Keller-Blank and FLEX solutions for geometry shown in Fig. 2-8, 40 Hz SH wavelet input, coarse grid.....	21

ILLUSTRATIONS (continued)

<u>Figure</u>		<u>Page</u>
2-12	Comparison of Keller-Blank and Flex solutions for the geometry in Fig. 2-4, 40 Hz SH wavelet input, coarse grid, skewed elements.....	22
2-13	Diffractons for P-wave incidence from below for different geometries.....	23
2-14	Time histories of diffracted field for P-wave incidence from below to 90-degree mesa.....	24
2-15	Time histories of diffracted field from P-wave incidence to 70-degree mesa.....	25
2-16	Time histories of diffracted field from P-wave incidence to 45-degree mesa.....	26
2-17	Time histories of diffracted field from P-wave incidence to 20-degree mesa.....	27
2-18	Time histories of diffracted field from P-wave incidence to 90-degree mesa, offset 45 degrees.....	28
2-19	Time histories of diffracted field from P-wave incidence to 90-degree mesa, offset 22.5 degrees.....	29
2-20	Vector plots of diffraction from P-wave incidence at time 0.06158 s for 90-degree mesa.....	30
2-21	Diffractons from P-wave incidence at time 0.07698 s for 90-degree mesa.....	31
2-22	Diffractons from P-wave incidence for 90-degree mesa, offset 45 degrees.....	32
2-23	Diffracton from P-wave incidence at time 0.06158 s for 90-degree mesa, offset 22.5 degrees, showing center portion of grid.....	33
2-24	Diffractons from P-wave incidence on 70-degree mesa.....	34
2-25	Diffractons for SV-wave incidence from below for different geometries.....	35
2-26	Time histories of diffracted field for SV-wave incidence from below to 90-degree mesa.....	36
2-27	Time histories of diffracted field for SV-wave incidence to 70-degree mesa.....	37

ILLUSTRATIONS (continued)

<u>Figure</u>		<u>Page</u>
2-28	Time histories of diffracted field from SV-wave incidence to 45-degree mesa.....	38
2-29	Time histories of diffracted field from SV-wave incidence to 20-degree mesa.....	39
2-30	Time histories of diffracted field from SV-wave incidence to 90-degree mesa, offset 45 degrees.....	40
2-31	Time histories of diffracted field from SV-wave incidence to 90-degree mesa, offset 22.5 degrees.....	41
2-32	Diffractions at time 0.09238 s for SV-wave incidence to 90-degree mesa, offset 45 degrees.....	42
2-33	Diffractions at time 0.1078 s from SV-wave incidence to 90-degree mesa, offset 45 degrees.....	43
2-34	Diffraction at time 0.09238 s from SV-wave incidence to 90-degree mesa, offset 22.5 degrees, showing center position of grid.....	44
2-35	Diffraction from SV-wave incidence to 45-degree mesa...	45
2-36	Diffraction at time 0.09238 s from SV-wave incidence to 20-degree mesa.....	46
2-37	Time histories of diffracted field from Rayleigh wave incidence to 90-degree mesa.....	47
2-38	Time histories of diffracted field from Rayleigh wave incidence to 70-degree mesa.....	48
2-39	Time histories of diffracted field from Rayleigh wave incidence to 45-degree mesa.....	49
2-40	Time histories of diffracted field from Rayleigh wave input to 20-degree mesa.....	50
2-41	Reference field for Rayleigh wave incidence showing waves generated by wavelet loading over 5 nodes on 200 x 100 nodes halfspace.....	51
2-42	Diffractions from Rayleigh wave incidence to 90-degree mesa showing full wave field for center portion of grid.	52
2-43	Diffractions from Rayleigh wave incidence to 70-degree mesa showing full wave field for center portion of grid.	53
2-44	Diffractions from Rayleigh wave incidence to 45-degree mesa showing full wave field for center portion of grid	54

ILLUSTRATION (concluded)

<u>Figure</u>		<u>Page</u>
2-45	Diffractions from Rayleigh wave incidence to 20-degree mesa showing full wave field for the center position of the grid.....	55
3-1	The generalized plane diffractor, consisting of M semi-infinite wedges formed by directed lines from the vertex. The lines (interfaces) are designated by their polar angles, L_m , $m = 1, M$	68
3-2	a) Definition of contour C bounding the limit points at $r = 0$ and ∞ ($\arg \epsilon = 0$); b) Cartoon of the complete set of limit points defining the generalized diffractor.....	69
3-3	Mapping of the wave domain, Ω into the z_+ plane by the characteristic transformation.....	70
3-4	Mapping of the wave domain, Ω to the upper half-plane by conformal transformation, $w(z_+)$	70

SECTION 1

INTRODUCTION

1.1 INTRODUCTION

The purpose of this research is to investigate diffraction effects in complicated geologic and topographic structures of interest to the Air Force Geophysics Laboratory. This first technical report examines diffraction by reentrant corners, i.e., corners with included angle greater than 180 degrees, which idealize the abrupt topographic relief commonly found at the base of escarpments and mesas. Reentrant landforms are also common in tectonic regions, and include fault scarps and other block joints. These erosional and tectonic features are nicely illustrated in Fig. 1, reproduced collectively from Holmes (1965), showing near-surface structural variations at both local and regional scales. Approximating these regions of high curvature by perfect edges defines so-called generalized models--where curvature is concentrated at singular points (corners) on the free-surface. Diffraction from a single corner will be studied in detail here. Effects of more realistic distributed curvature in local and regional models will be examined in subsequent reports.

The principal tool for the study is finite element modeling, since no mathematical solutions presently exist for P-SV wave edge diffraction in even the simplest geologic diffractors. This necessary emphasis on numerical simulation is balanced in the study by a mathematical analysis of self-similar vector wave diffraction theory. The analysis yields a formal reduction of the general problem to a system of singular integral equations. The resulting integral expressions provide a new calculational basis for solutions to a variety of diffraction problems in mathematical physics.

1.2 BACKGROUND

Motivation for this study is the observation that highland interiors are often in the shadow zone of lowland seismic sources. Consequently, diffracted waves from surfaces of high curvature (e.g., edges and corners) provide the dominant seismic signals detected in the interior. In other words, edges and corners on the free surface act as secondary sources illuminating the highland interior. This is illustrated in Fig. 2, showing a cartoon of the highland-lowland topography, source generated rays and the geometric shadow zone, and diffraction (secondary) sources. Numerical calculations of the full wave field are necessary to simulate this phenomenon

because approximate theories, such as conventional ray tracing and boundary integral methods, cannot accommodate diffraction from irregular boundaries. However, questions remain regarding the range of validity of numerical diffractions, due in large part to the existence of certain singularities (stress concentrations) at reentrant corners (geometric singularities).

The geophysical problem is best illustrated by some finite element examples modeling reentrant wedges of elastic rock diffracting an incident Rayleigh wavelet. Snapshots of the full wave field are shown in Fig. 3, for Rayleigh wave incidence from the right. Each wedge simulates the lower edge of an escarpment, and the Rayleigh wave represents ground roll from a vibratory surface source located 100 meters (100 elements) from the edge. Although the escarpment is in the source's geometric shadow, clearly surface wave interaction with the corner radiates significant body wave energy into the highland interior. Furthermore, the Rayleigh wavelet is seen to transmit effectively around the corner, hence, will radiate into the interior at each encounter with subsequent corners on the free surface.

1.3 REPORT PLAN

Results of the research are presented in the following three sections. Section 2 describes the numerical diffraction experiments, Section 3 develops the mathematical theory of vector wave diffraction and Section 4 presents the discussion and conclusions. The numerical work in Section 2 was done principally by the second author. The first author was responsible for the remaining research and written report.

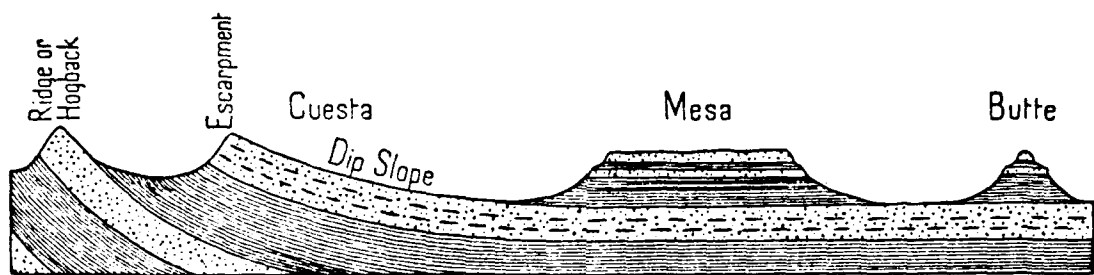


FIG. 413 Diagram to illustrate the relation of various erosional landforms to the structure and dip of the strata from which they have been carved

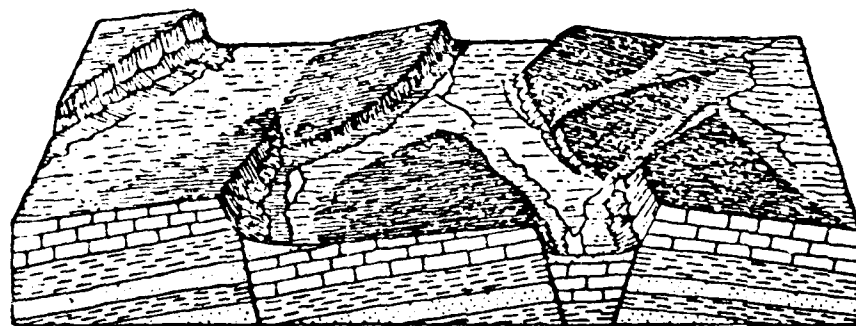


FIG. 796 Diagram to illustrate the fault-block structure of the ranges of the Great Basin, Utah
(After W. M. Davis)



FIG. 791 Schematic section across the Cordillera of the western United States.
Length of section about 1,900 miles (3,000 km.)

Figure 1-1. Examples of erosional and tectonic landforms with reentrant features. The upper two diagrams are at local scales (1-100km) while the bottom section is on a regional scale (1000-3000km). These illustrations with captions are reproduced directly from Holmes (1965).

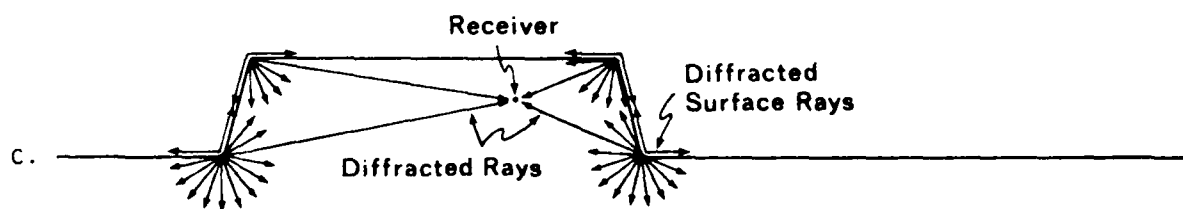
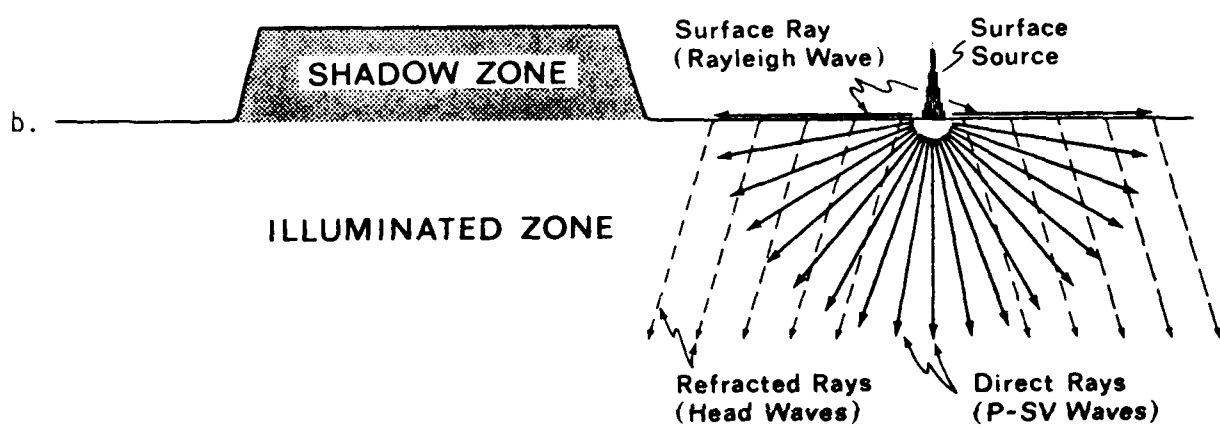


Figure 1-2. Illustrations of a) highland-lowland erosional topography showing a typical mesa cross-section; b) idealized topography showing rays from a surface source on the lowland and its highland geometric shadow zone; c) diffractions from the corners illuminating receivers in the shadow zone.

10^{-7} m/s

Timestep = 250 Timestep = 300 Timestep = 350 Timestep = 400

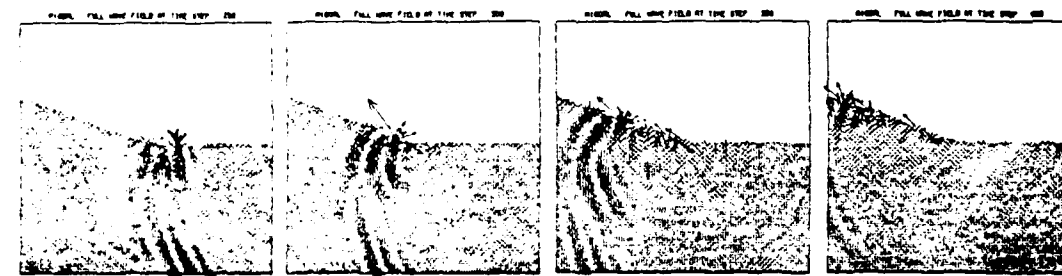
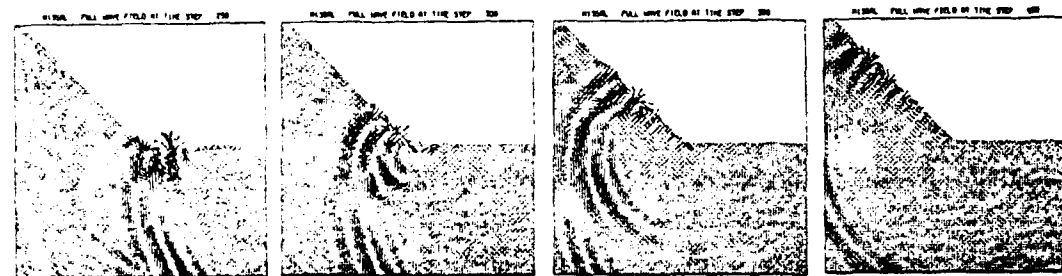
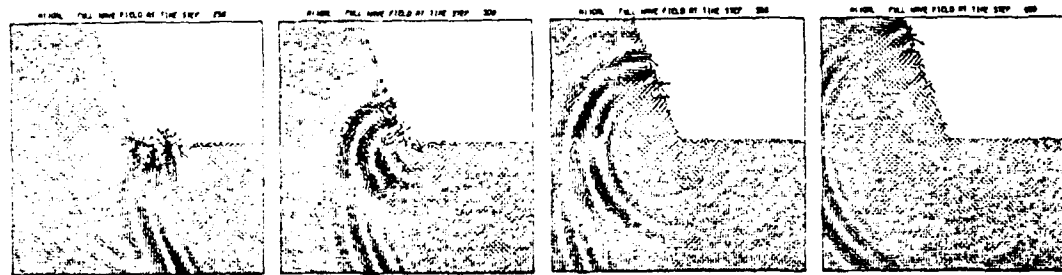
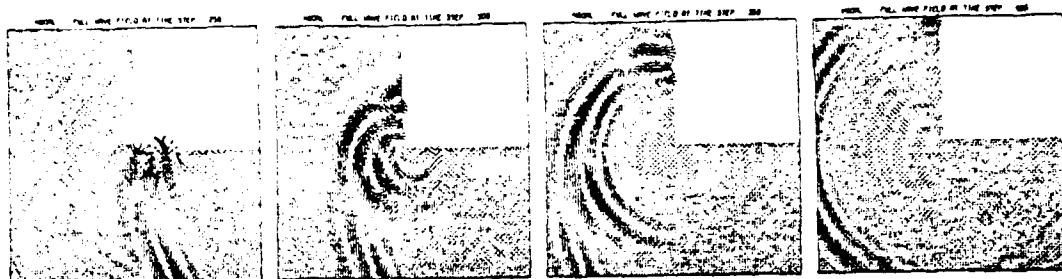


Figure 1-3. A sequence of snapshots from finite element simulations of Rayleigh surface wave reflection, transmission and diffraction in four reentrant corners. The Rayleigh wave is incident from the right, and each sequence shows vector plots of the velocity field at 50 timestep increments, starting when the surface wave reaches the corner at timestep = 250 (leftmost figure).

SECTION 2 NUMERICAL STUDY OF DIFFRACTIONS

2.1 INTRODUCTION

The numerical analysis of diffraction from reentrant corners is performed using the finite element method. Plane P-, SV- and SH-waves and a Rayleigh surface wave are incident on reentrant corners with angles typical of mesas and escarpments. The SH-waves have particle motions perpendicular to the plane of the mesa structure, while P-SV waves have in-plane particle motions. The Rayleigh waves have in-plane particle motions with their characteristic retrograde elliptical orbits and exponential decay with depth. The resulting diffracted fields are then examined quantitatively.

Section 2.2 outlines the finite element model used for the computations. Section 2.3 discusses diffractions for SH-wave input. Results for P-SV-wave input are shown in Section 2.4, while Section 2.5 concludes with the results for Rayleigh wave input.

2.2 FINITE ELEMENT MODEL

The numerical computations are made with FLEX, an explicit time integration finite element code, Vaughan (1984). The baseline finite element model is a 199 meter by 199 meter cross-section of a mesa edge with a 199 by 199 element discretization of 1 meter square elements, Fig. 2-1. The material is linearly elastic with $c_p = 2600 \text{ m/sec}$, $c_s = 1500 \text{ m/sec}$ and $\rho = 2000 \text{ kg/m}^3$. Frequency resolution of the model is about 160 Hz. Reentrant angles are modeled by cutouts in the first and second quadrants with the vertex at the center of the grid. Note that definition of the mesa by square elements produces a stepped interface for most of the reentrant angles considered.

Body waves are input from the bottom of the grid, the left and right sides having appropriate symmetry or asymmetry boundary conditions for P- or SV-waves, respectively. Rayleigh surface waves are generated by prescribing vertical velocity over five nodes (four elements) along the x-axis, Fig. 2-1, with a symmetry condition on the right side and an absorbing boundary on the other three sides. All wave types are input as nodal velocity-time histories of the wavelet function, $F = A \cdot \text{EXP}(-(\omega T/\alpha)^2) \cos(\omega T + v)$, where A is amplitude, ω is predominant wavelet frequency, α approximates the number of cycles in the wavelet, v is the phase shift and T is time shifted by half the wavelet duration.

A unit amplitude wavelet with 80 Hz predominant frequency, zero phase shift and $\alpha = 4$ is used to define the input wave fields. A reference model with the same wavelet input to a halfspace (199 m by 199 m with no cutouts) provides the incident field. The diffracted field is obtained by subtracting the incident from the full field. Output consists of time histories of the diffracted field at points around the vertex and snapshots of nodal velocities at selected times.

2.3 DIFFRACTION FROM PLANE SH-WAVES

SH-waves are relatively unimportant in mesa applications compared to P-SV-waves because surface sources are seldom of SH type. Yet scalar SH-waves have the advantage that analytic diffraction solutions are available, whereas no solution is available for P-SV diffraction. To investigate validity of the finite element solutions, especially effects of the stepped interface produced by square elements, diffractions from SH-waves are studied and compared with the analytic solution.

The closed-form solution for SH incidence to wedges is available from Keller and Blank (1950) in terms of algebraic and trigonometric functions of radial distance from the vertex, wave speed and time. Keller and Blank use a step function as the input wave. To obtain the diffracted field for a wavelet input, the analytic solution is convolved with the wavelet time function.

Figure 2-2 shows sketches of wavefronts in the diffracted field for several wedge angles. The calculated field consists of two components, reflections off the two interfaces and a circular diffracted wave from the vertex. For certain regions of the mesa, such as points A and B in Fig. 2-2, the diffracted field has both components with the circular portion lagging behind. Thus, the time of arrival is controlled by the reflected component, not by the circular component as intuition would suggest. This is confirmed by the finite element solution.

To simulate 2-D plane SH waves, symmetric boundary conditions are enforced on both the left and right side. The diffracted field from the finite element analysis is cross-plotted against the Keller-Blank solutions in

Figs. 2-3 to 2-8 for various reentrant angles. It is obvious that the finite element solution agrees very well with the analytic solution. When the interface is inclined at angles which give a smooth stepped interface (such as 0, 45 and 90 degrees), the finite element model gives very good results. For other angles with a less uniform stepped interface, the finite element model is able to capture the predominant wavelet diffraction but generates some oscillation at late time. The amplitude of this oscillation appears to be a direct function of distance from the stepped interface.

Figure 2-9 shows snapshots of the finite element solution for the geometry shown in Fig. 2-8. Both the full wave field and the diffracted field are plotted.

To investigate the nature of the late-time oscillation, a numerical study with the same finite element model but a lower frequency (40 Hz) wavelet is made. The geometry giving the worst oscillation (Fig. 2-8) is used. Figure 2-10 shows the diffracted field for the lower frequency wavelet input. The late-time oscillation is reduced significantly.

To further illustrate the dependence of the oscillation on the frequency content of the input wavelet, another computation is made with a coarse grid of 2 m square elements and 40 Hz wavelet input. The frequency resolution of this coarse grid model is about 80 Hz. Again, the input wavelet has a frequency of about half the resolution of the grid. The late-time oscillation is very evident, as illustrated in Fig. 2-11.

Finally, a finite element model with the coarse grid and skewed elements is used. The skewed elements eliminate the stepped interface but impose severe time-step size constraints for interfaces inclined at angles close to 45 degrees. Figure 2-12 compares the diffracted field from the skewed elements to the Keller-Blank solution. Again, the late-time oscillation is reduced drastically. This clearly shows the relationship of the oscillation to the stepped interface.

This study shows that finite element modeling with square elements can capture the predominant response of the diffracted field. The stepped interface does, however, introduce some oscillation to the late-time solution. Whereas the finite element grid can be used to resolve up to 160 Hz for regular wave propagation analysis, the singularity of the diffracted field causes

a slight degradation of the late-time solution for an 80 Hz input. The finite element solution gives better results as the frequency of the input is lowered. A lower frequency wavelet has a longer wave length and the incoming, reflected and diffracted wave trains will interfere with one another on the time history plots, making interpretation difficult. All subsequent body wave calculations will be made with the baseline model of 1 m square elements subjected to an 80 Hz wavelet input.

2.4 DIFFRACTIONS FROM PLANE P-SV WAVES

The diffracted field from a vector (P-SV) field is more complex than that from a scalar field. Incident field polarized as pure P-wave (where the particle motions are in the direction of wave propagation) or pure SV-wave (particle motions perpendicular to direction of wave propagation) generates both P and SV components in the diffracted field. The analysis will consider first diffractions for P-wave incidence.

A two-dimensional plane strain model is used to simulate planar P-waves with symmetry conditions imposed on both the left and right boundaries. Diffracted wavefronts are shown in Fig. 2-13. Note that the diffracted field is more complicated than for the SH case shown in Fig. 2-2. Both P- and SV-waves are reflected off inclined interfaces according to Snell's law. Diffraction from the vertex has both P and SV circular fronts propagating at their respective wave speeds. Of course, only the P-wave is reflected at normal incidence (horizontal interface). Figures 2-14 to 2-19 are cross plots of the x and y components of the diffracted solution. Figures 2-20 to 2-24 show vector plots of the diffracted field for different geometries. Note that most of the vector plots show only the center 100 by 100 m portion of the grid.

For the SV incident case, asymmetric boundary conditions are used in the left and right sides. Figure 2-25 shows wavefronts of the diffracted field. Only an SV wave is reflected for SV incidence beyond the critical value. This is illustrated in the bottom sketch in Fig. 2-25. Diffraction from the vertex has both P and SV components. Figures 2-26 to 2-31 are cross plots of x and y components of the diffracted solution. Note the different time scale to accommodate the slower incident SV-wave and the new legend for x and y components of velocity. Figures 2-32 to 2-35 show vector plots of the diffracted field for different geometries.

2.5 DIFFRACTIONS FROM RAYLEIGH WAVES

Rayleigh waves are generated by applying a vertical velocity over five nodes along the x-axis, see Fig. 2-1. The same two-dimensional plane strain model is used. The boundary conditions are symmetry on the right and absorbing on the other three sides. In addition to Rayleigh waves, the normal velocity input generates P- and SV-waves, although at a much lower amplitude. The P-wave speed of 2600 m/sec is much higher than that of the Rayleigh wave (at 1440 m/sec, 96 percent of SV wave speed). Thus, arrival of P and Rayleigh waves at the vertex will be well separated. The Rayleigh wave can be distinguished from the SV-wave by its retrograde-elliptical particle motion. On crossplots of x and y velocity components, this will show up as a 90-degree phase difference between the two. In order to separate the three different wave types even more, a wavelet frequency 120 Hz is used. The response in the second quadrant contains only the diffracted solution since this is a shadow-zone. Thus, the reference field is a 200-by-100-node (199 m by 99 m) grid corresponding to the bottom half of the baseline model. The diffracted field is obtained by subtracting the reference from the full field.

Figures 2-37 to 2-40 are cross plots of x and y velocities of the diffracted solution. Note the different scale used for this series of plots. The low amplitude early arrivals are diffractions from the P-wave. The higher amplitude response is the diffracted Rayleigh wave with the 90-degree phase difference between the two components. The diffracted Rayleigh wave travels along both the inclined free surface (transmitted) and the positive x-axis (reflected), the former always having a higher amplitude than the latter. Figures 2-41 to 2-45 show vector plots of the diffracted field for different geometries.

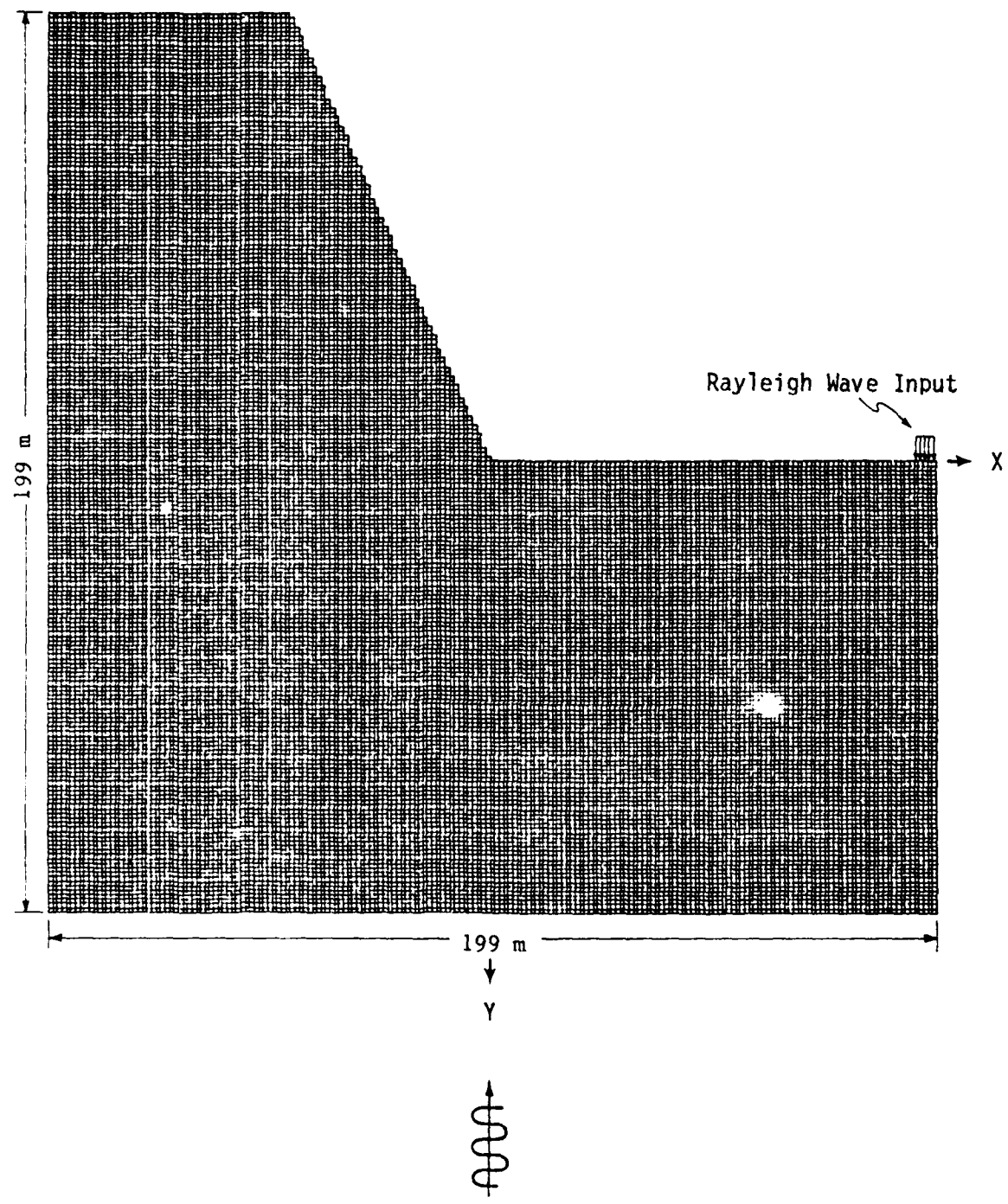


Figure 2-1. Baseline finite element model for 2-D slice of an idealized mesa or escarpment base.

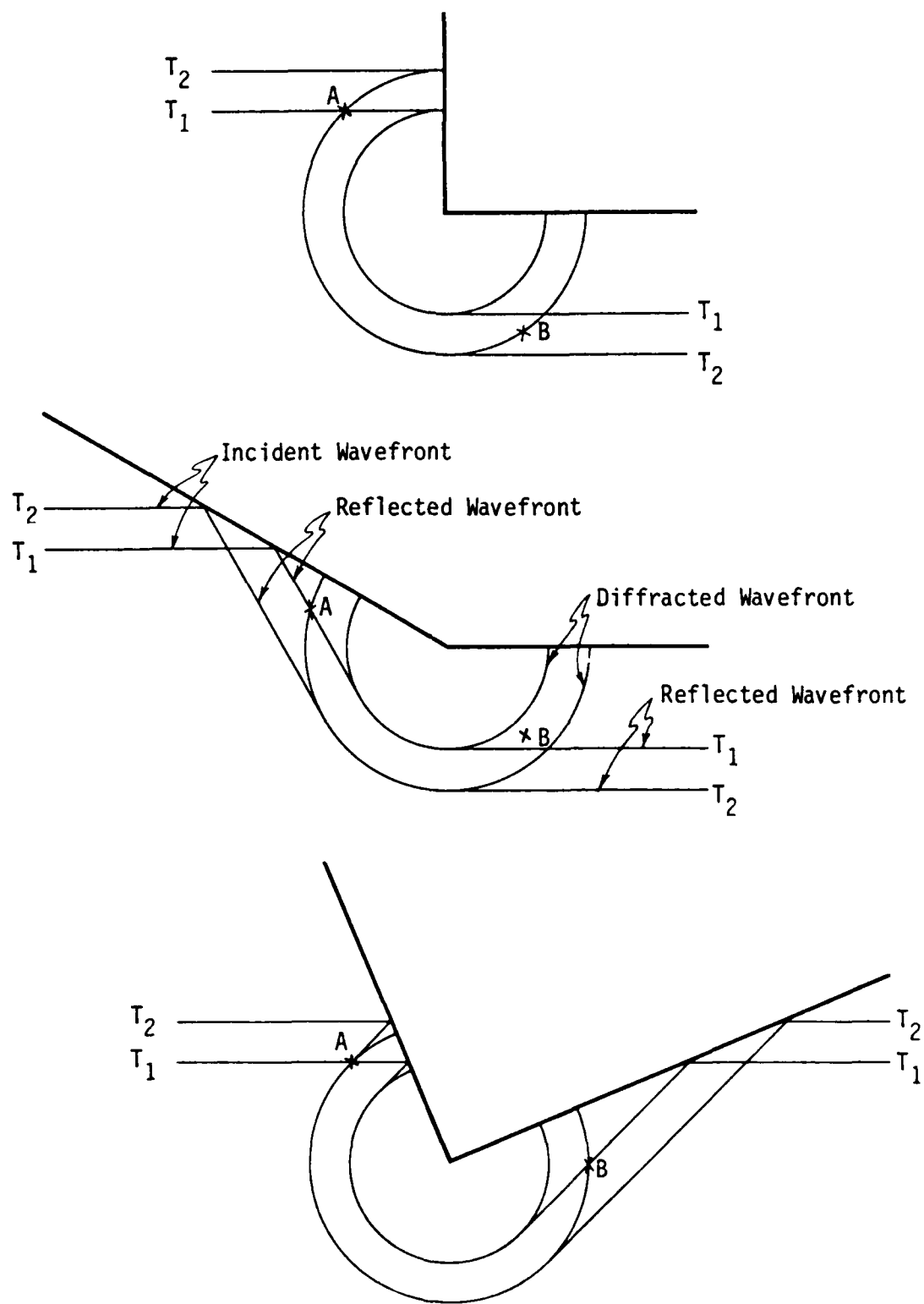


Figure 2-2. Diffracted wavefronts for an SH-wave incident from below at times T_1 and T_2 , where $T_2 > T_1$.

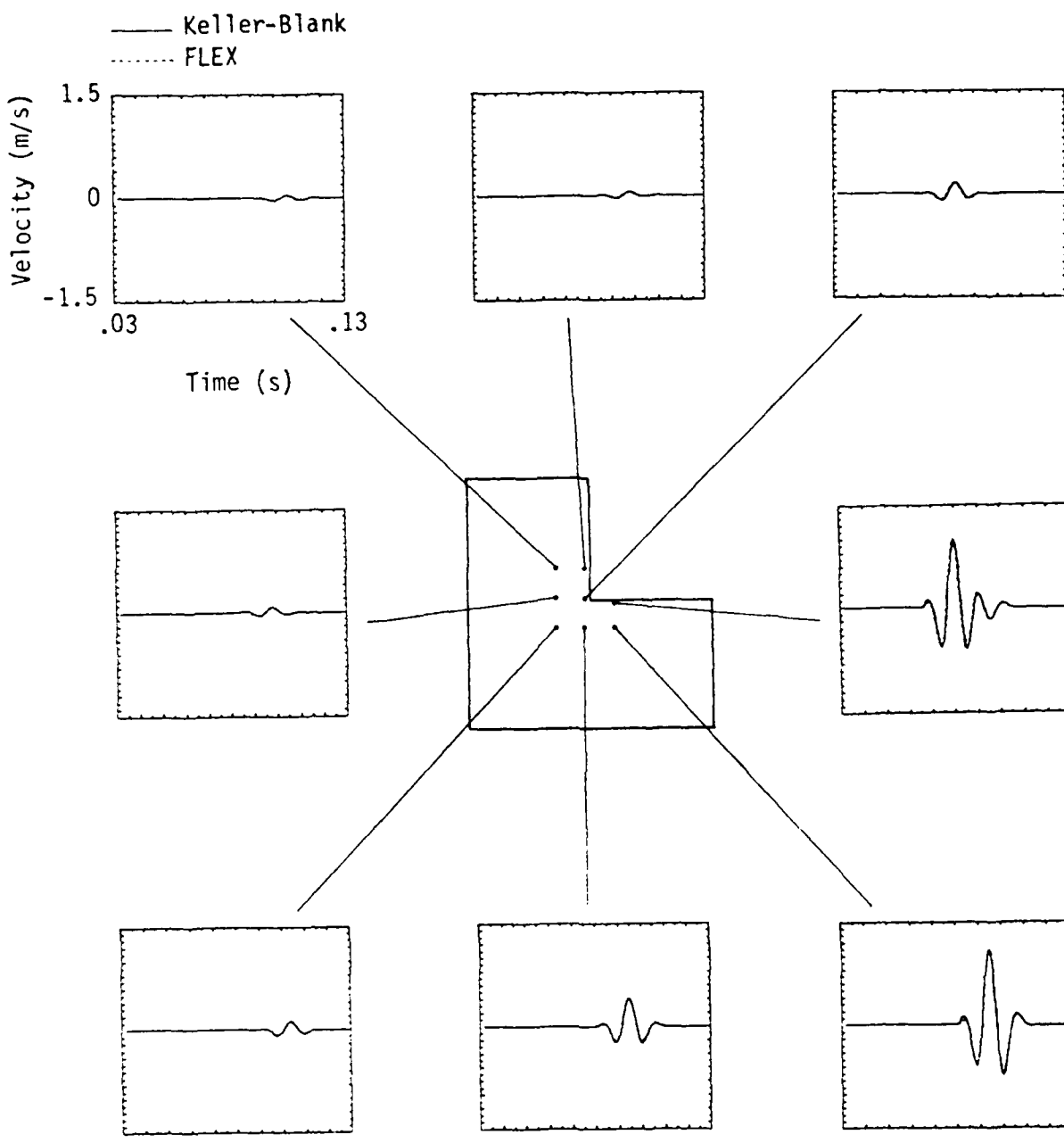


Figure 2-3. Comparison of Keller-Blank and FLEX solution for SH-wave incident from below to 90-degree mesa.

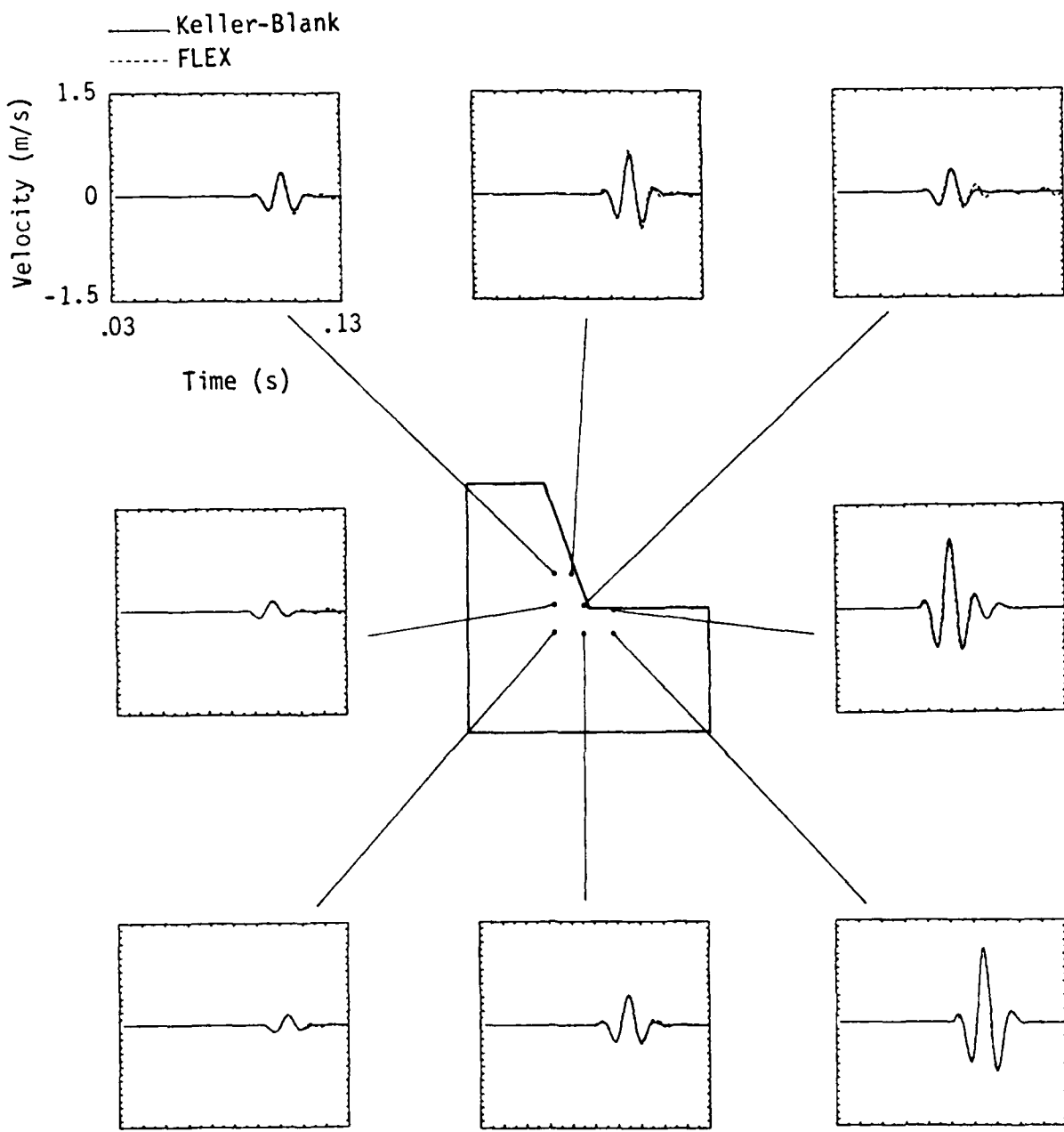


Figure 2-4. Comparison of Keller-Blank and FLEX solution for SH-wave incident to 70-degree mesa.

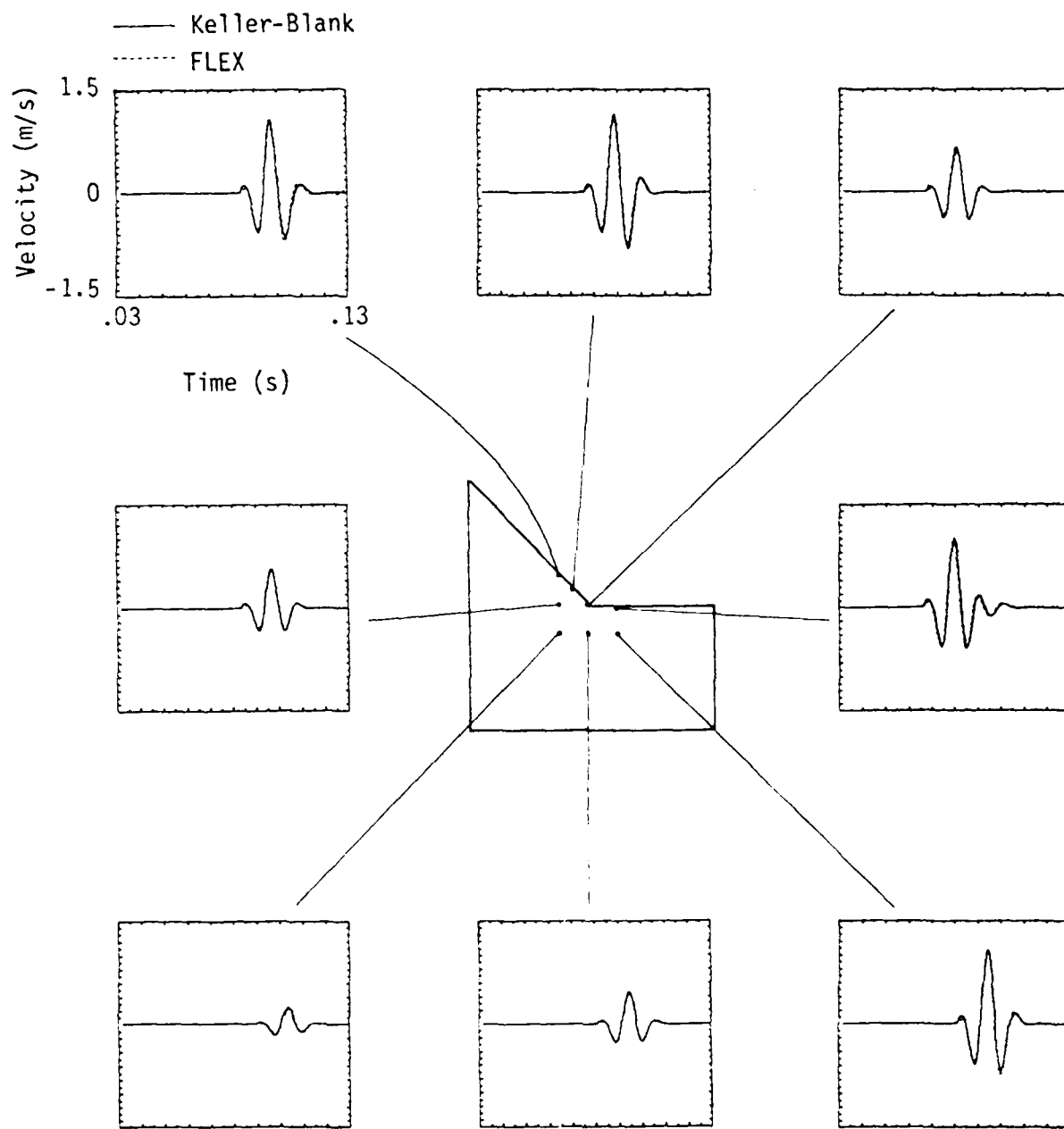


Figure 2-5. Comparison of Keller-Blank and FLEX solutions for SH-wave incident to 45-degree mesa.

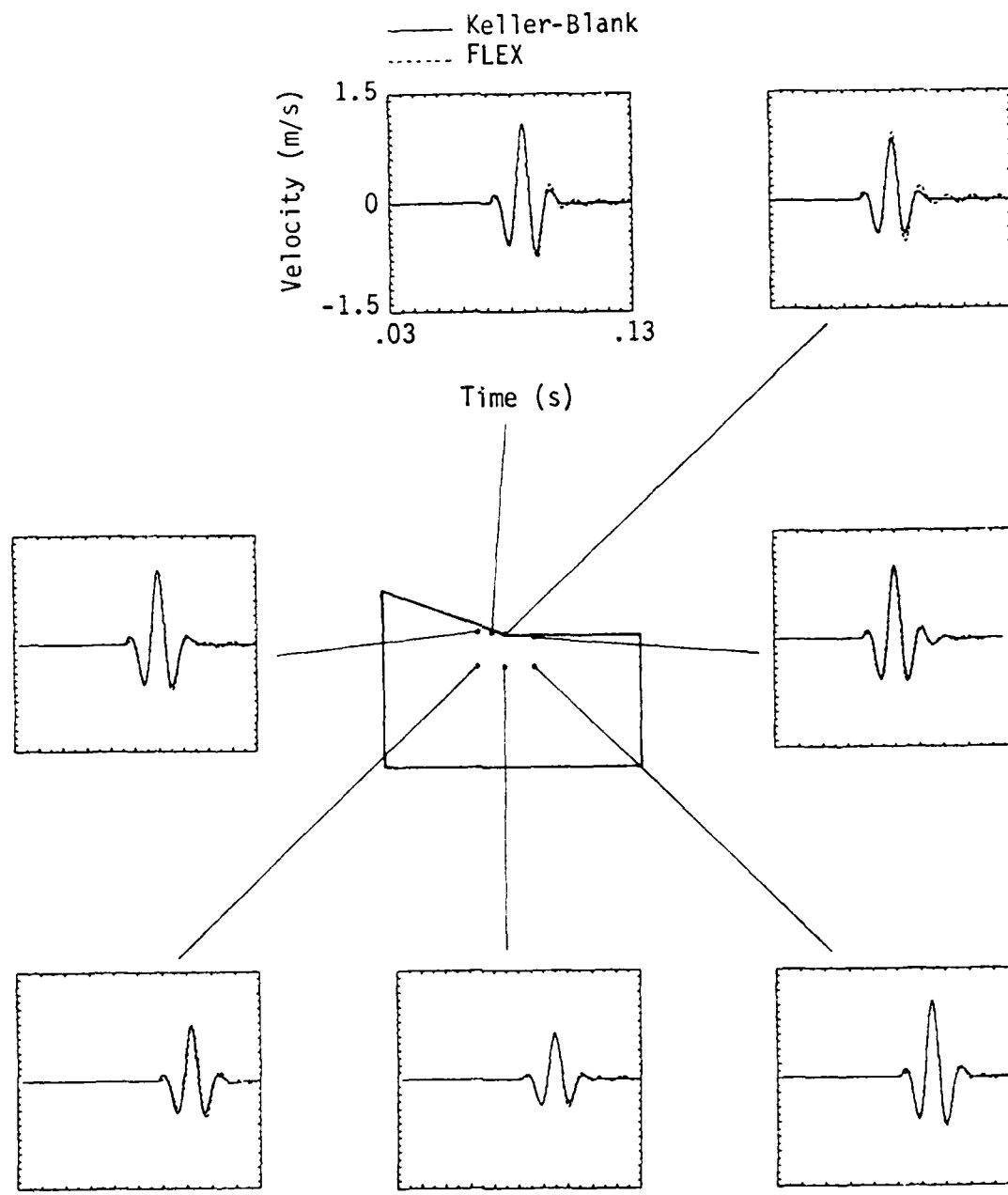


Figure 2-6. Comparison of Keller-Blank and FLEX solution for SH-wave incident to 20-degree mesa.

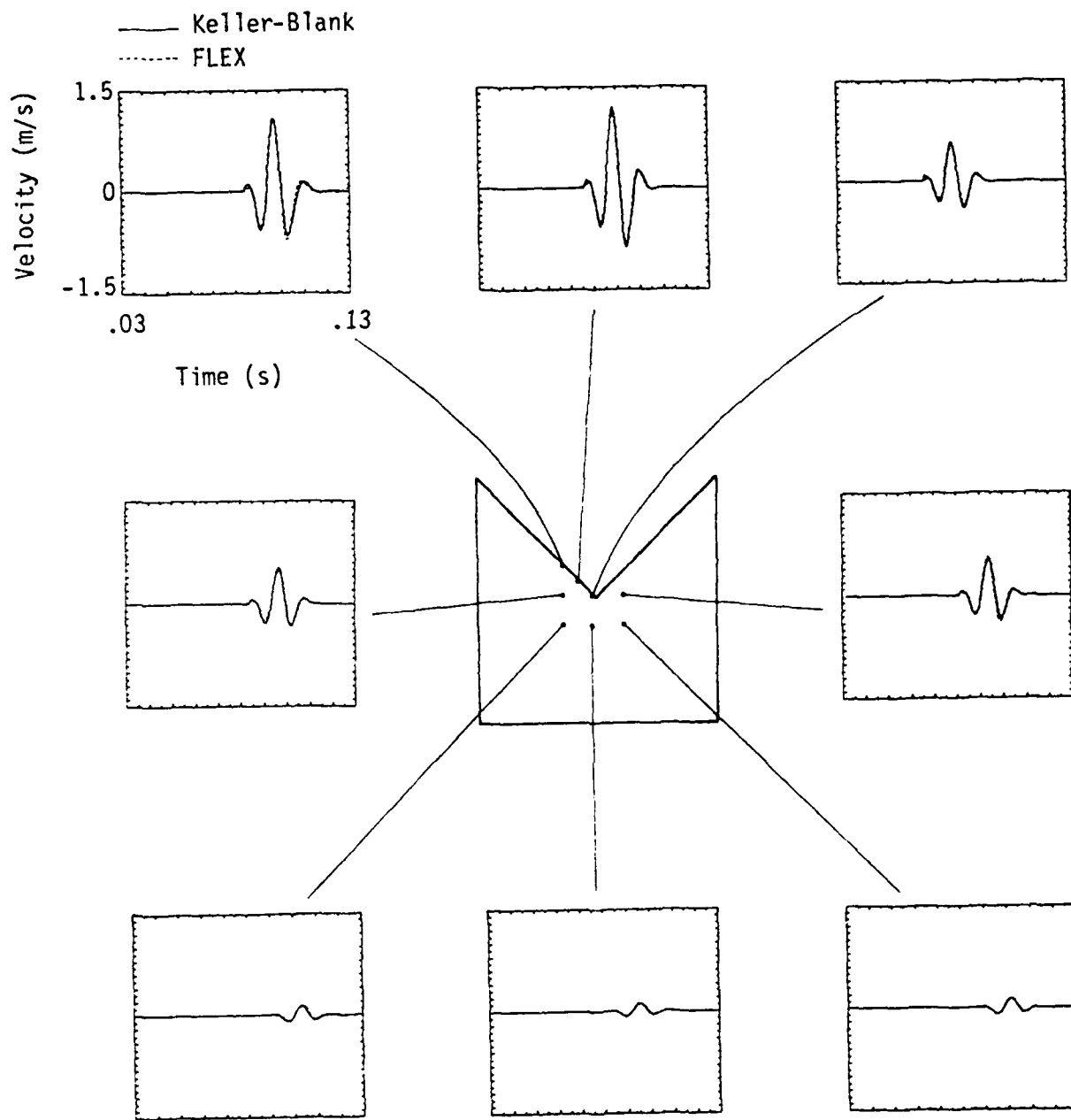


Figure 2-7. Comparison of Keller-Blank and FLEX solutions for SH-wave incident to 90-degree mesa, offset 45 degrees.

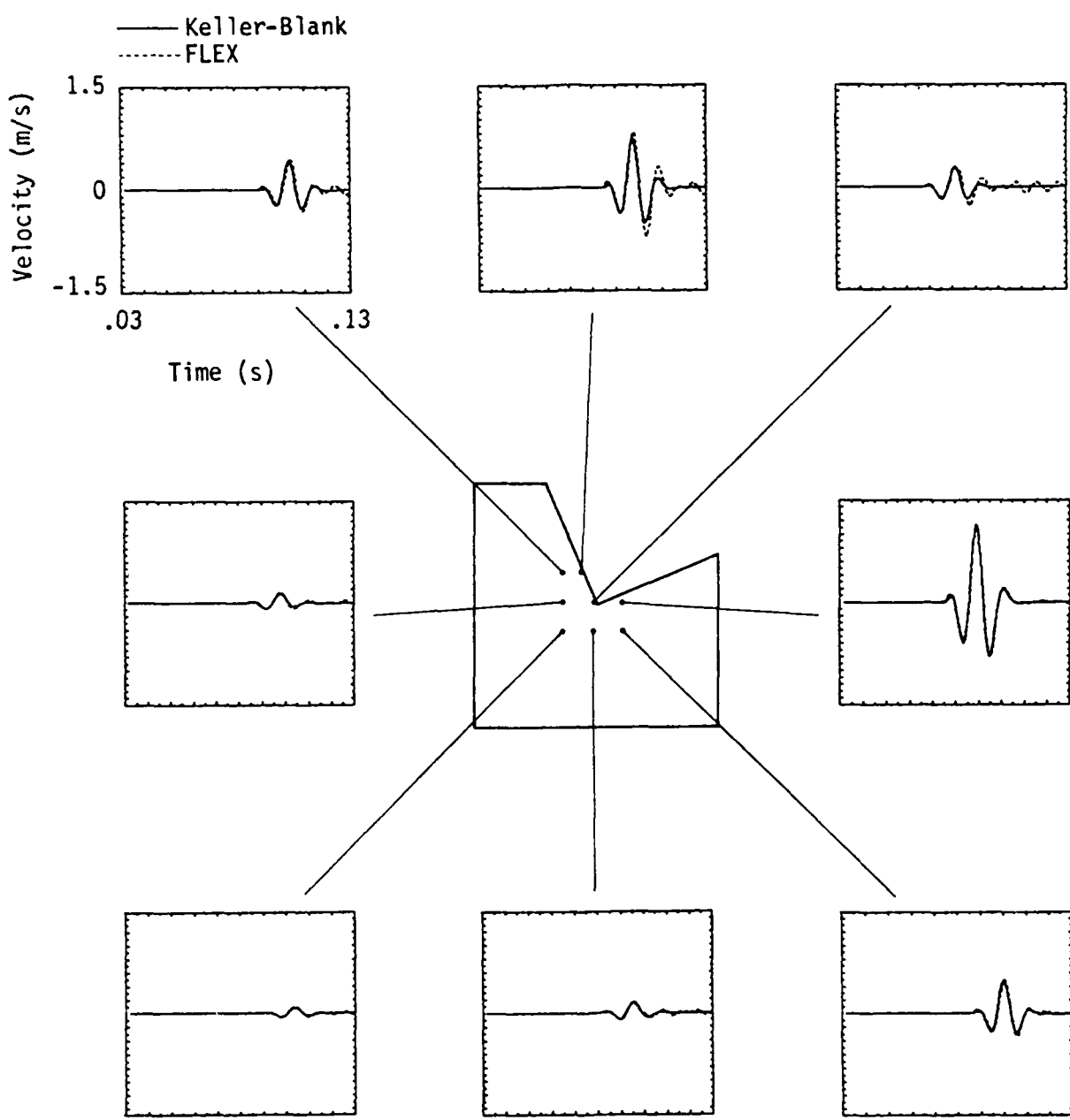


Figure 2-8. Comparison of Keller-Blank and FLEX solutions for SH-wave incident to 90-degree mesa, offset 22.5 degrees.

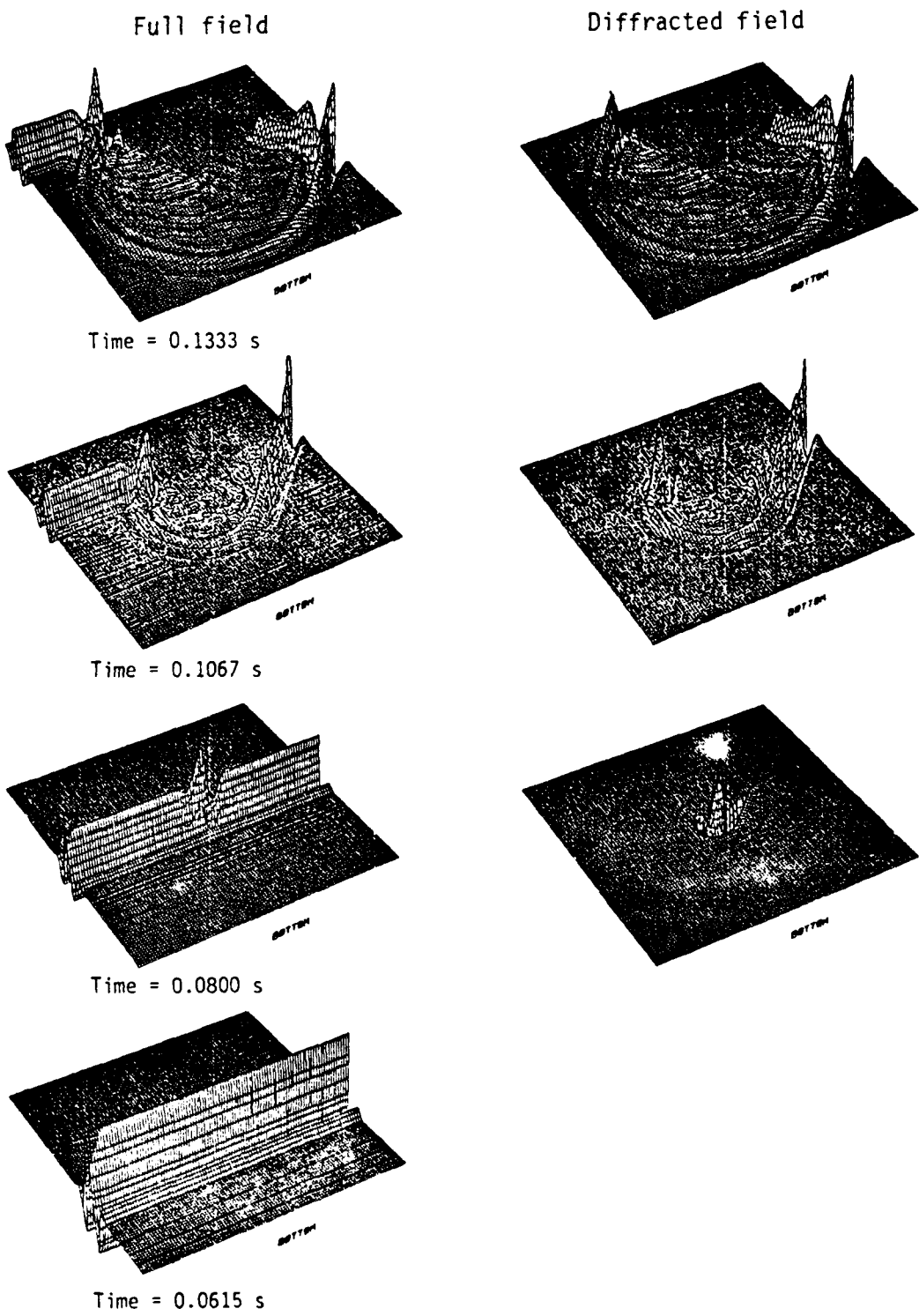


Figure 2-9. Surface plots of diffraction for SH-wave incidence on 90-degree mesa, offset 22.5 degrees.

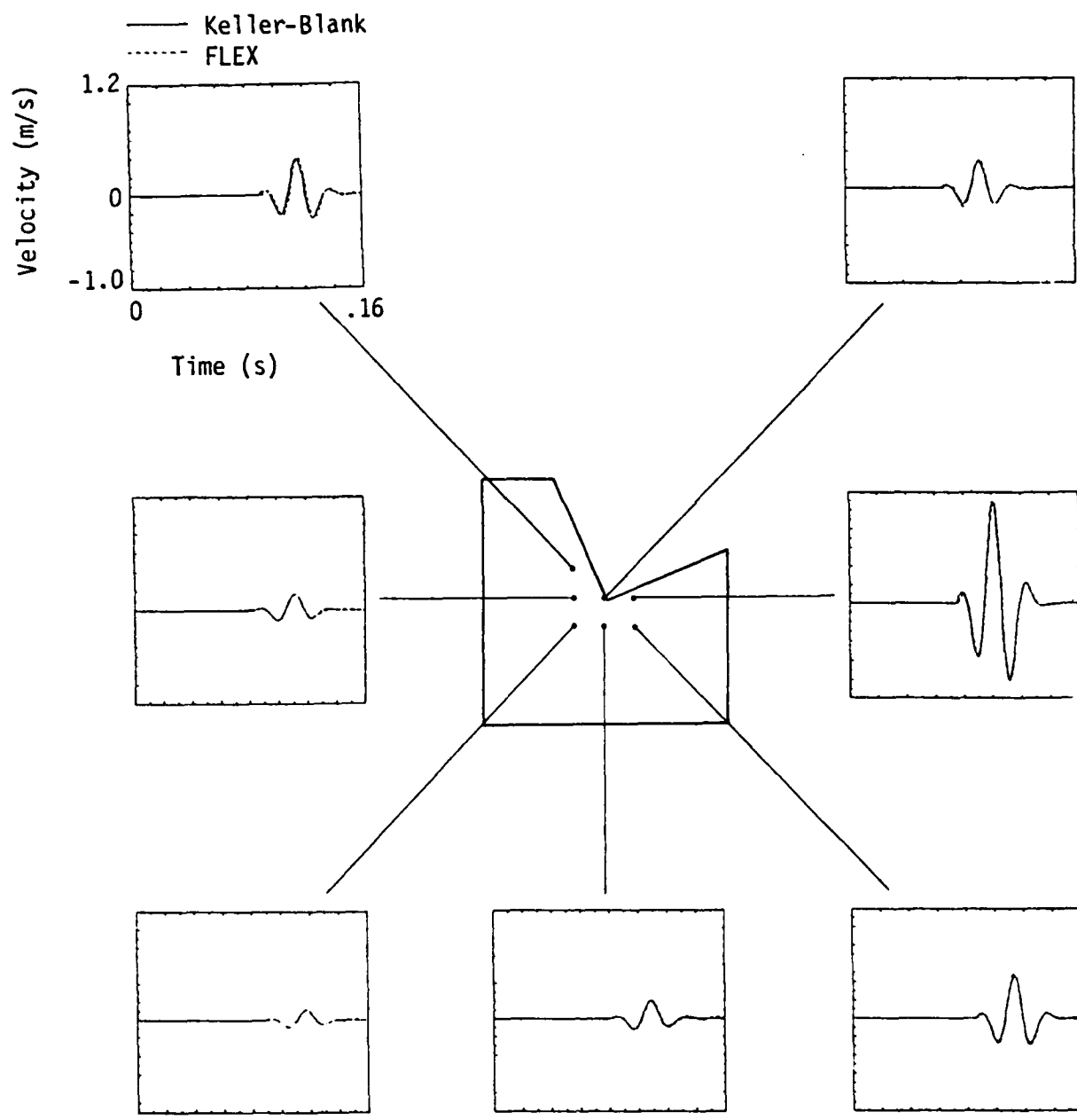


Figure 2-10. Comparison of Keller-Blank and FLEX solutions for geometry shown in Fig. 2-8, 40 Hz SH wavelet input

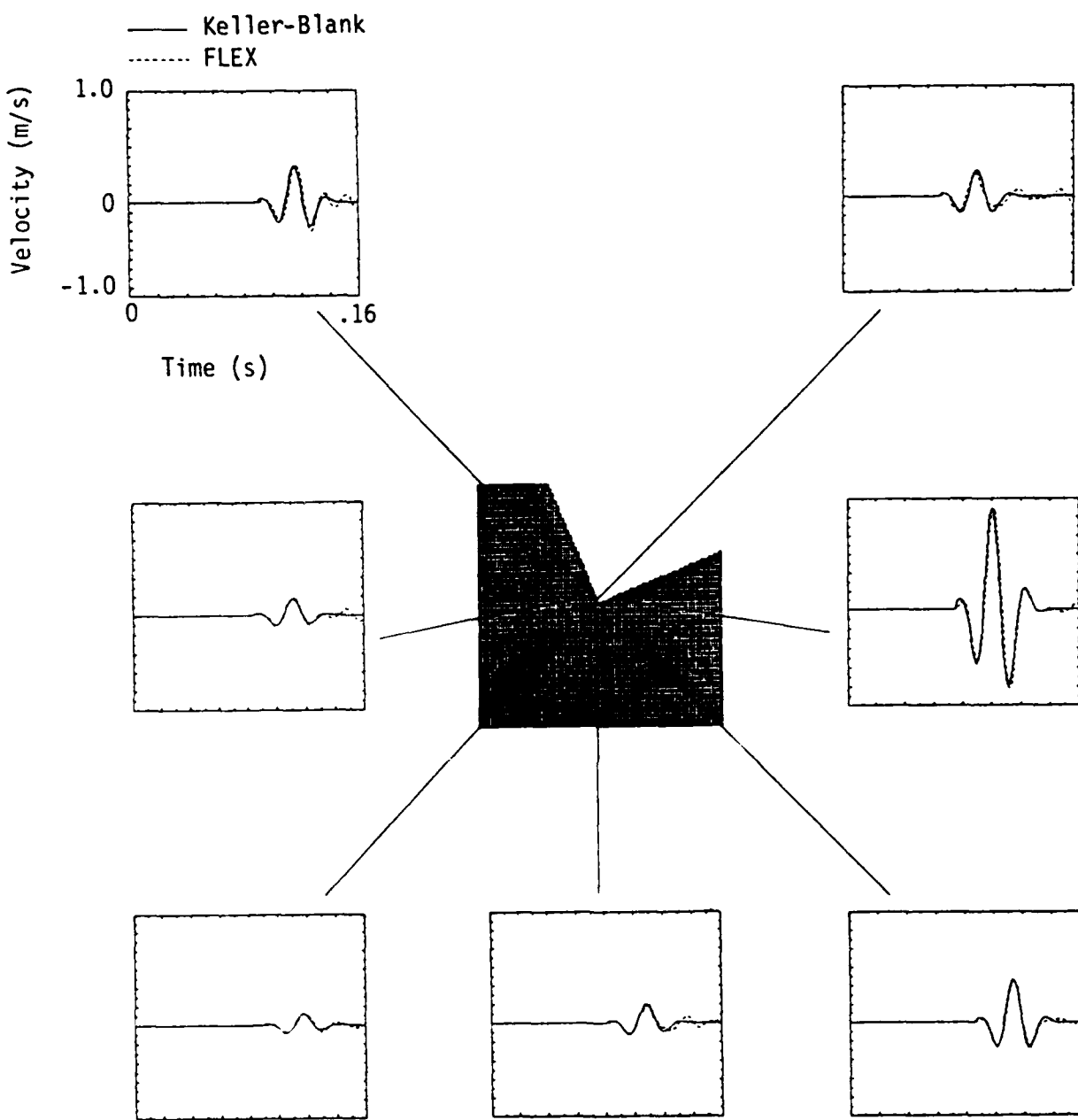


Figure 2-11. Comparison of Keller-Blank and FLEX solutions for geometry shown in Fig. 2-8, 40 Hz SH wavelet input, coarse grid.

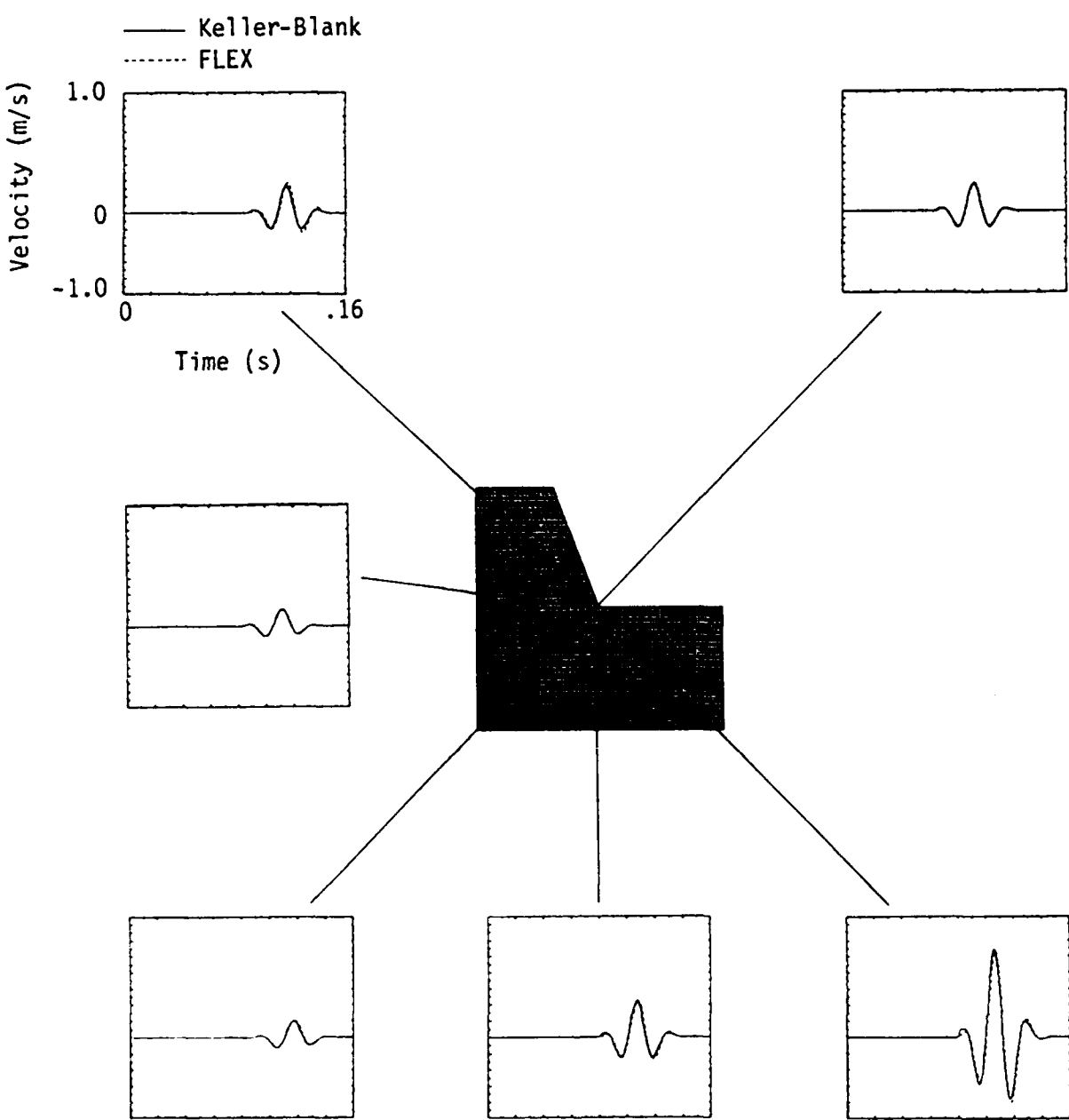


Figure 2-12. Comparison of Keller-Blank and FLEX solutions for the geometry in Fig. 2-4, 40 Hz SH wavelet input, coarse grid, skewed elements.

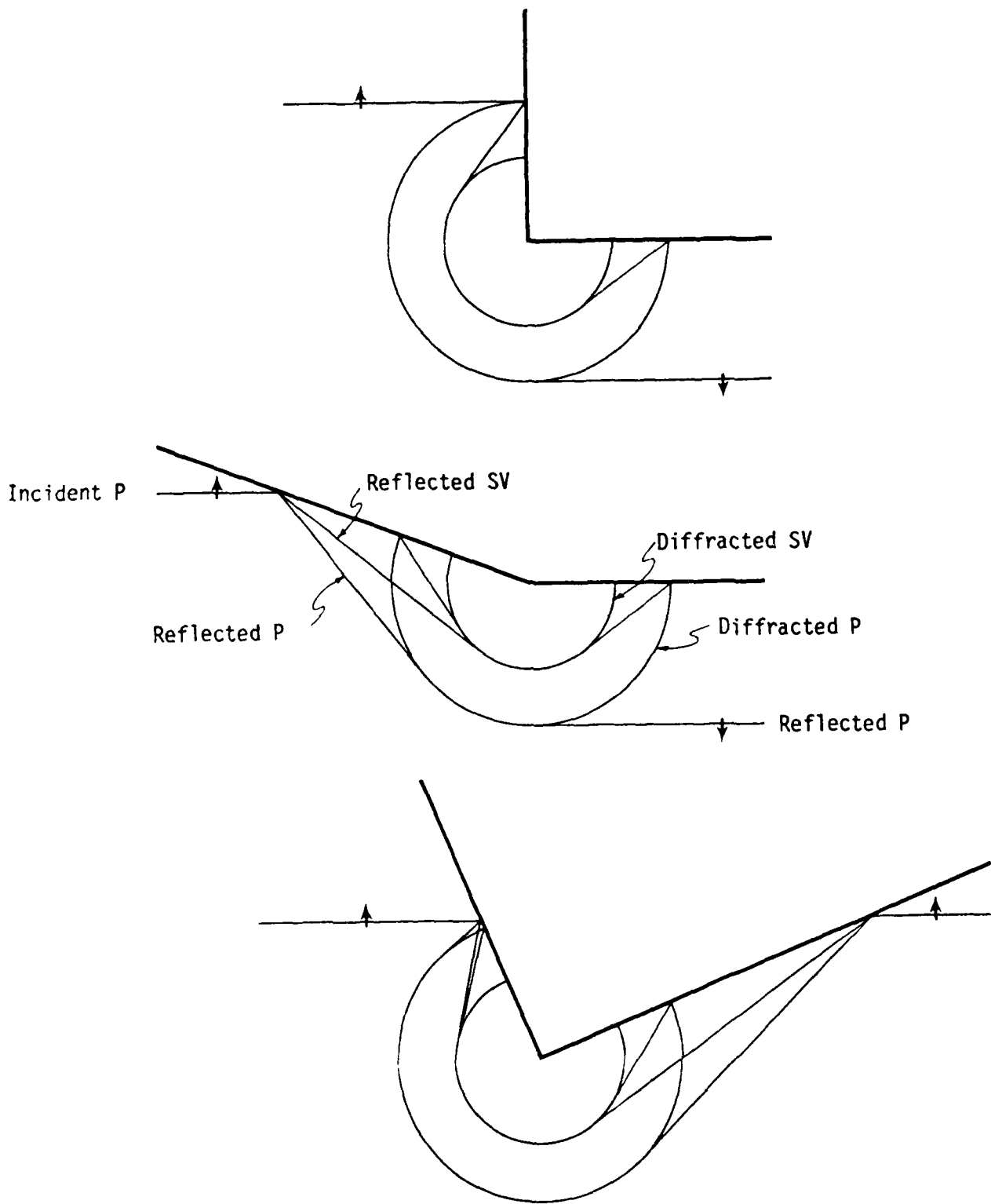


Figure 2-13. Diffractions for P-wave incidence from below for different geometries.

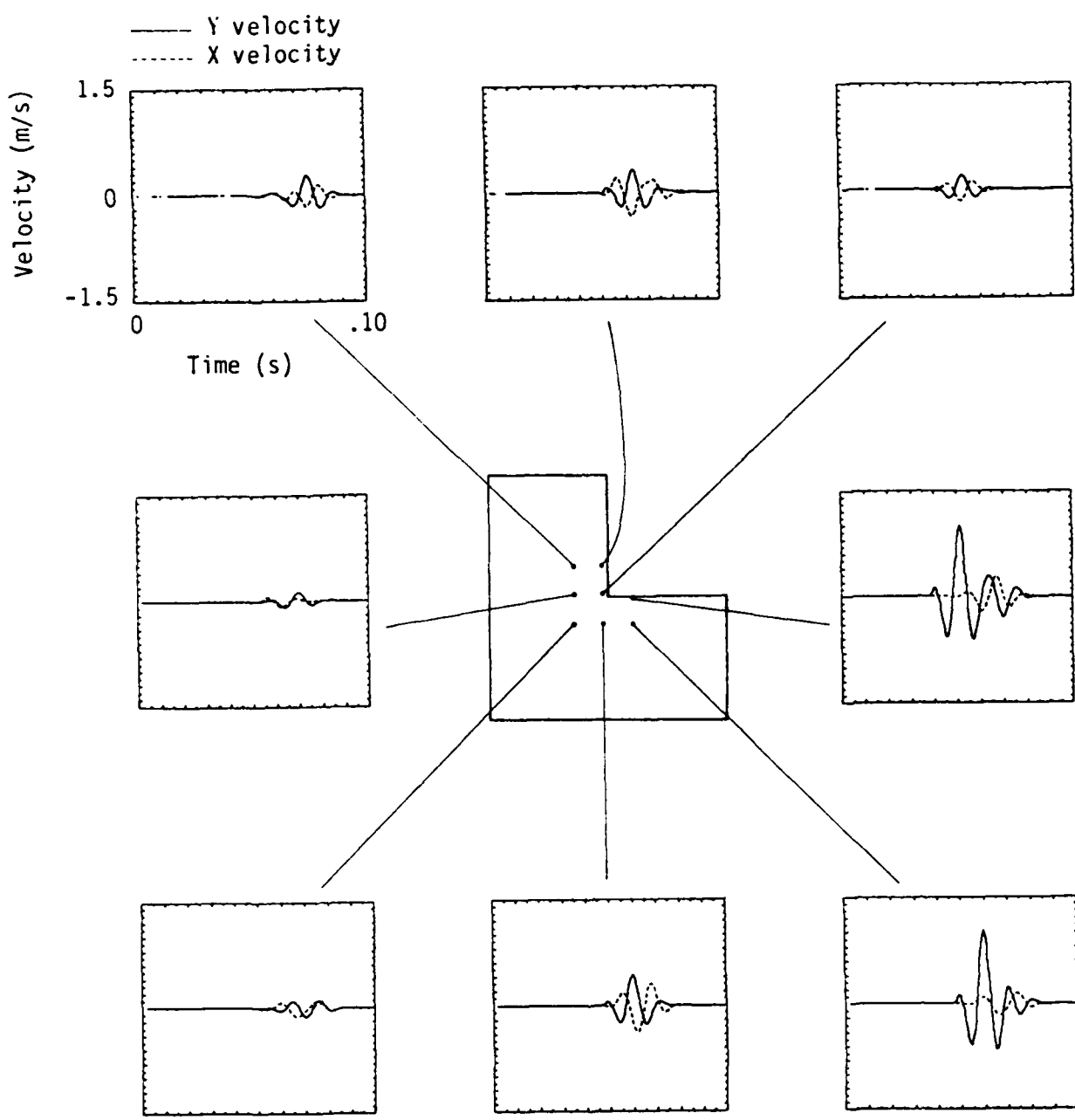


Figure 2-14. Time histories of diffracted field for P-wave incidence from below to 90-degree mesa.

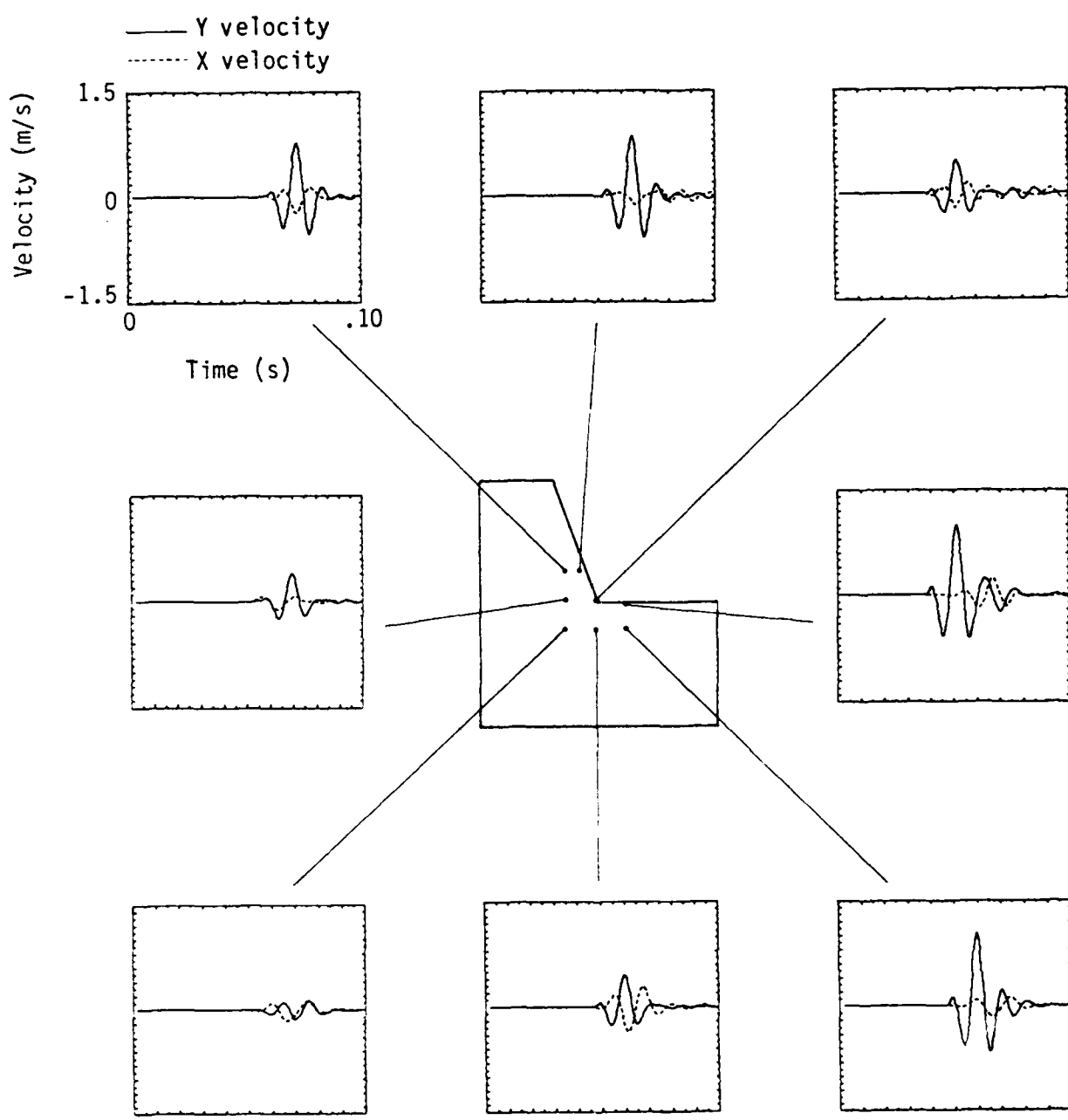


Figure 2-15. Time histories of diffracted field from P-wave incidence to 70-degree mesa.

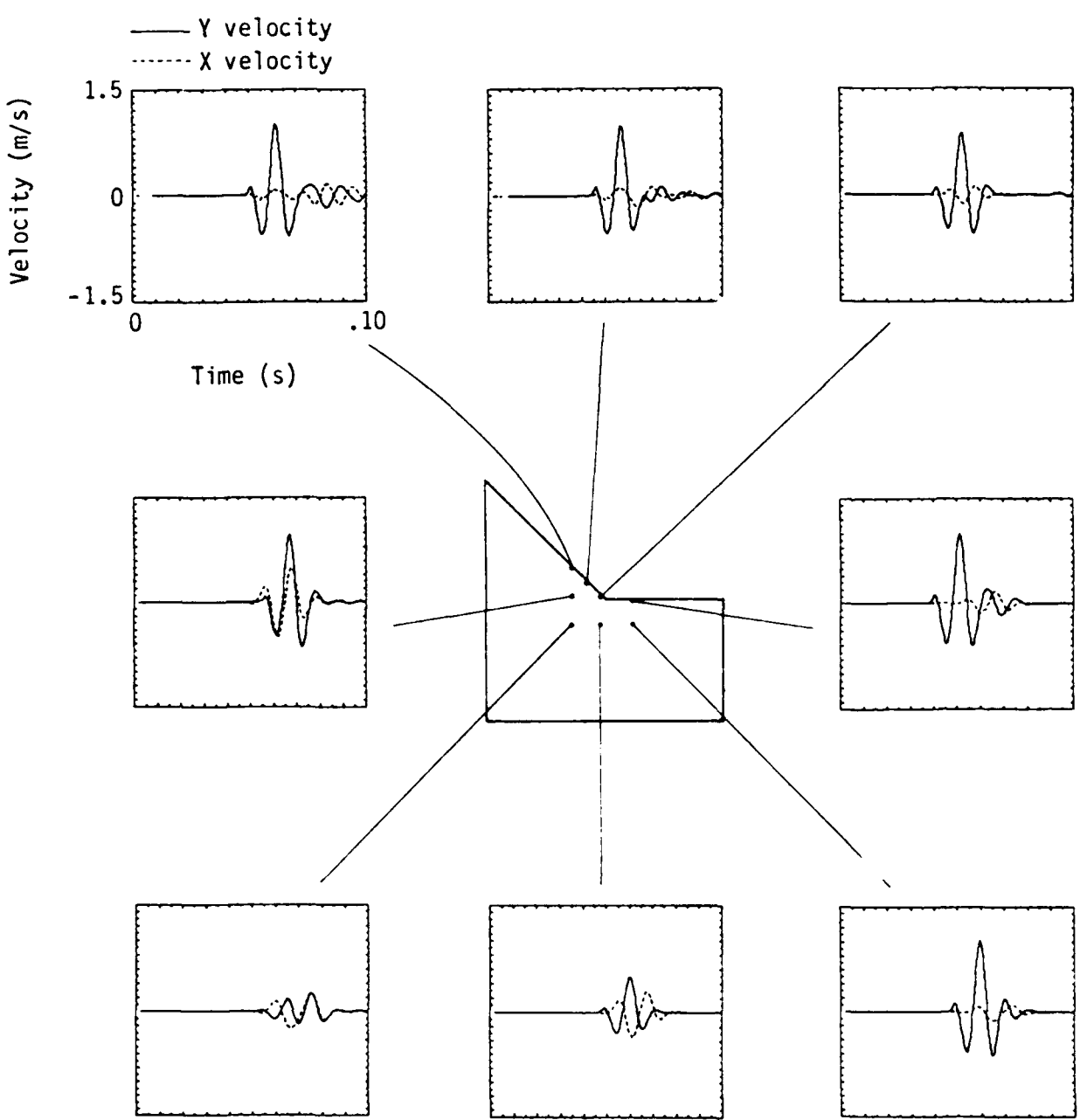


Figure 2-16. Time histories of diffracted field from P-wave incidence to 45-degree mesa.

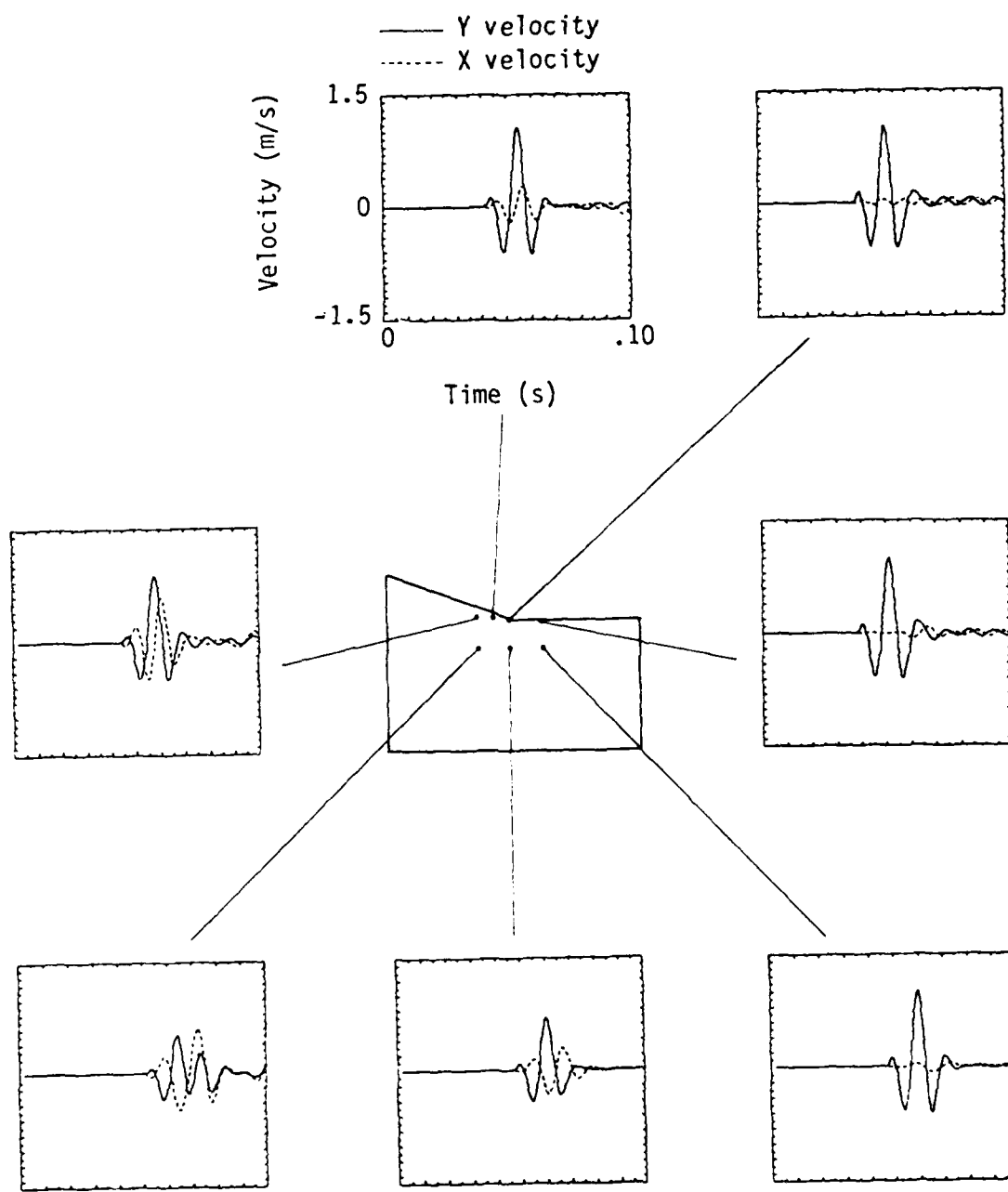


Figure 2-17. Time histories of diffracted field from P-wave incidence to 20-degree mesa.

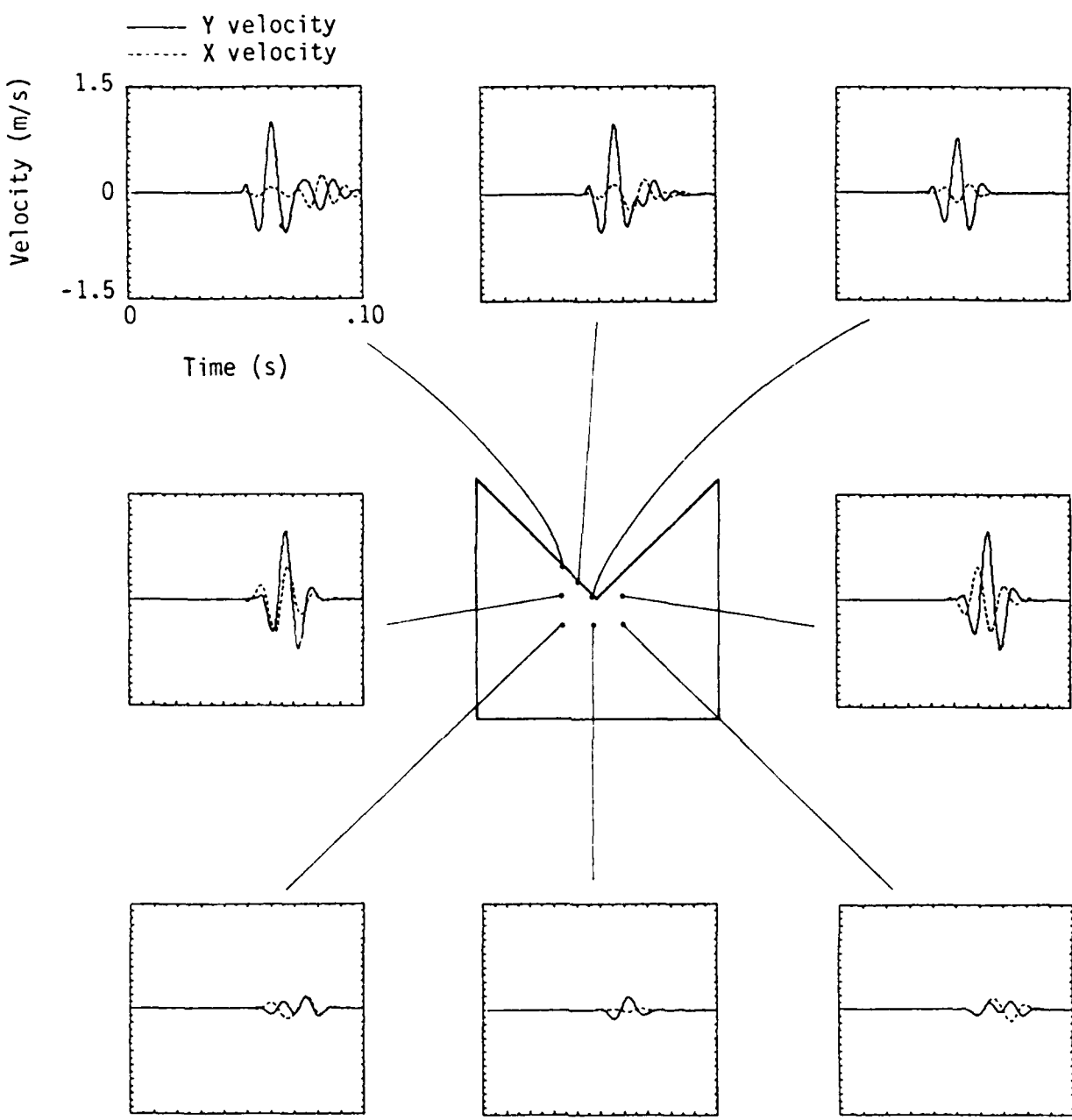


Figure 2-18. Time histories of diffracted field from P-wave incidence to 90-degree mesa, offset 45 degrees.

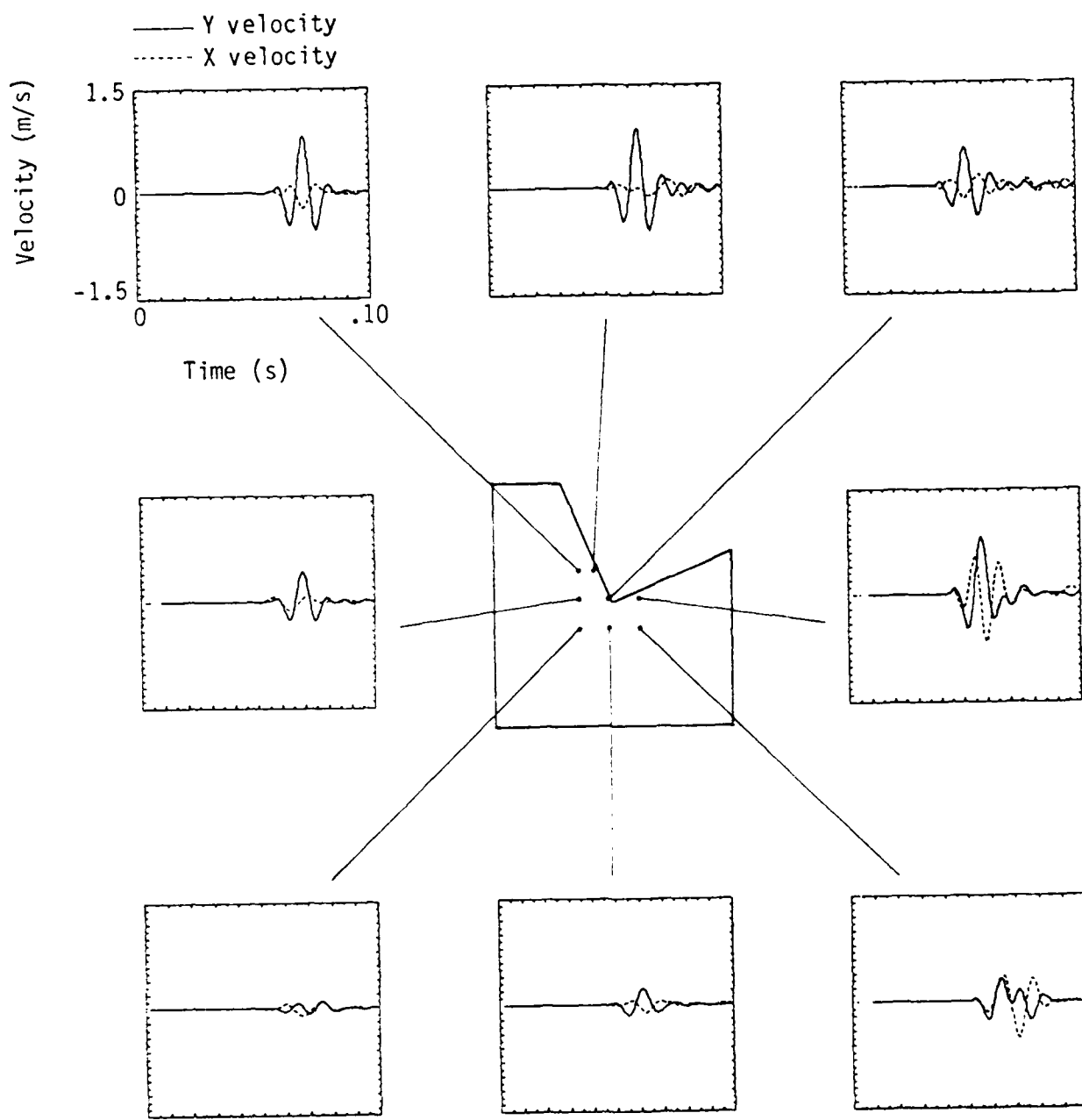
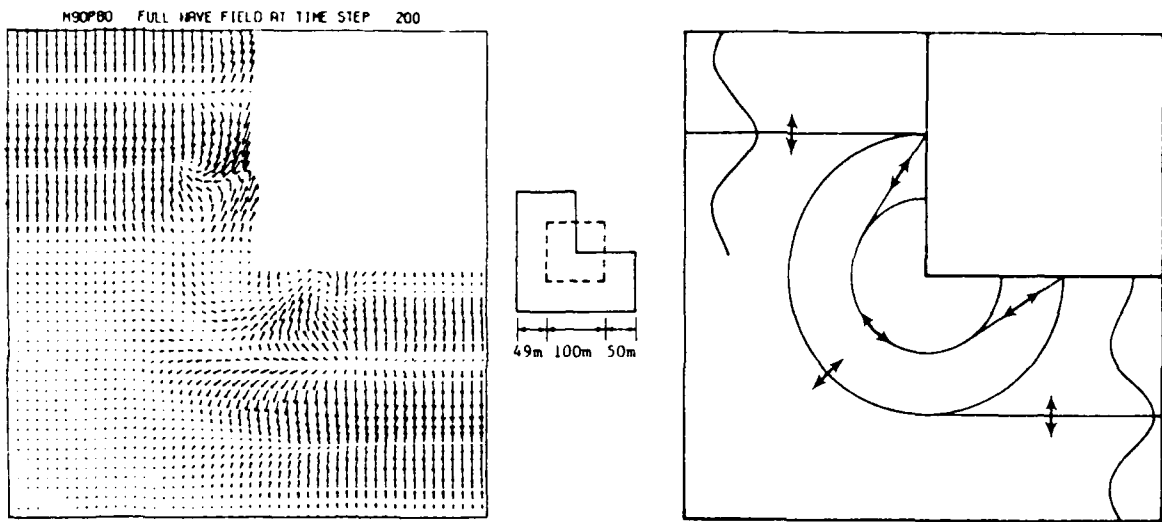
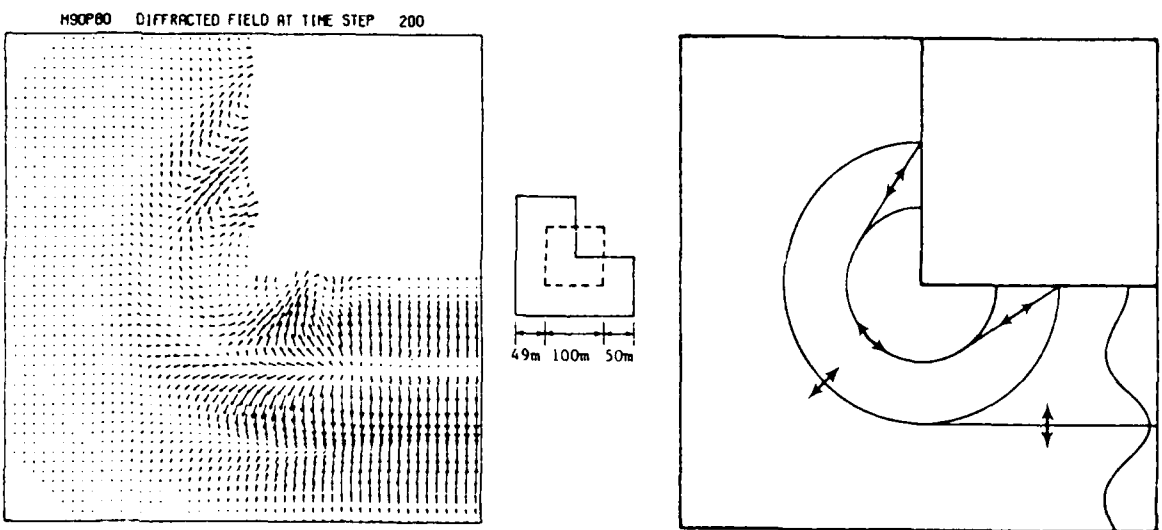


Figure 2-19. Time histories of diffracted field from P-wave incidence to 90-degree mesa, offset 22.5 degrees.

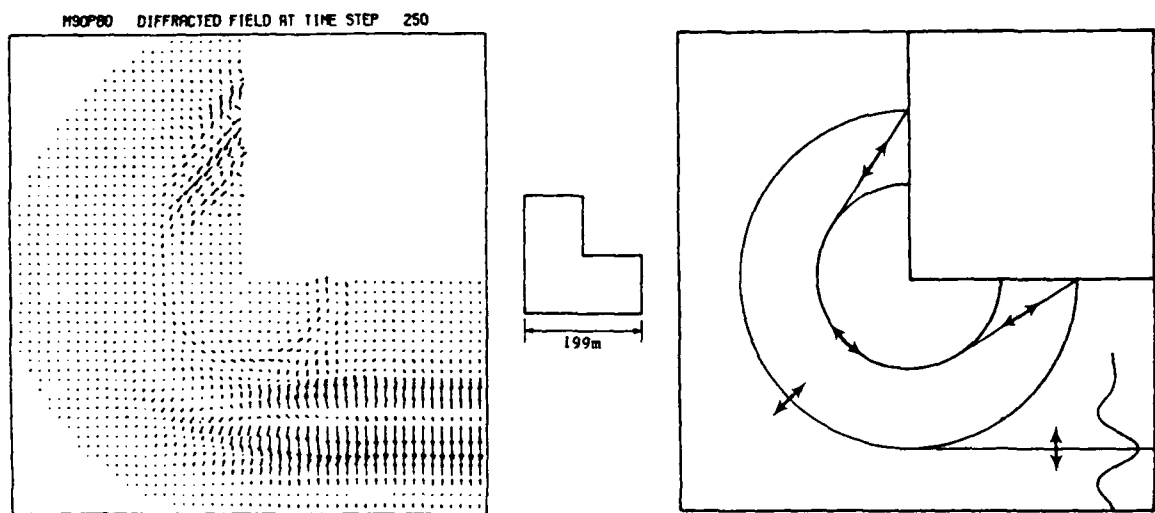


(a) Full-field for center grid at time 0.06158 s

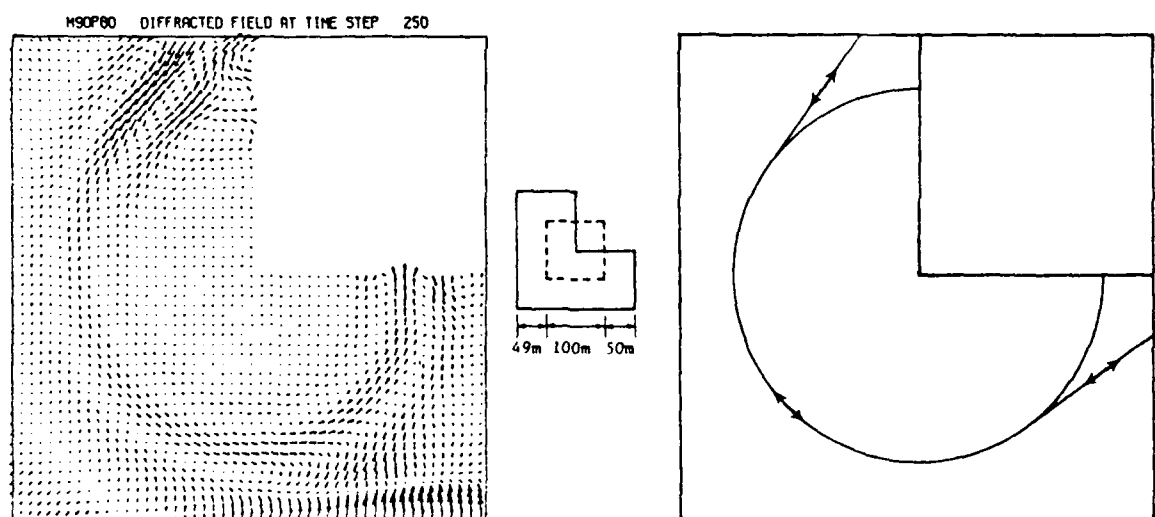


(b) Diffracted field for center grid at time 0.06158 s

Figure 2-20. Vector plots of diffraction from P-wave incidence at time 0.06158 s for 90-degree mesa.

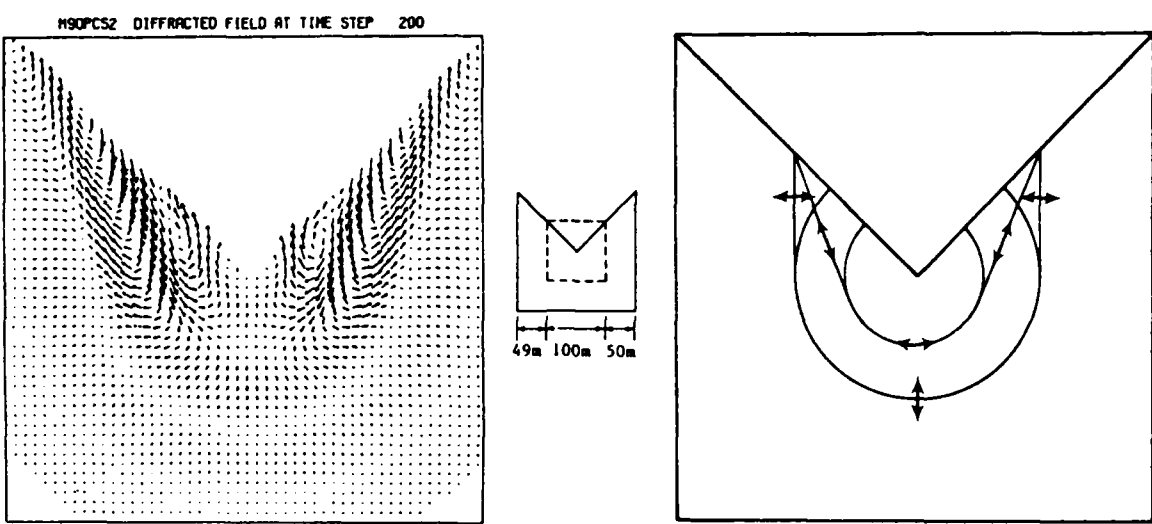


(a) Diffracted field for entire grid at time 0.07698 s

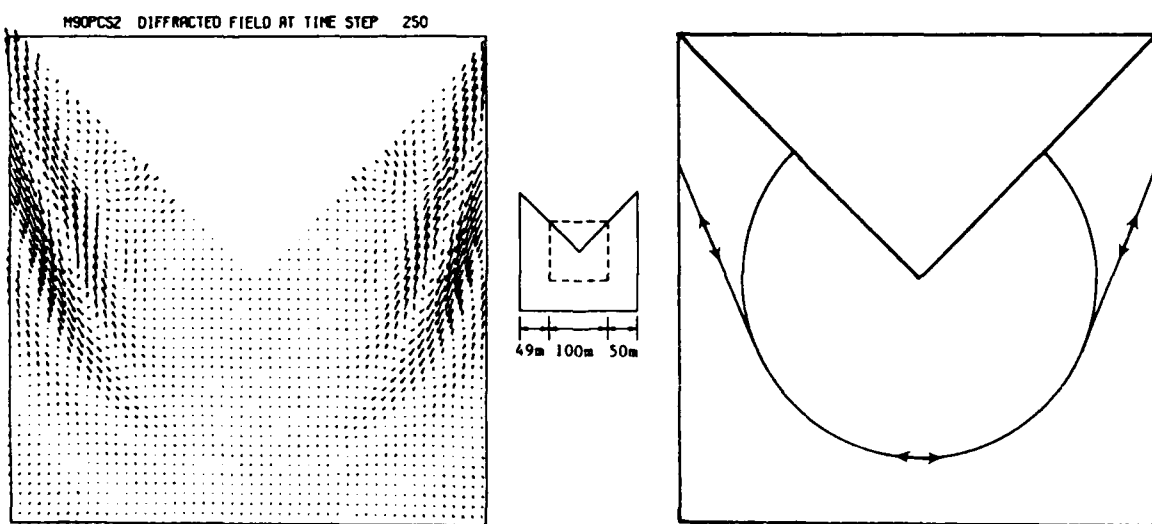


(b) Diffracted field for center grid at time 0.07698 s

Figure 2-21. Diffractions from P-wave incidence at time 0.07698 s for 90-degree mesa.



(a) Diffracted field for center grid at time 0.06158 s



(b) Diffracted field for center grid at time 0.07698 s

Figure 2-22. Diffractions from P-wave incidence for 90-degree mesa, offset 45 degrees.

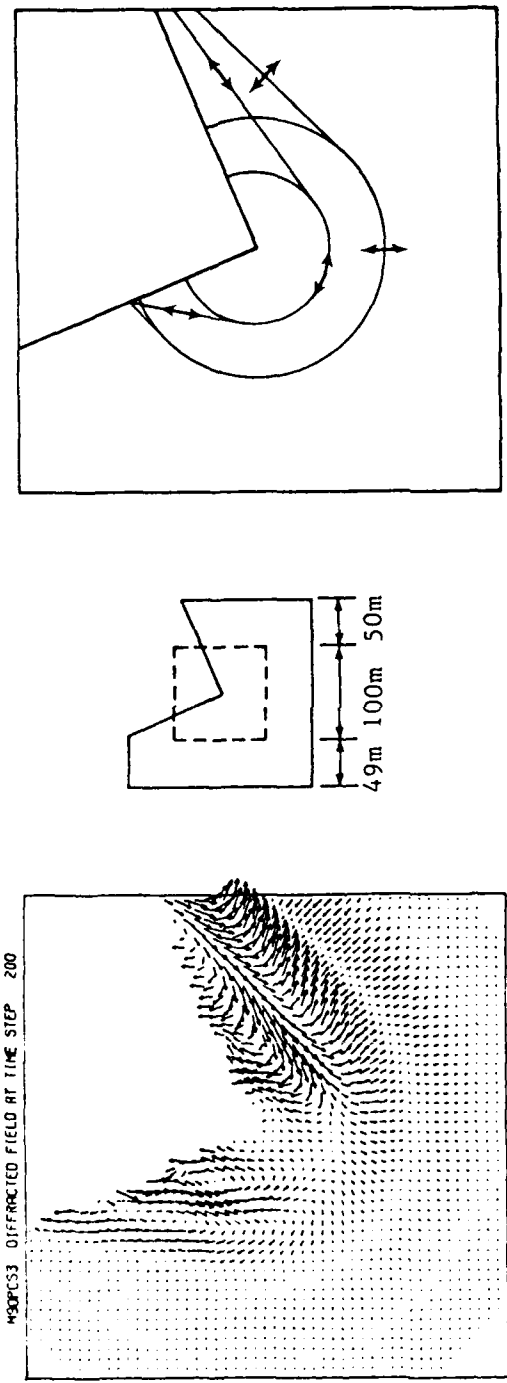
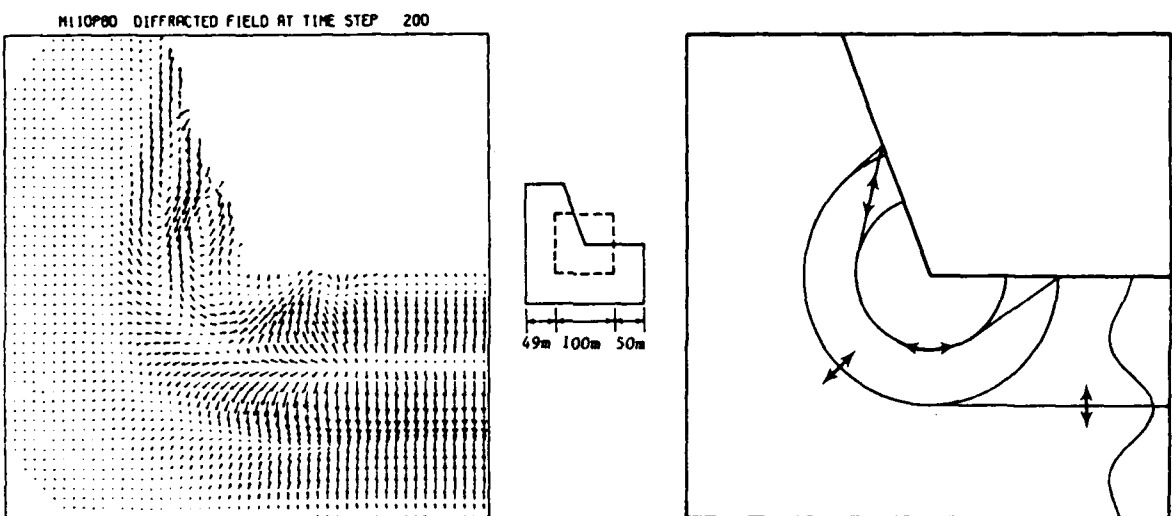
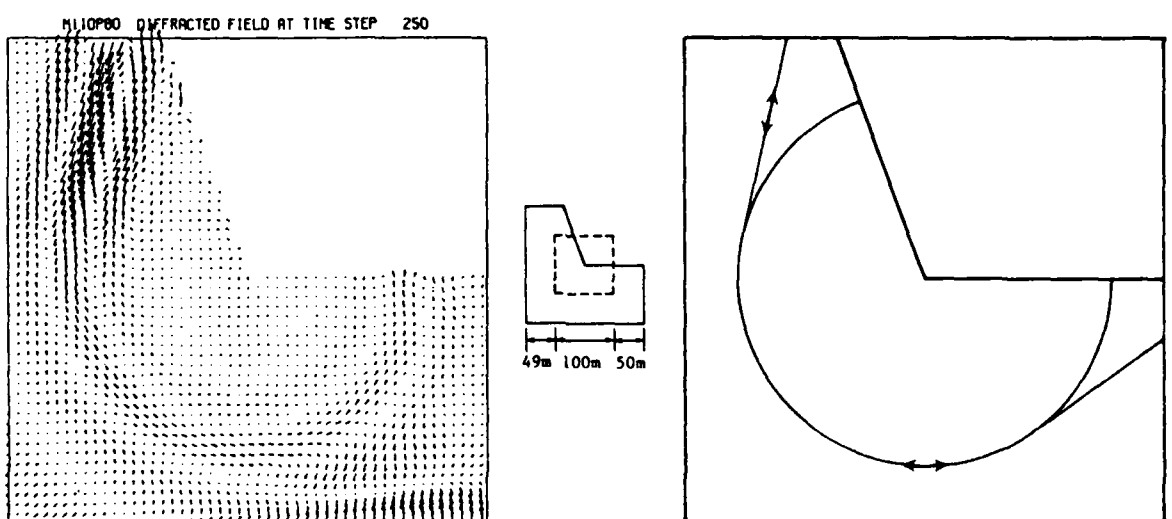


Figure 2-23 . Diffraction from P-wave incidence at time 0.06158 s for 90-degree mesa, offset 22.5 degrees, showing center portion of grid.



(a) Diffracted field for center grid at time 0.06158 s



(b) Diffracted field for center grid at time 0.07698 s

Figure 2-24. Diffractions from P-wave incidence on 70-degree mesa.

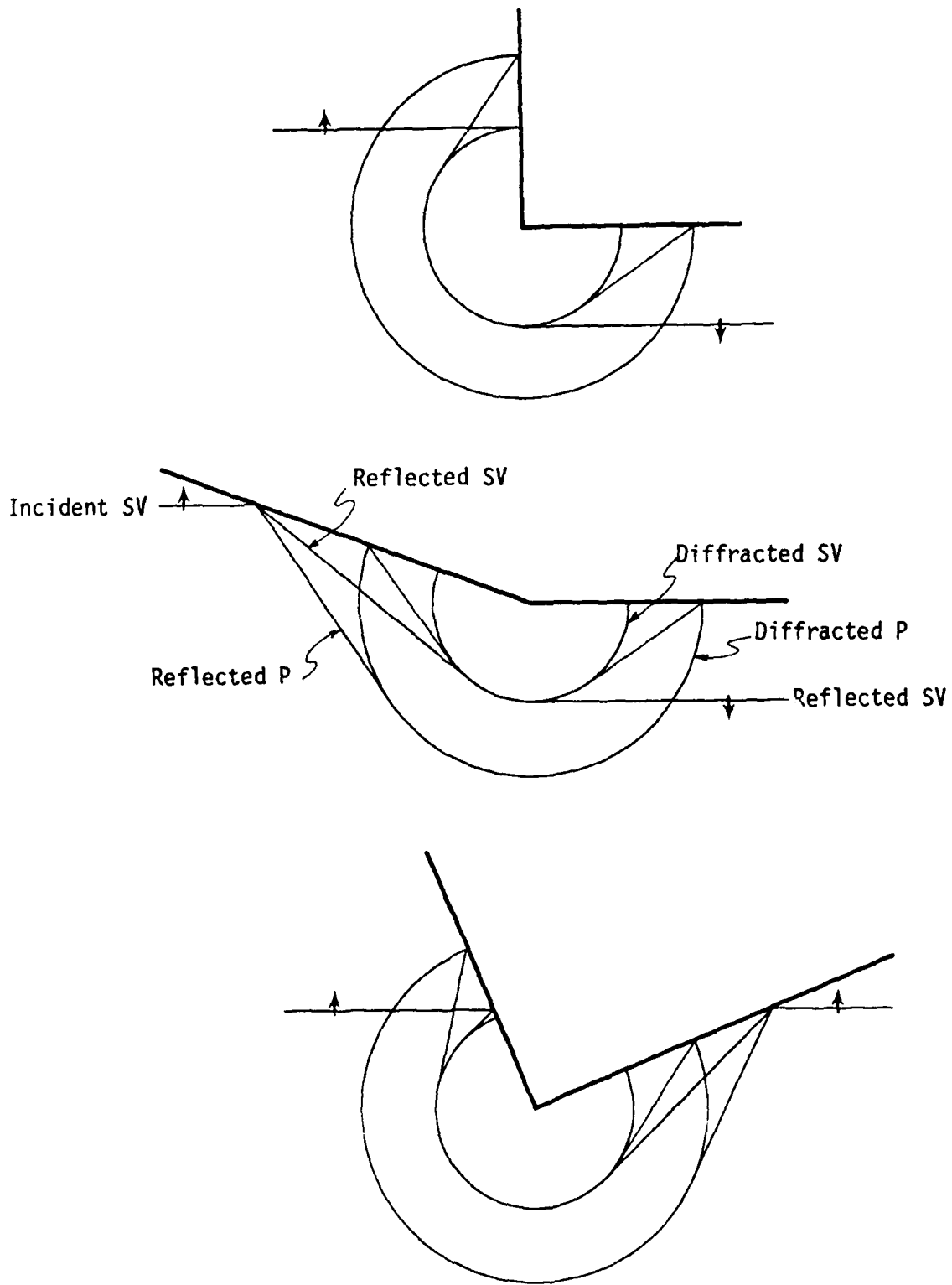


Figure 2-25. Diffractions for SV-wave incidence from below for different geometries.

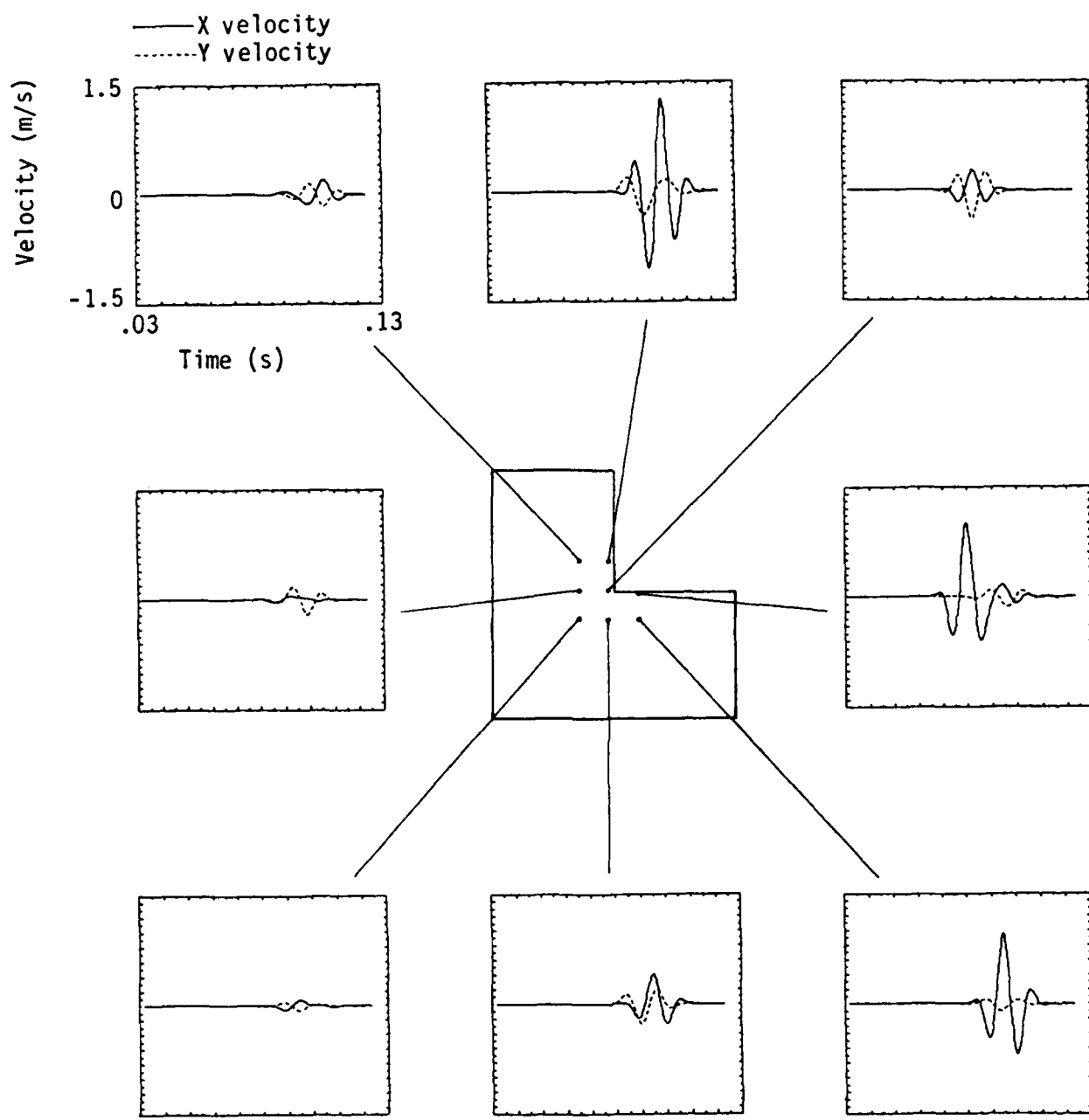


Figure 2-26. Time histories of diffracted field for SV-wave incidence from below to 90-degree mesa.

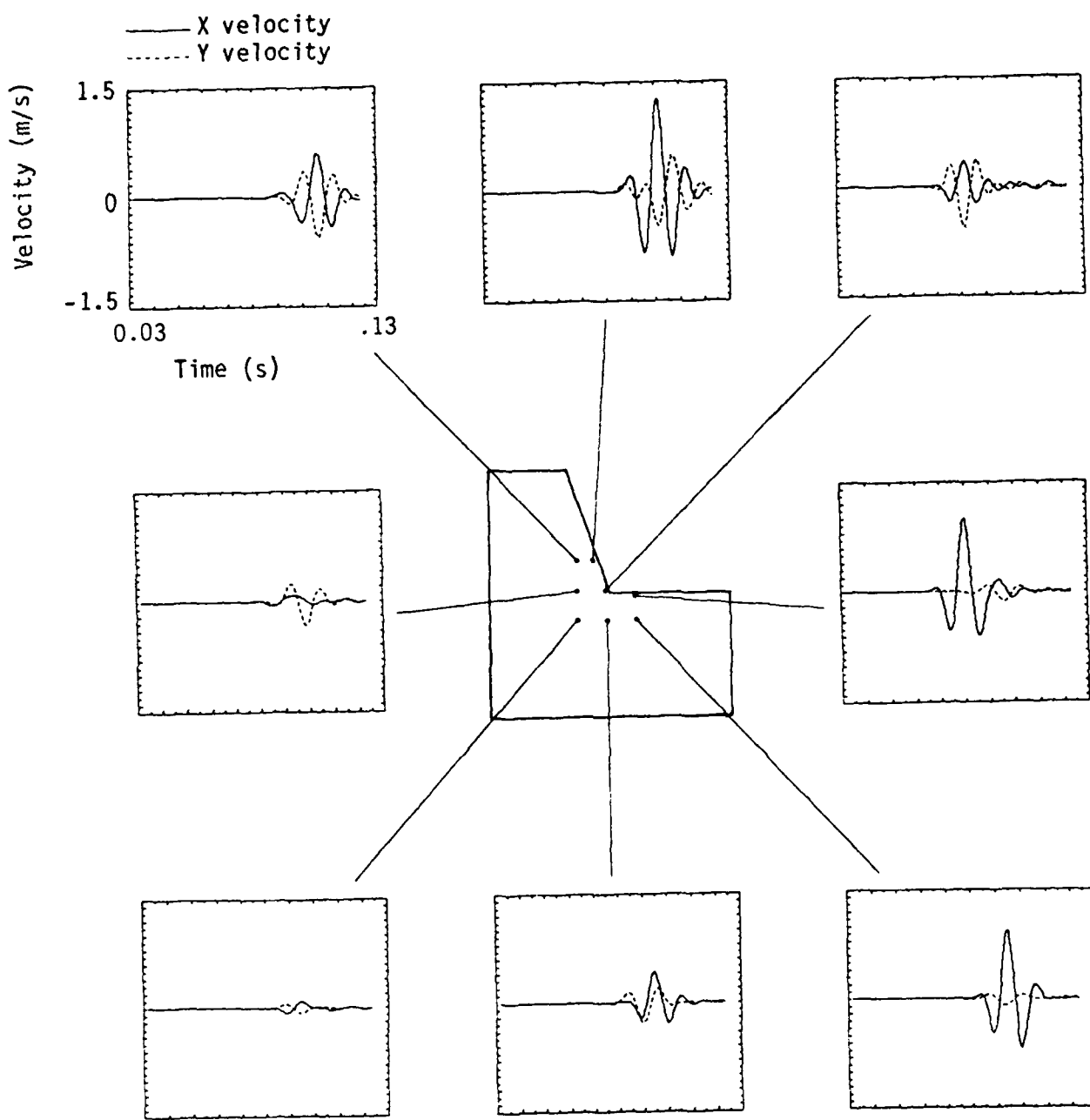


Figure 2-27. Time histories of diffracted field for SV-wave incidence to 70-degree mesa.

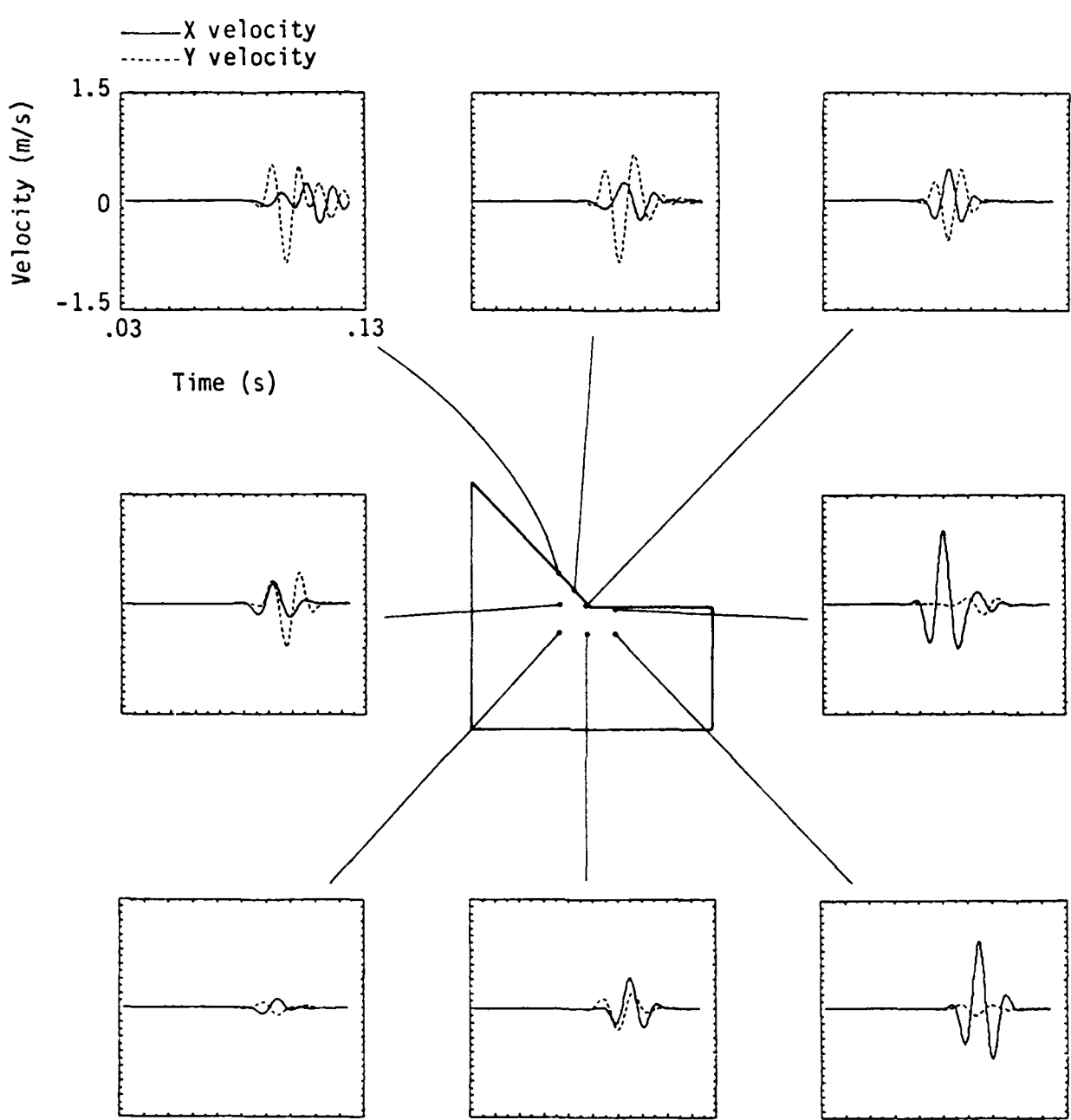


Figure 2-28. Time histories of diffracted field from SV-wave incidence to 45-degree mesa.

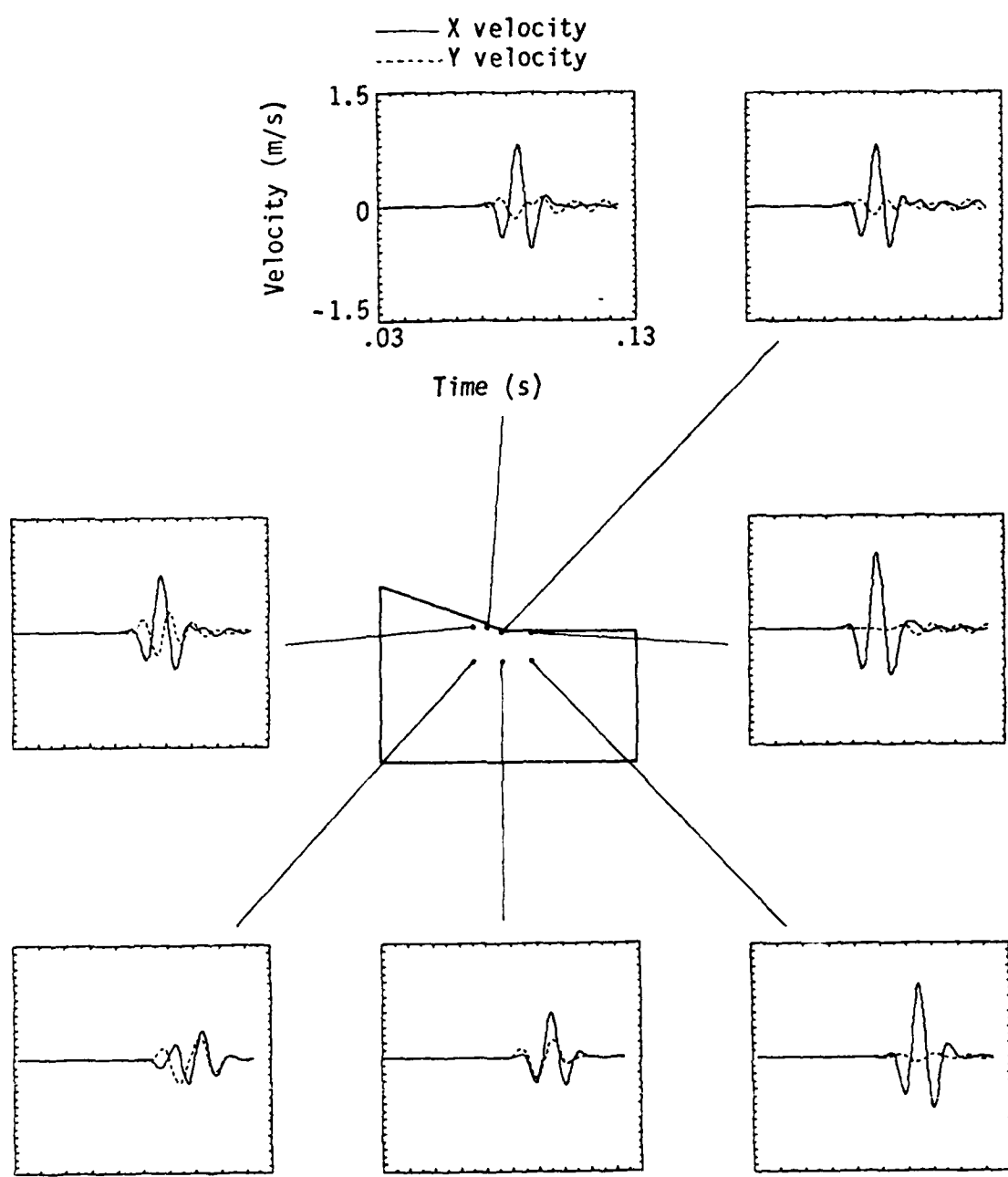


Figure 2-29. Time histories of diffracted field from SV-wave incidence to 20-degree mesa.

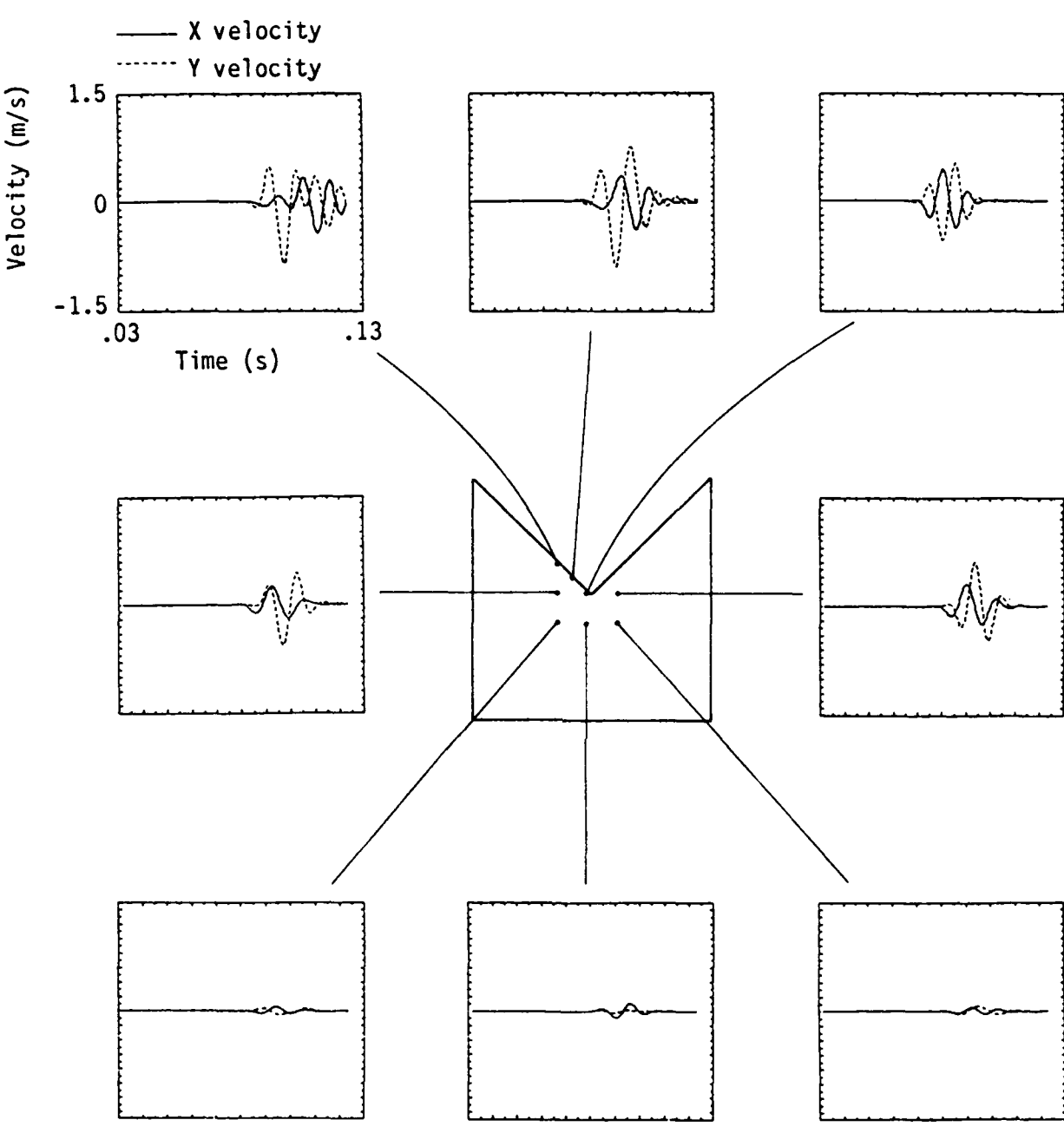


Figure 2-30. Time histories of diffracted field from SV-wave incidence to 90-degree mesa, offset 45 degrees.

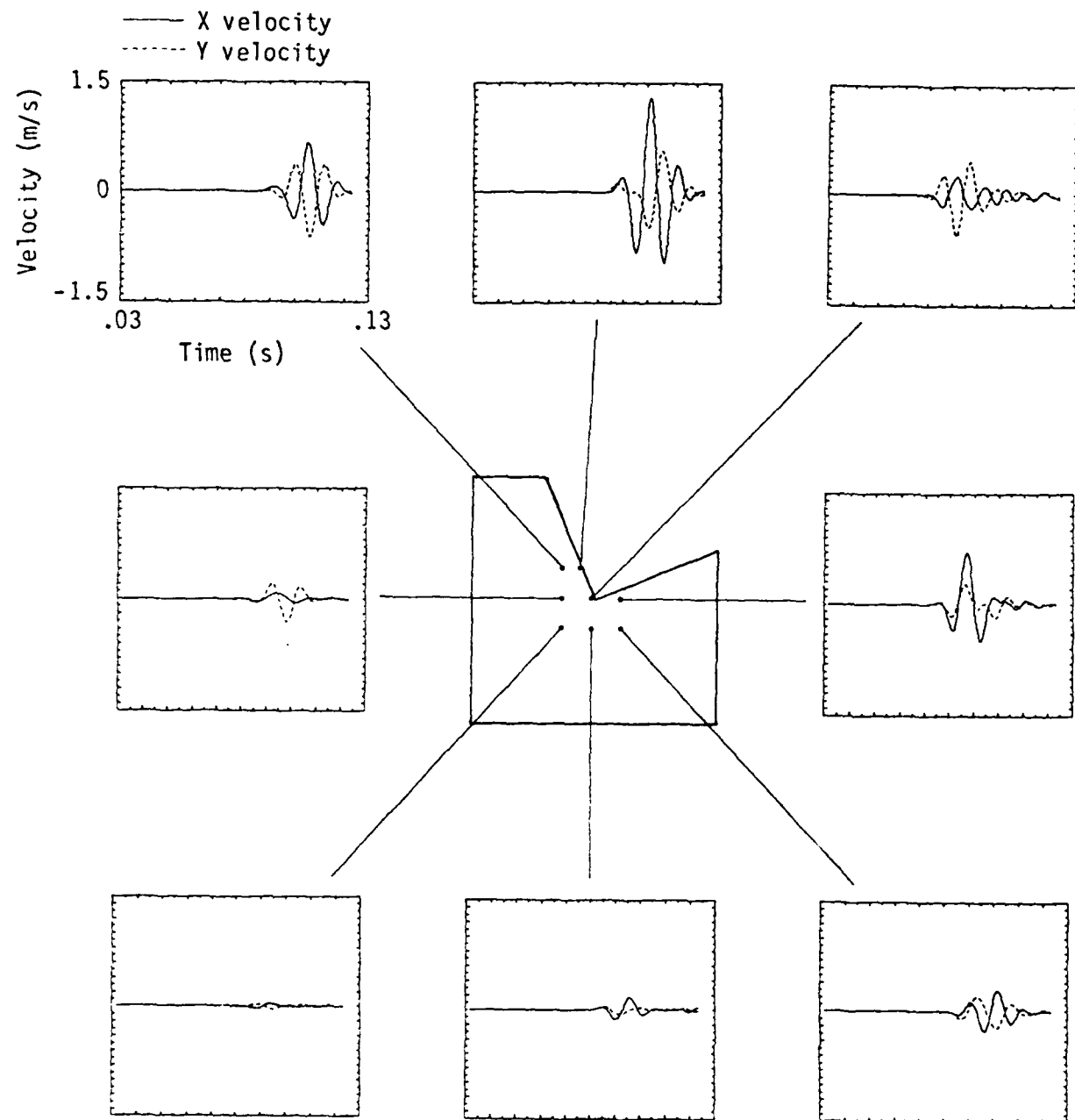
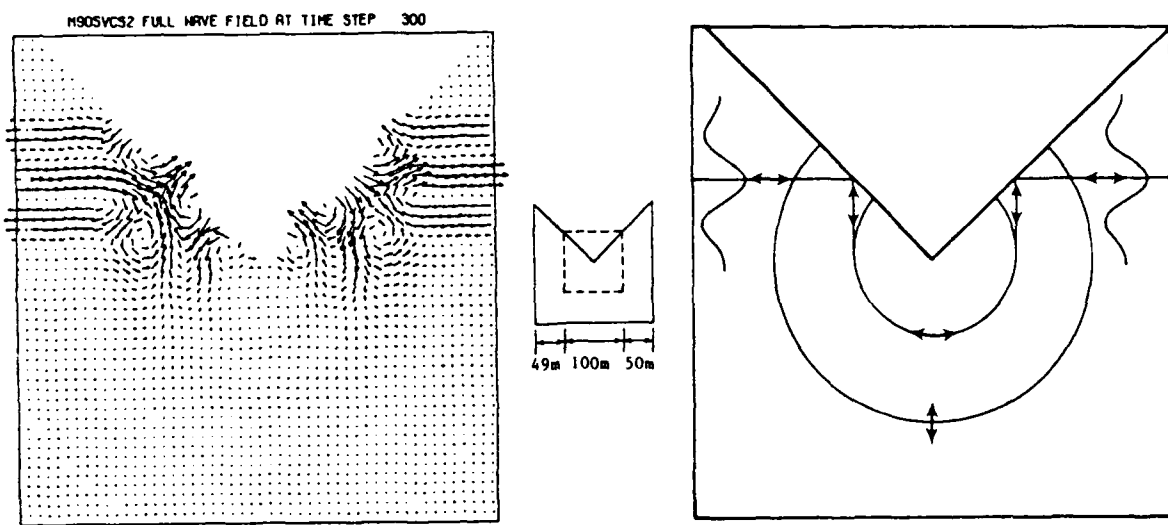
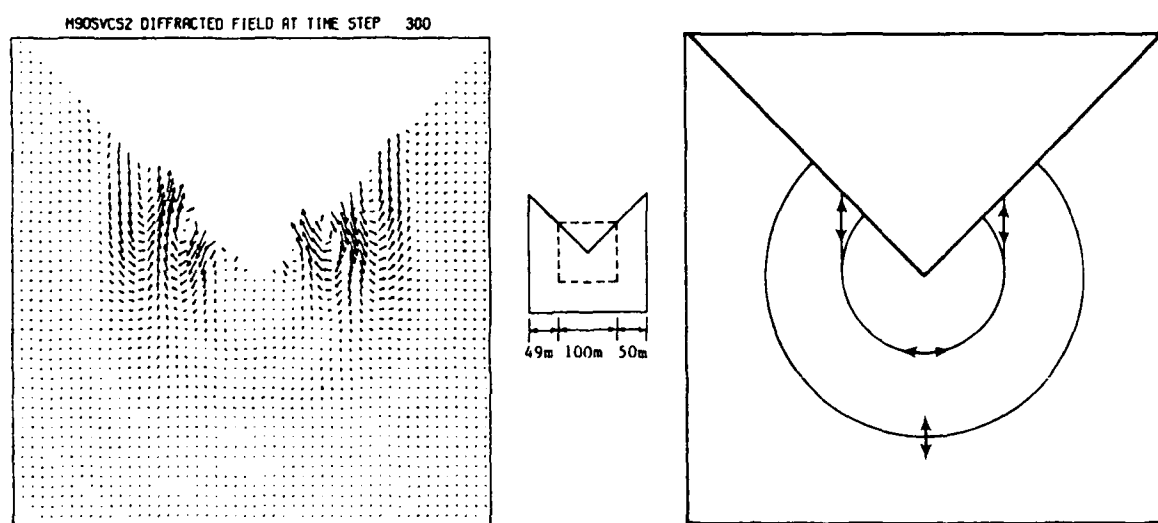


Figure 2-31. Time histories of diffracted field from SV-wave incidence to 90-degree mesa, offset 22.5 degrees.

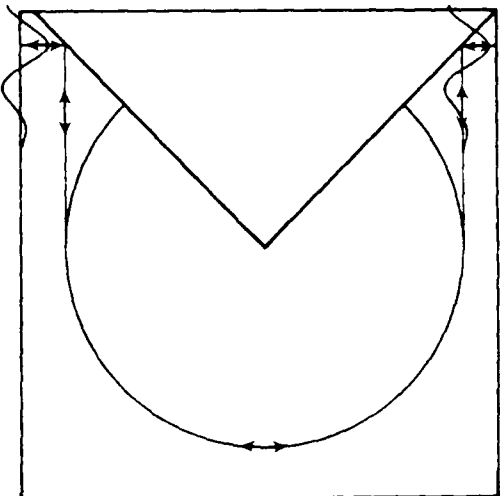
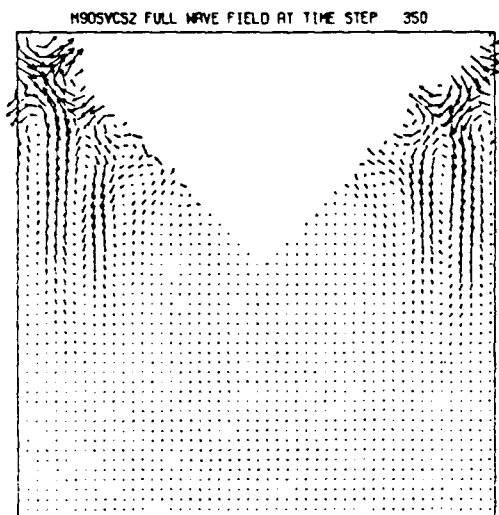


(a) Full wave field for center grid .

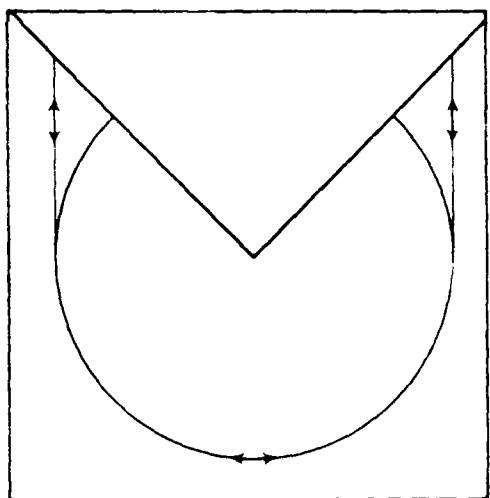
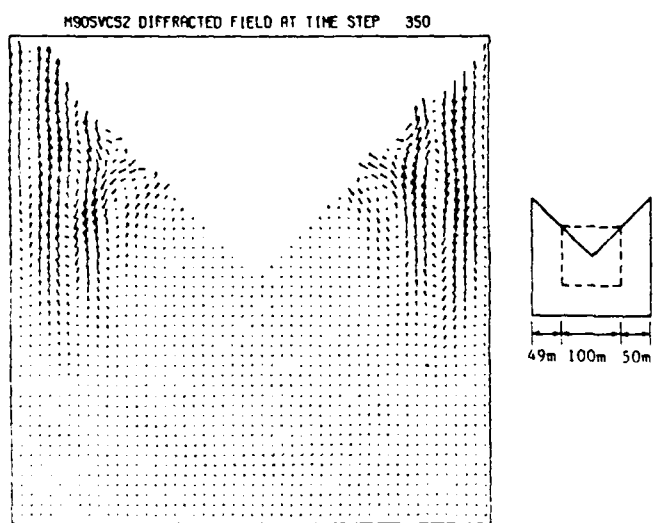


(b) Diffracted field for center grid

Figure 2-32. Diffractions at time 0.09238 s for SV-wave incidence to 90-degree mesa, offset 45 degrees.



(a) Full wave field for center grid



(b) Diffracted field for center grid

Figure 2-33. Diffractions at time 0.1078 s from SV-wave incidence to 90-degree mesa, offset 45 degrees.

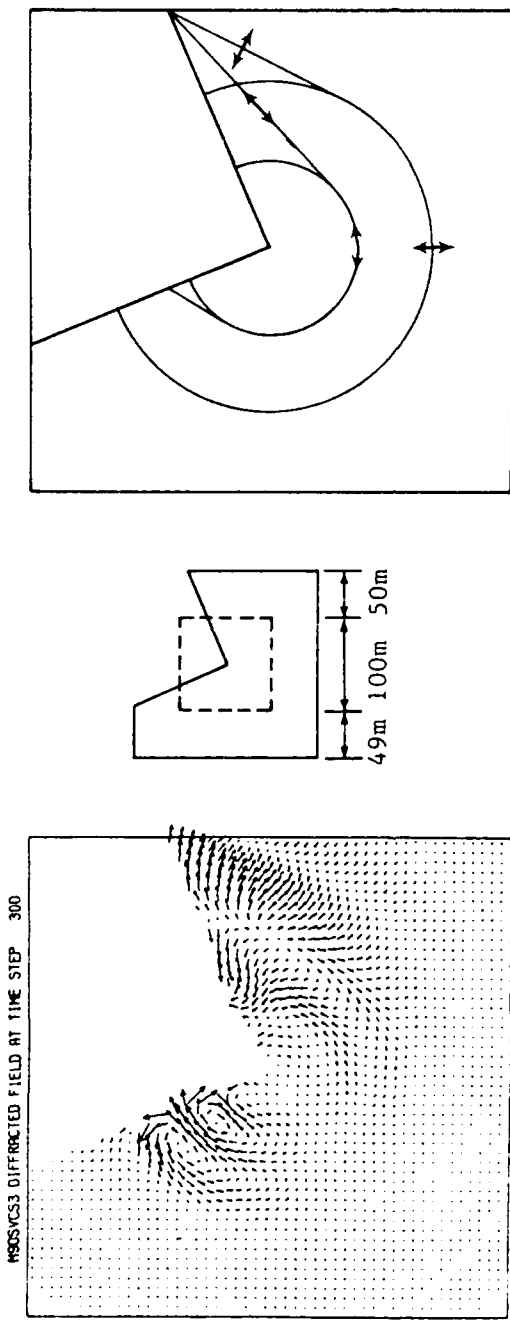
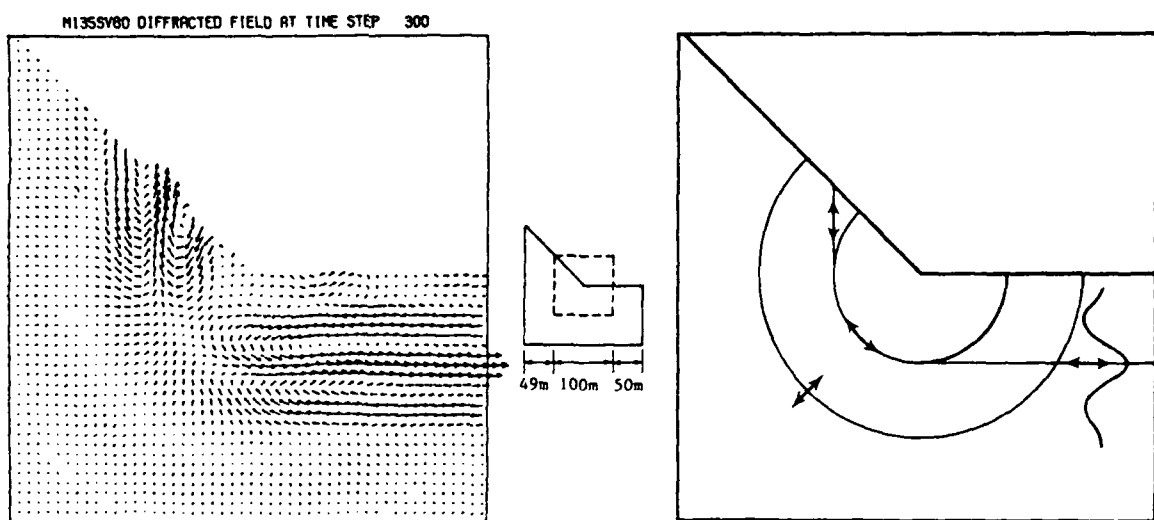
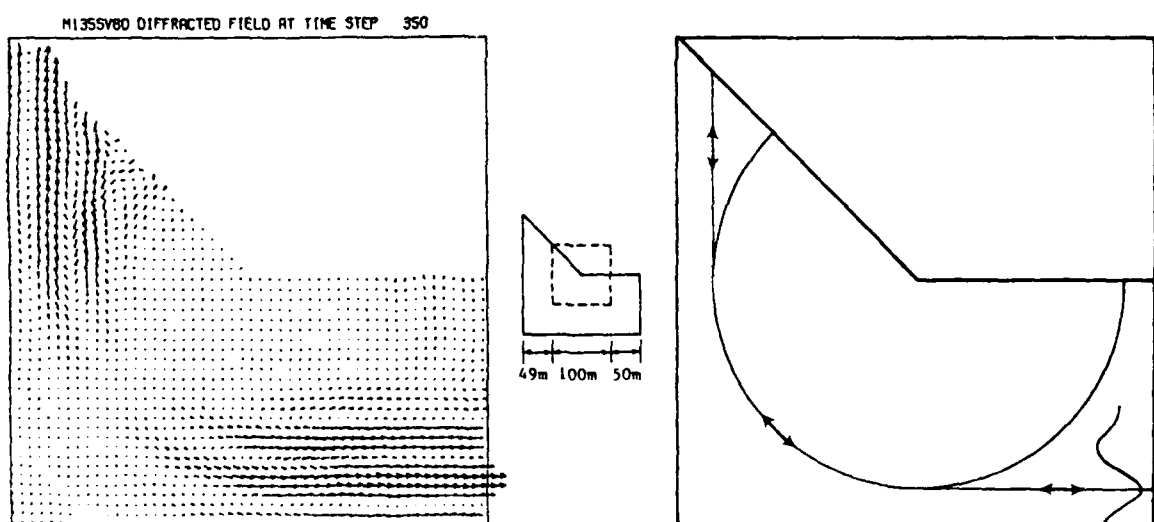


Figure 2-34. Diffraction at time 0.09238 s from SV-wave incidence to 90-degree mesa, offset 22.5 degrees, showing center position of grid.

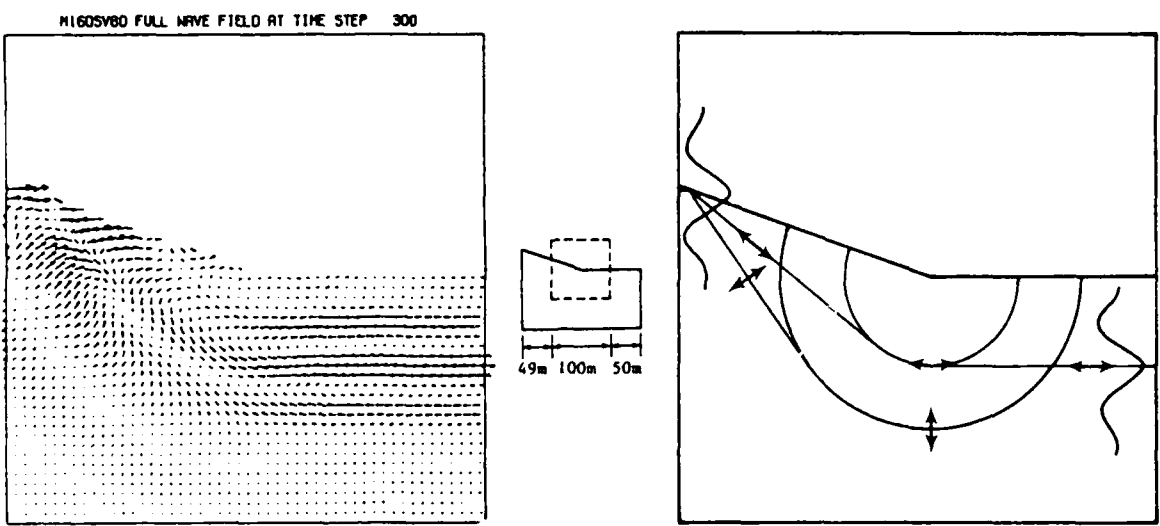


(a) Diffracted field for center grid at time 0.09238 s

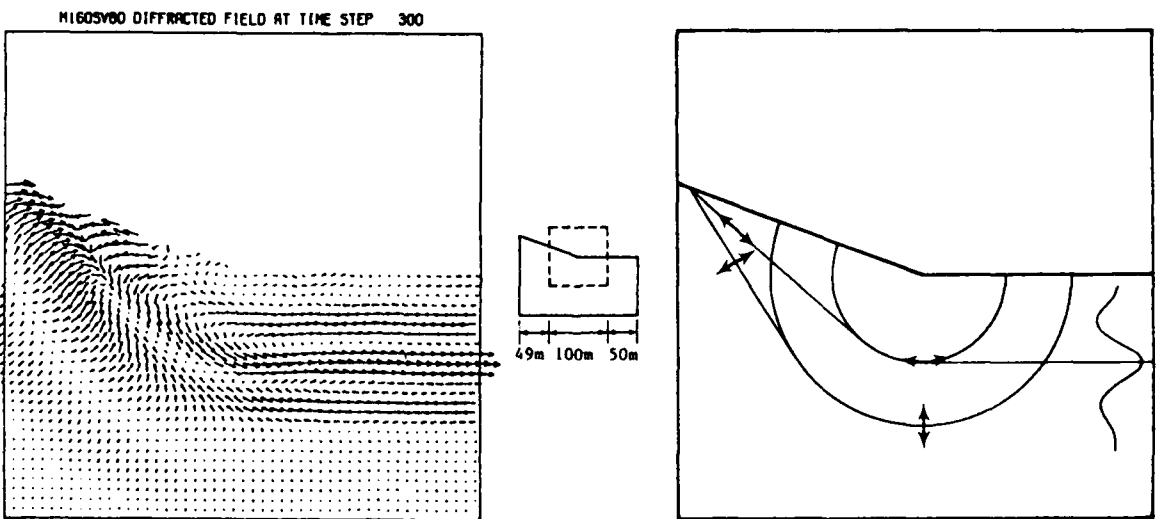


(b) Diffracted field for center grid at time 0.1078 s

Figure 2-35. Diffraction from SV-wave incidence to 45-degree mesa.



(a) Full wave field for center grid



(b) Diffracted field for center grid

Figure 2-36. Diffraction at time 0.09238 s from SV-wave incidence to 20-degree mesa.

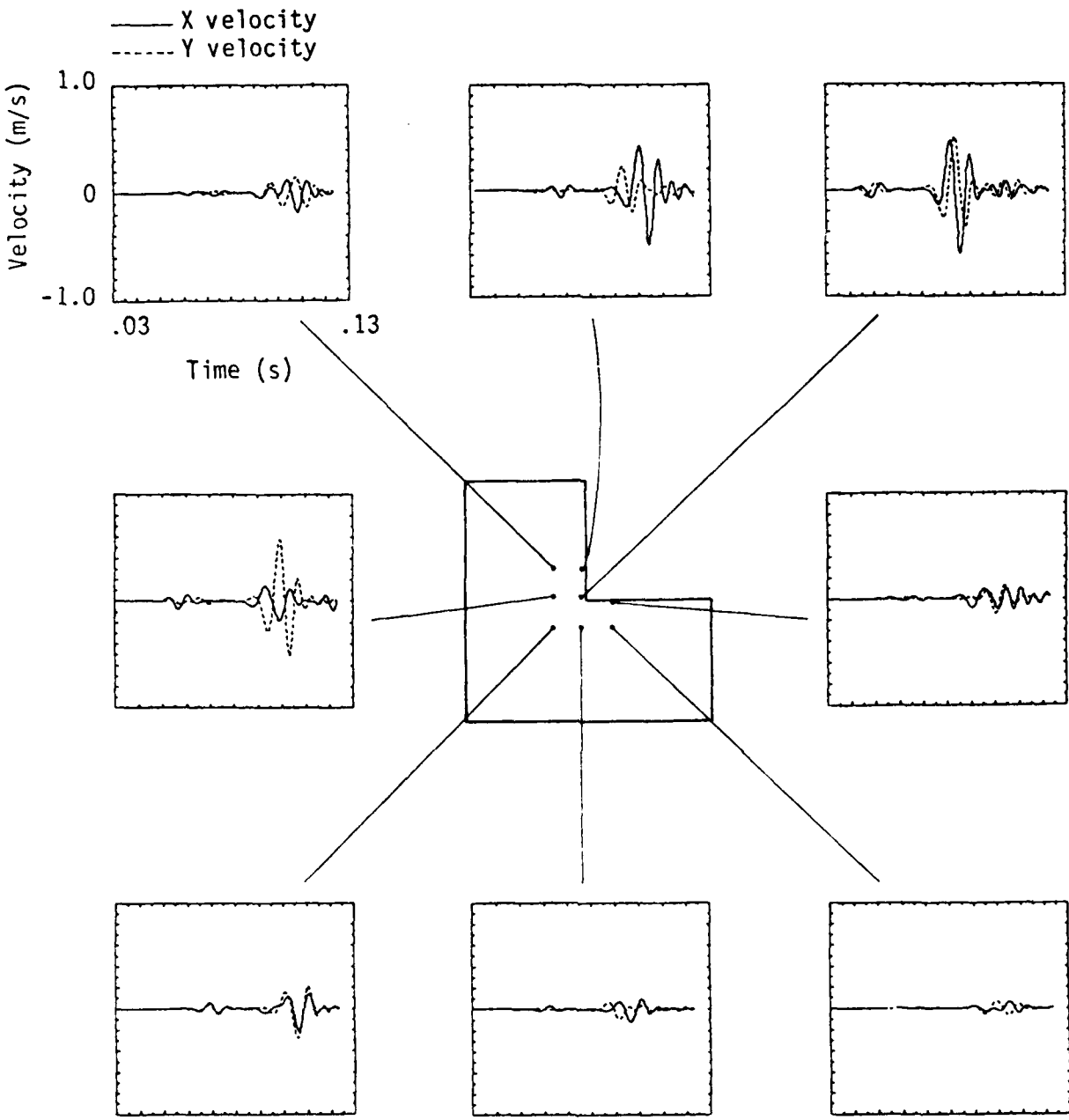


Figure 2-37. Time histories of diffracted field from Rayleigh wave incidence to 90-degree mesa.

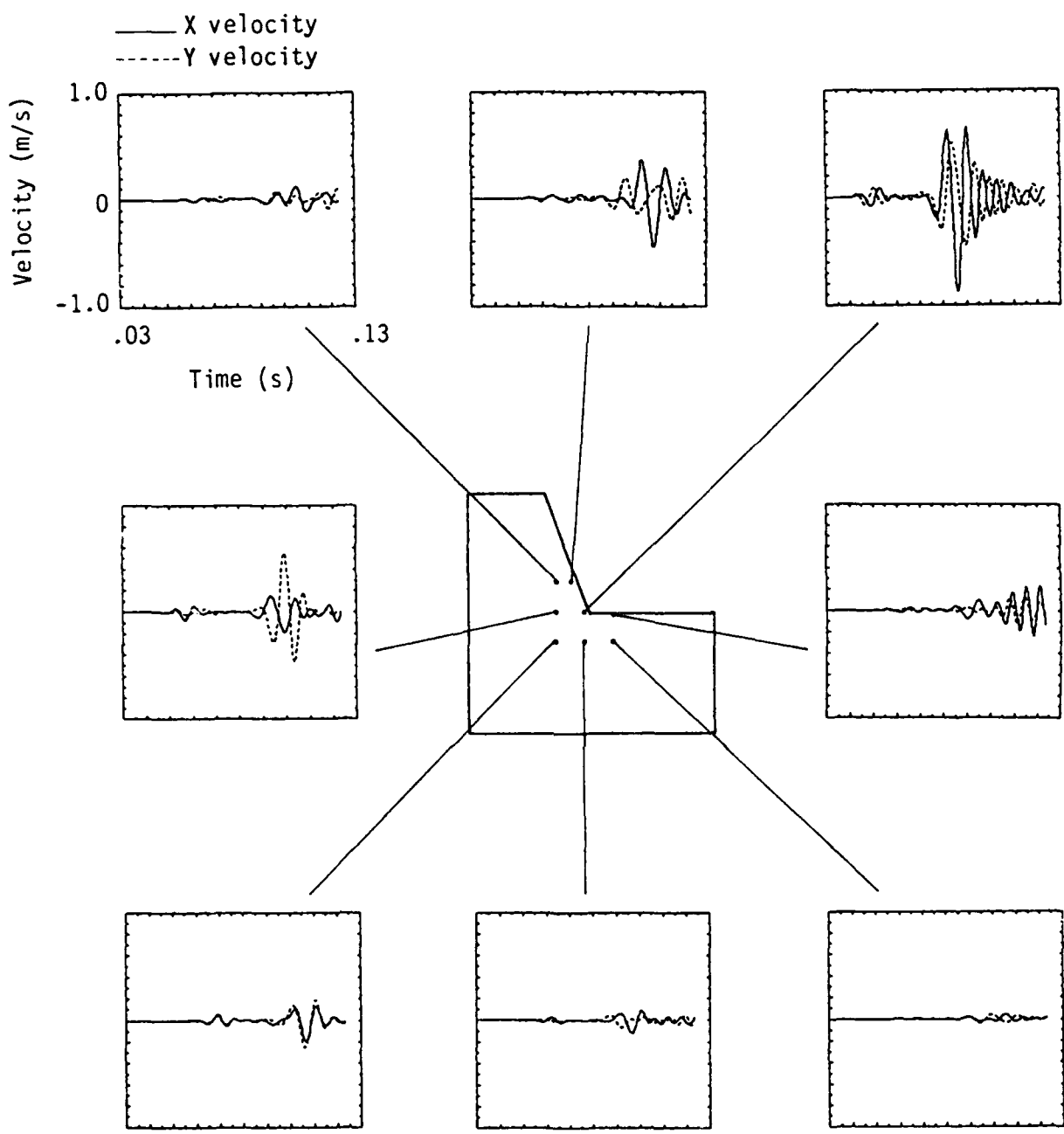


Figure 2-38. Time histories of diffracted field from Rayleigh wave incidence to 70-degree mesa.

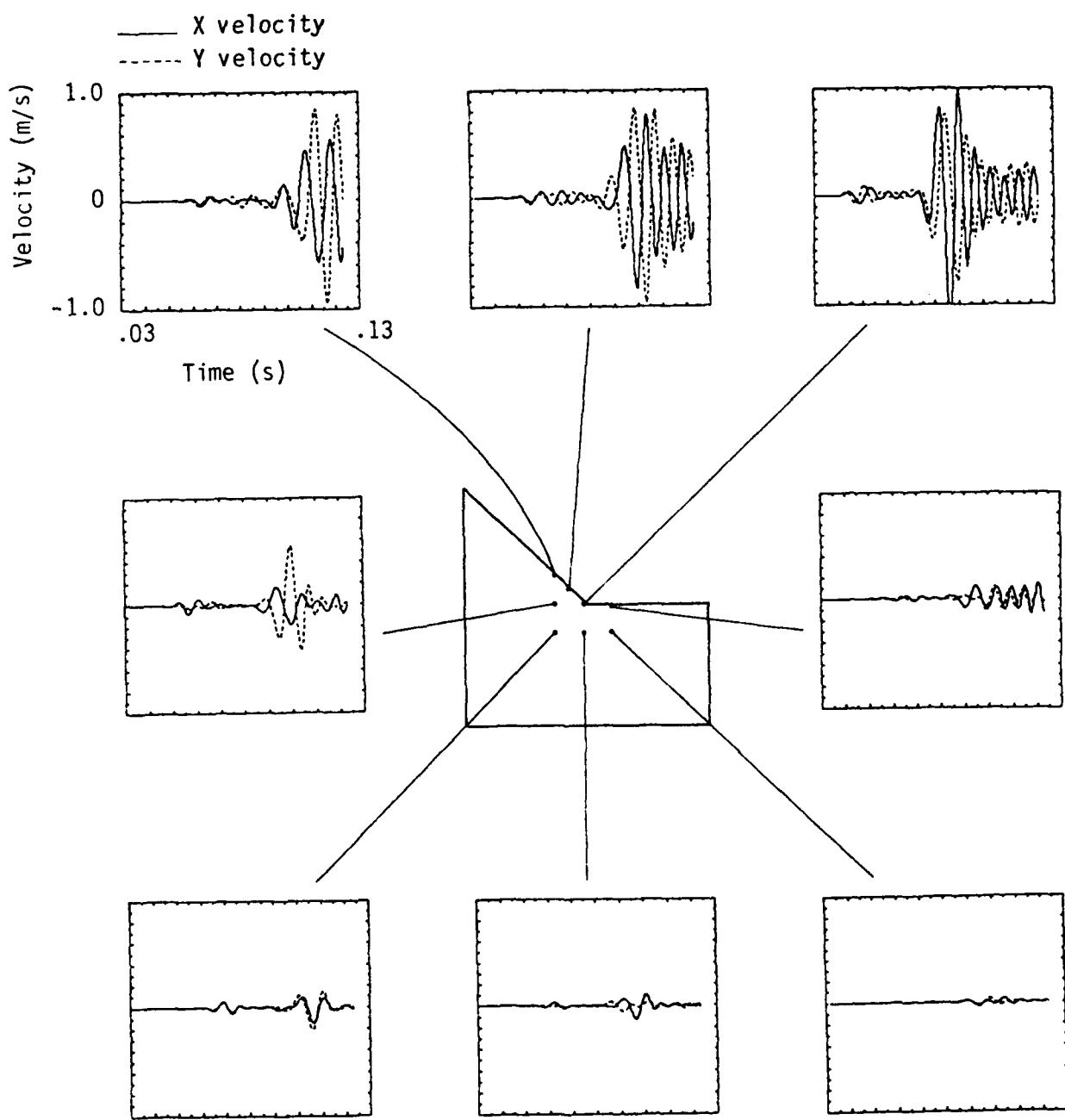


Figure 2-39. Time histories of diffracted field from Rayleigh wave incidence to 45-degree mesa.

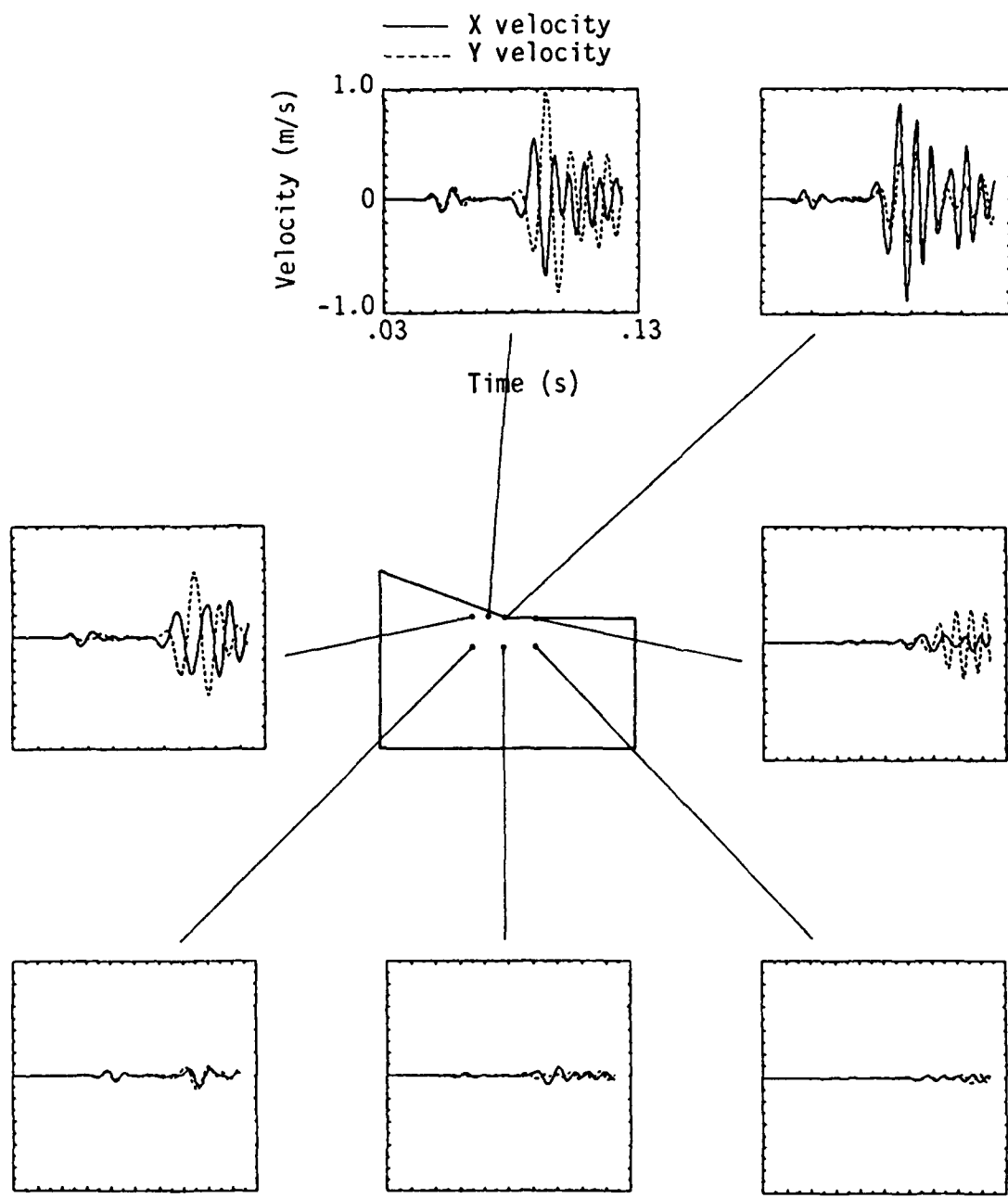


Figure 2-40. Time histories of diffracted field from Rayleigh wave input to 20-degree mesa.

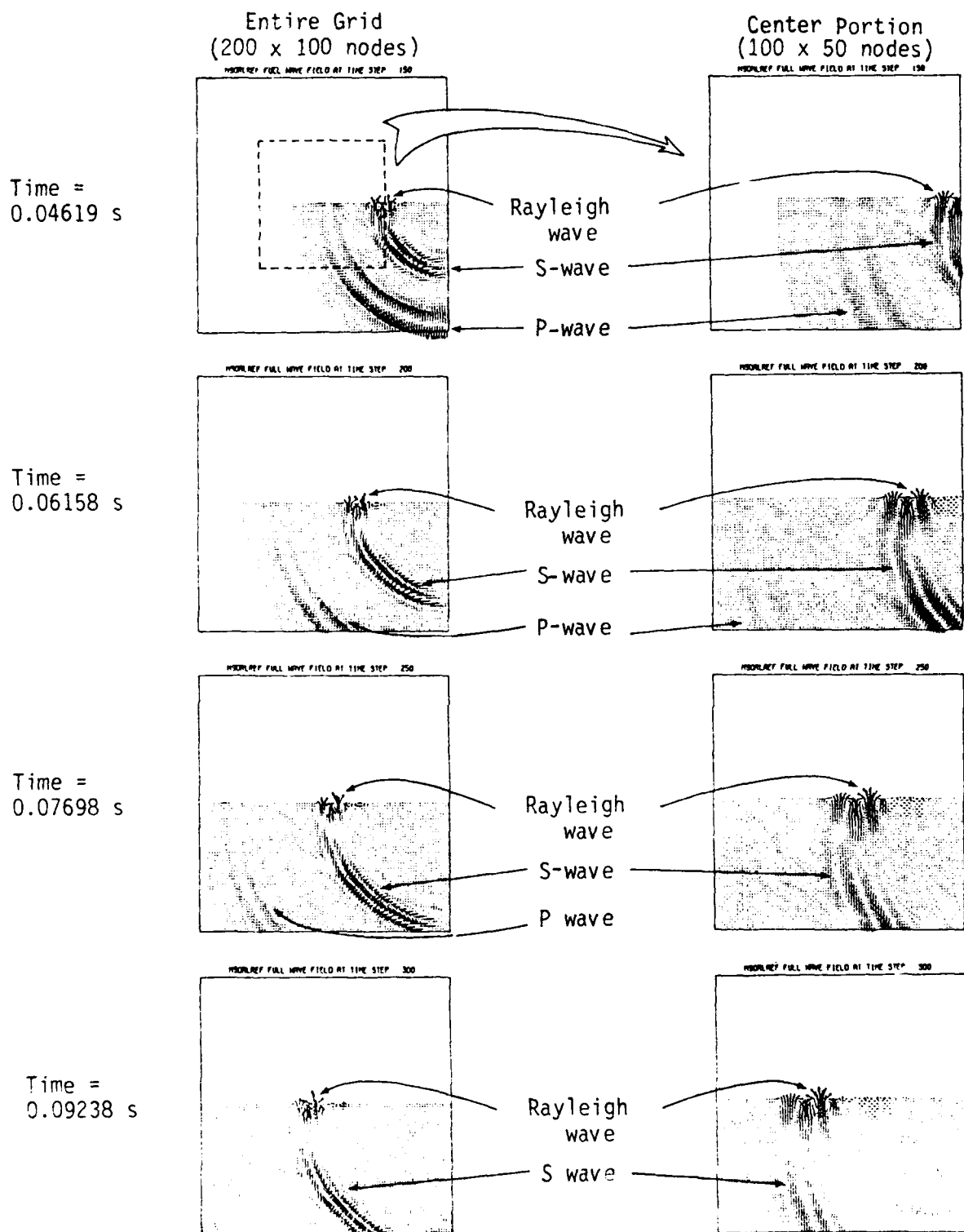
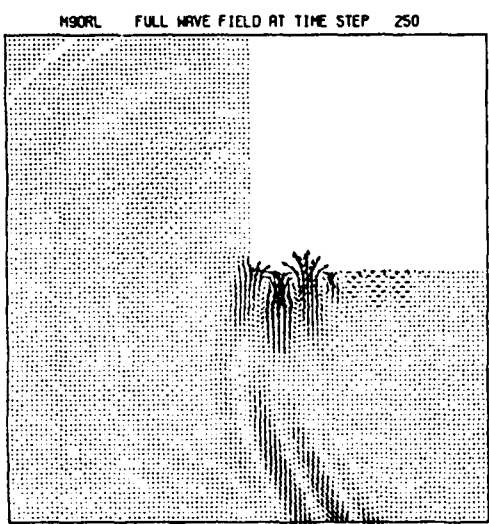
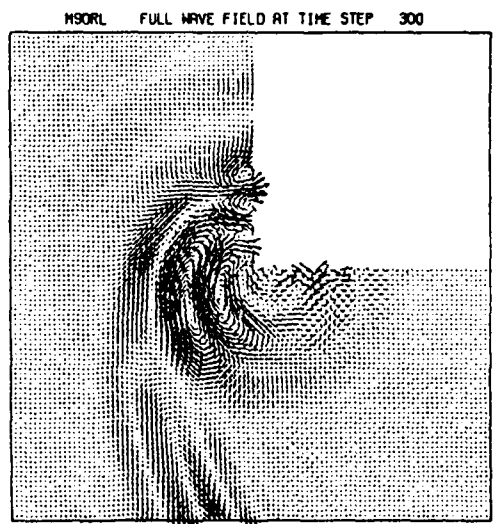


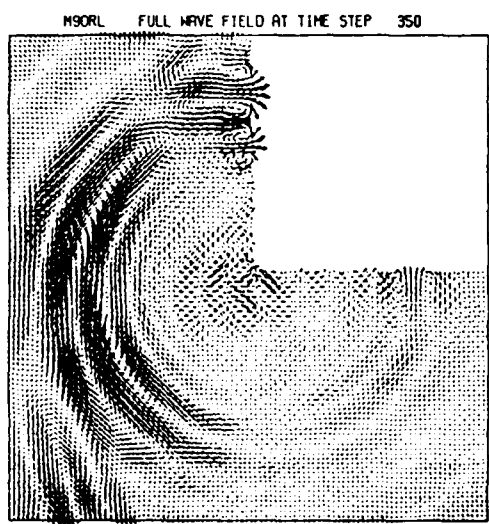
Figure 2-41. Reference field for Rayleigh wave incidence showing waves generated by wavelet loading over 5 nodes on 200 x 100 nodes halfspace.



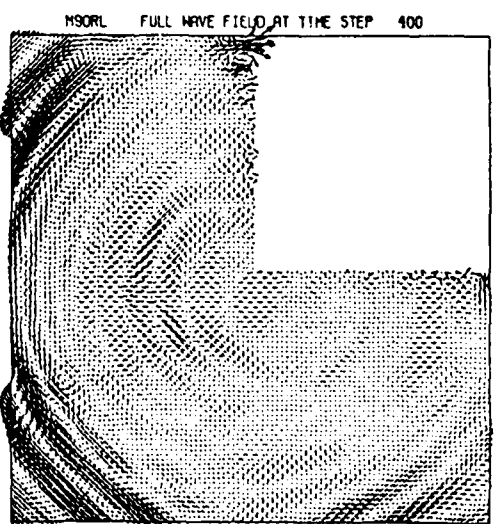
Time = 0.07698 s



Time = 0.09238 s

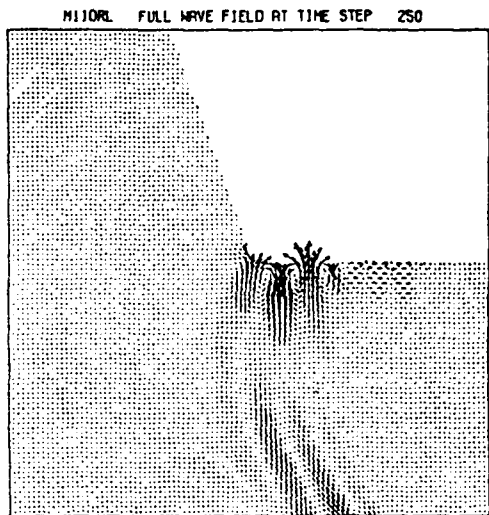


Time = 0.1078 s

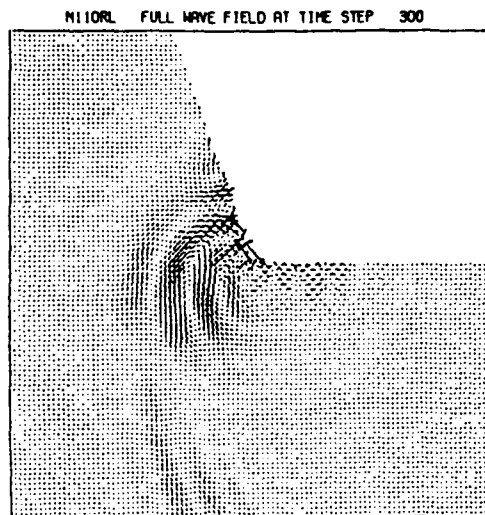


Time = 0.1232 s

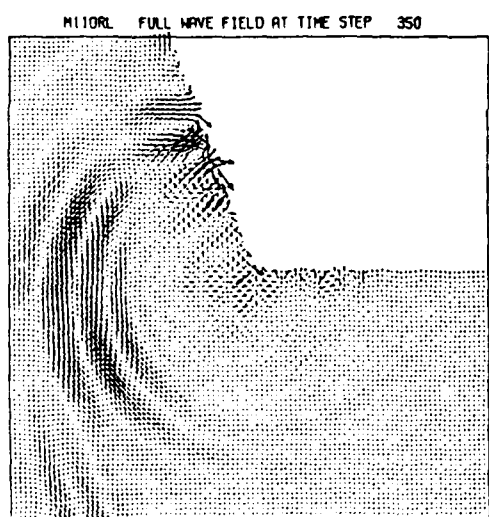
Figure 2-42. Diffractions from Rayleigh wave incidence to 90-degree mesa showing full wave field for center portion of the grid.



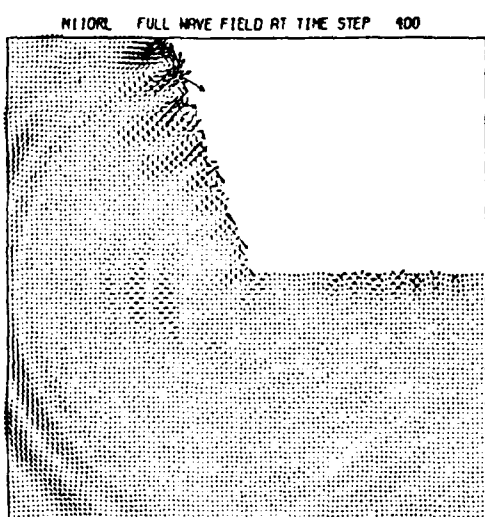
Time = 0.076998 s



Time = 0.09238 s

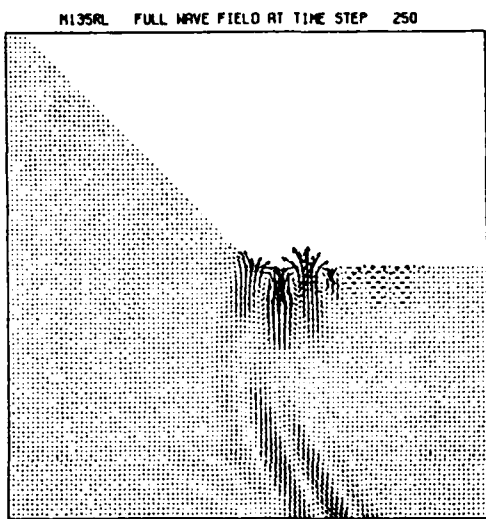


Time = 0.1078 s

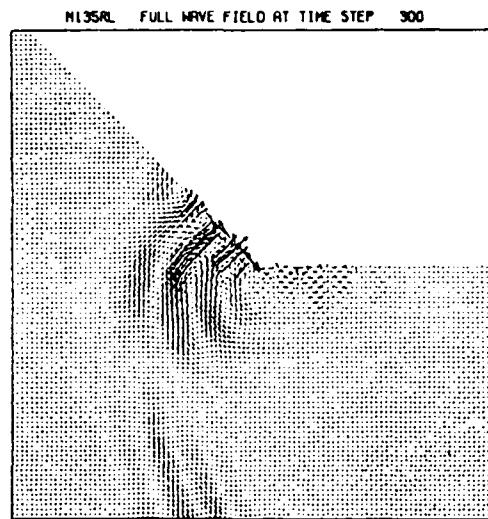


Time = 0.1232 s

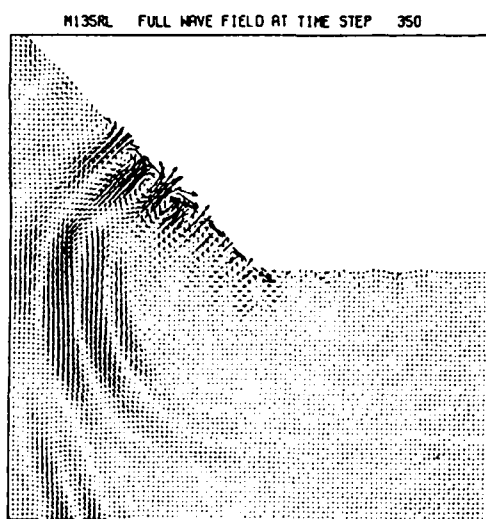
Figure 2-43. Diffractions from Rayleigh wave incidence to 70-degree mesa showing full wave field for the center portion of the grid.



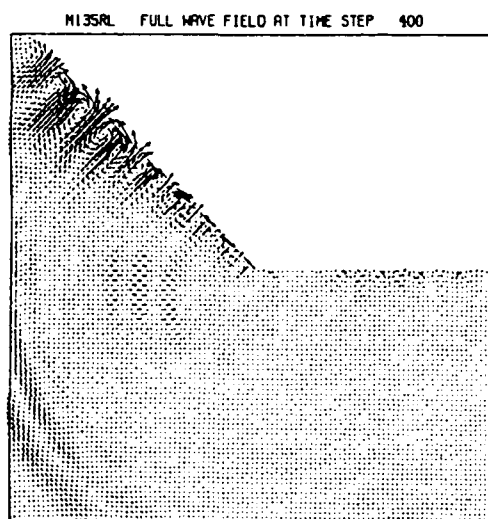
Time = 0.07698 s



Time = 0.09238 s



Time = 0.1078 s



Time = 0.1232 s

Figure 2-44. Diffractions from Rayleigh wave incidence to 45-degree mesa showing full wave field for the center portion of the grid.

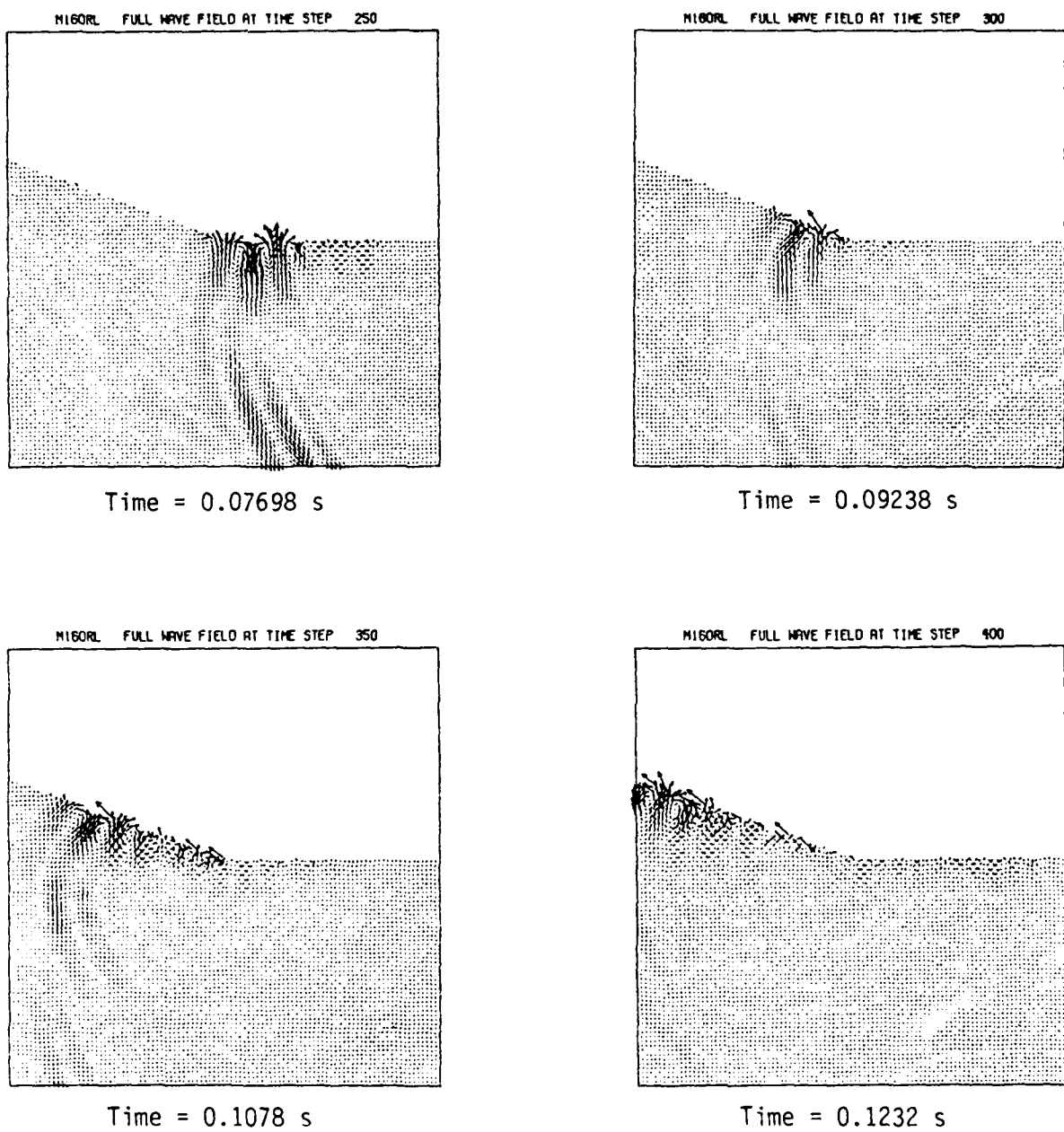


Figure 2-45. Diffractions from Rayleigh wave incidence to 20-degree mesa showing full wave field for the center position of the grid.

SECTION 3

SELF-SIMILAR THEORY OF VECTOR WAVE DIFFRACTION

3.1 INTRODUCTION

This section develops a new mathematical theory of vector wave diffraction. The theory is based on self-similar wave solutions in the so-called generalized diffractor, Fig. 3-1. This idealized diffractor, designated Π , is made of M contiguous sectors covering the plane from a common vertex. It simulates a wide variety of physical structures diffracting elastic, acoustic or electromagnetic waves.

Although many efforts have been made over the years to solve vector diffraction problems in applied physics, geophysics, and mechanics, they have all failed. These failures, however, are due to mathematical limitations rather than physics. In all cases, the underlying culprit is essential coupling of two or more wave functions at the vertex--excluding, in particular, separable solutions of the wave equations. Therefore, the following theory is based on a completely general vector formulation of wave equations and boundary conditions, with no further reference to physics. Since no characteristic length exists in the generalized diffractor, homogeneous solutions of degree zero (i.e., self-similar solutions) provide the basis for analysis.

The theory is presented in the following nine subsections, covering:
1) the governing vector equations; 2) homogeneous vector solutions; 3) the resulting vector boundary value problem (VBVP); 4) characteristic mapping of the boundaries; 5) normal forms of the VBVP; 6) solutions of all normal forms; 7) consistency conditions; 8) reduction to a vector integral equation; and 9) the canonical problem (two wave functions).

3.2 EQUATIONS GOVERNING THE GENERALIZED DIFFRACTOR

In two space dimensions, the generalized diffractor, Π consists of M semi-infinite wedges formed by M directed lines emanating from the common vertex. These directed lines (interfaces) partitioning the plane are identified by polar angles, L_m , $m = 1, M$, and their union is designated L . Geometry and polar coordinates are illustrated in Fig. 3-1.

A total of N wave functions, f_1 to f_N are supported by the diffractor in domains, Ω_n , $n = 1, N$. The number of wave functions per wedge is denoted

j_m , $m = 1, M$, and by definition each function satisfies a scalar wave equation. Consequently, the N -vector unknown, $f = (f_1 \dots f_N)^T$ is governed by the normal form of the vector wave equation (vector d'Alembertian),

$$\square f \equiv c^2 \Delta f - f_{tt} = 0 \quad \text{in } \Omega \quad (3-1)$$

where $\Delta f = f_{rr} + f_r/r + f_{\theta\theta}/r^2$ is the scalar Laplacian acting on the elements of f , and c is a diagonal $N \times N$ matrix of real constants. Partial derivatives are of course indicated by r , θ and t subscripts. This diagonal form of the operator, \square does not preclude off-diagonal terms in c , only requiring that the fuller matrix, e.g. \hat{c} , be diagonalized by a linear transformation, S as $c = S^{-1}\hat{c}S$, whence the solution is $\hat{f} = Sf$.

The N functions defined in M wedges are coupled by boundary conditions on set $\partial\Pi$, the union of Π -domain limit points. In addition to interfaces, L , these points include the limiting contour, $C = C_0 + C_\infty$ of circles bounding the vertex and infinity. The union of interfaces and contours is illustrated in Fig. 3-2. General boundary conditions on the limit points are written

$$\zeta f_r + \tau f_t + n f_\theta/r = g \quad \text{on } \partial\Pi = L + C \quad (3-2)$$

where ζ , τ and n are linearly independent (disjoint) $N \times N$ matrices and g is an N -vector.

The matrix coefficients and inhomogeneous vector in (3-2) are actually distributions on $\partial\Pi$ and represent sums over the union of contours, namely

$$\zeta = \sum_{m=1}^M \zeta_m, \quad \tau = \sum_{m=1}^M \tau_m, \quad n = \sum_{m=1}^M n_m, \quad g = \sum_{m=1}^M g_m$$

Terms in each sum are linearly independent by virtue of their definition on disjoint boundaries, with the common vertex point excluded by contour C_0 . On interface L_m , condition (3-2) prescribes $j_m + j_{m-1}$ equations in the same number of wave functions. On arc C_m , (3-2) prescribes j_m equations in j_m unknowns. The nonzero row and/or column elements in ζ_m , τ_m , n_m and g_m correspond to positions of the coupled functions in N -vector, f .

3.3 SELF-SIMILARITY AND HOMOGENEOUS VECTOR SOLUTIONS

Because the diffractor lacks a characteristic length, self-similar solutions of the governing equations, (3-1) and (3-2), are admissible. The most tractable and directly useful of these are homogeneous solutions of degree zero, i.e., functions where $f(r, \theta, t) = t^0 f(r/t, \theta)$. In principle, homogeneous

solutions of non-zero degree can be obtained by differentiation or integration of the degree zero solution.

Introducing the scalar similarity variable, $\rho \equiv r/t$ into the wave equation, (3-1) using the relation, $rf_r = -tf_t = \rho f_\rho$, gives

$$\rho^2(c^2 - \rho^2 I) f_{\rho\rho} + c^2 f_{\theta\theta} + \rho(c^2 - 2\rho^2 I) f_\rho = 0 \quad (3-3)$$

where I is the $N \times N$ identity matrix (ones on the main diagonal and zeros off).

The most effective approach to solving this self-similar form of the vector wave equation is to transform it to characteristic coordinates. The characteristic equation is readily found to be

$$\rho^2(c^2 - \rho^2 I)(d\theta)^2 + c^2(d\rho)^2 = 0$$

and solving for $d\theta/d\rho$ gives the differential equation

$$-\frac{d\theta}{d\rho} I = \beta_{\pm} = \pm c(\rho\sqrt{\rho^2 I - c^2})^{-1} = \frac{\pm d(\cos^{-1}c/\rho)}{d\rho}$$

The characteristic function, β_+ has a pole at $\rho = 0$, branch point at $\rho I = c$, and a double zero as $\rho \rightarrow \infty$. Principal values of the square root and inverse cosine functions are assumed, while multivaluedness is included explicitly with the \pm sign. Multiplying by $d\rho$ and integrating yields

$$z_{\pm} = \theta I \pm \cos^{-1}c/\rho = x \pm y \quad (3-4)$$

where the new coordinate matrices, $z_{\pm} = x \pm y$ are constants of integration.

Transforming the similarity form, (3-3) to characteristic coordinates by replacing the derivatives as

$$f_\theta = f_{z_+} + f_{z_-}, \quad f_\rho = \beta_+ f_{z_+} + \beta_- f_{z_-} \quad (3-5)$$

yields the normal vector form.

$$f_{z_+ z_-} = 0 \quad (3-6)$$

which of course can be integrated directly giving the classic solution

$$f(\rho, \theta) = F_+(z_+) + F_-(z_-). \quad (3-7)$$

3.4 THE VECTOR BOUNDARY VALUE PROBLEM

Particular solutions for F_{\pm} are determined from the boundary condition,

(3-2). Introducing the similarity variable, $\rho = r/t$ gives

$$\eta f_\theta/r + (\zeta - \rho\tau) f_\rho/t = g$$

Therefore, to admit homogeneous solutions, matrices ζ , η and τ must have the same degree of homogeneity, h say, while vector g is necessarily of degree $h-1$. This means that $g(r,t) = t^{h-1}g(\rho)$ and e.g., $\eta(r,t) = t^h\eta(\rho)$, whence dividing the above by t^{h-1} yields the boundary condition,

$$\eta/\rho f_\theta + (\zeta - \rho\tau) f_\rho = g(\rho) \quad (3-8)$$

Substituting (3-7) into (3-5), the partial derivatives of f become

$$f'_\theta = F'_+ + F'_-, \quad f'_\rho = \beta_+ F'_+ + \beta_- F'_- \quad (3-9)$$

Since $\beta_- = -\beta_+$ these can be written

$$F'_+ + F'_- = f'_\theta$$

$$F'_+ - F'_- = \beta_+^{-1} f'_\rho$$

Therefore, defining densities, d_\pm such that on the boundary

$$d_+ \equiv f'_\theta, \quad d_- \equiv \beta_+^{-1} f'_\rho \quad (3-10)$$

yields the following boundary value problem on $\partial\Pi$

$$F'_+ \pm F'_- \approx d_\pm \quad (3-11)$$

$$\eta/\rho d_+ + (\zeta - \rho\tau) \beta_+ d_- = g \quad (3-12)$$

for determination of F'_\pm in Ω . Because d_+ and d_- (i.e., f'_θ and f'_ρ) are not independent, the multivalued problem, (3-11) represents a consistency condition between f'_θ and f'_ρ .

3.5 CHARACTERISTIC MAPPINGS

The analytic functions, $F'_\pm(z_\pm)$ are determined by solving the boundary value problems defined in (3-11) and (3-12) on the limit set, $\partial\Pi$. The characteristics map $\partial\Pi$ to $\partial\Omega$, a semi-infinite rectangle in the z_+ (or z_-) plane enclosing the wave domain, Ω . Recall, because z_+ is a diagonal $N \times N$ matrix of characteristics, this mapped domain actually represents N complex planes.

The z_+ plane is illustrated in Fig. 3-3, and z_- is a simple reflection

about the x (real) axis. The bounds on x are $\vartheta < x < \vartheta + \omega$, where ϑ and ω are diagonal $N \times N$ matrices. Elements of ϑ define angles of the lower interfaces and those of ω define wedge angles, in the N wave domains. In particular, wedge m supports j_m wave functions, then for each of the j_m functions $\vartheta_n \equiv L_m$ and $\omega_n \equiv L_{m+1} - L_m$. The bounds on y are $-\infty \leq y \leq \pi/2$, where characteristics are real for $y > 0$ (hyperbolic subdomain) and complex for $y < 0$ (elliptic subdomain). The circular arc at infinity, C_∞ maps to the end of the rectangle at $y = \pi/2$, while the arc around the vertex, C_0 goes to the opposite end, at $y \rightarrow -\infty$.

The boundary value problem for F_\pm is complicated by the corners on $\partial\Omega$ and mixed behavior of the functions, i.e., hyperbolic-elliptic. These difficulties can be eliminated by a suitable transformation of the characteristics. Consider a succession of mappings beginning with the linear transformation,

$$\pi\omega^{-1}(z_\pm - \vartheta)$$

which scales the real coordinate of the wave domain between 0 and π . Taking the cosine,

$$\cos(\pi\omega^{-1}(z_\pm - \vartheta))$$

maps the boundary to the real axis, with z_+ and z_- domains going to the lower and upper halfplanes, respectively. The hyperbolic subdomain closure maps along characteristics to the real axis between $-I$ and $+I$. Finally, taking the reciprocal,

$$w = [\cos(\pi\omega^{-1}(z_\pm - \vartheta))]^{-1} \equiv u + iv \quad (3-13)$$

maps the elliptic z_+ subdomain to the upper halfplane, z_- to the lower and the wedge vertex to the origin. The hyperbolic subdomain maps entirely to the real axis, on $-I > u > I$.

The conformal mapping, $w(z_+)$ is illustrated in Fig. 3-4 and maps each interface, L_m to segments of the real axis in $j_m + j_{m-1}$ of the N wave domains. Endpoints of L , at $\rho = 0, \infty$ go to $w = 0, +u_\infty$, where $u_\infty = [\cos(\pi^2\omega^{-1}/2)]^{-1}$. For the j_m wave functions defined in wedge m (above interface m), L_m maps to $[0, +u_\infty]$, while for the j_{m-1} functions in wedge $m-1$ L_{m-1} maps to $[0, -u_\infty]$. These segments $[0, \pm u_\infty]$ extend from zero to the right or left respectively and typically wrap around $\pm\infty$.

3.6 REDUCTION OF $F'_+ \pm F'_- = d_{\pm}$ TO NORMAL FORMS

Since densities, $d_+ = f_\theta$ and $d_- = \beta_+^{-1}f_\rho$ are not independent, the multi-valued vector boundary value problem, (3-11) must first be solved for their relationship. Here they are reduced to certain normal forms, which will next be solved in general. By virtue of the conformal mapping, multivalued subscripts on F' now correspond to limits from above and below the real axis in the $w = u + iv$ plane, i.e.

$$F'_{\pm}(u) = \lim_{v \rightarrow 0_{\pm}} F'(w),$$

rather than characteristics. By contrast, subscripts on d merely distinguish righthand sides for the two boundary value problems.

The boundary value expression given by the minus sign in (3-11) defines the normal form,

$$F'_+ - F'_- = d_- \quad (3-14)$$

The remaining expression,

$$F'_+ + F'_- = d_+$$

can be reduced to normal form by introducing matrix functions, D_{\pm} which satisfy the homogeneous problem,

$$D_+ + D_- = 0 \quad (3-15)$$

Multiplying by D_+ and replacing $D_+ F'_-$ by $-D_- F'_+$ through (3-15) gives

$$D_+ F'_+ - D_- F'_- = D_+ d_+ \quad (3-16)$$

Finally, the boundary value problem for D_{\pm} , (3-15) is reduced to normal form by rewriting it as

$$D_+ D_-^{-1} = D_-^{-1} D_+ = -I$$

Because D_+ and D_-^{-1} commute, taking the principal value logarithm yields

$$\ln D_+ - \ln D_- = i\pi I \quad (3-17)$$

Thus, the original expression, (3-11) is equivalent to the three normal forms, (3-14), (3-16) and (3-17).

3.7 SOLUTION OF THE NORMAL FORM, $B_+ - B_- = b$

The normal boundary value problem is defined by (3-14), rewritten in general as

$$B_+ - B_- = b \quad (3-18)$$

To solve for $B(w)$, the inhomogeneous vector or matrix, b is replaced by an integral over $\partial\Omega$ using the sifting property of the delta function, i.e.,

$$b(u) = \frac{1}{2\pi i} \int_{\partial\Omega} ds \delta(s-u) b(s)$$

Factoring the diagonal matrix of delta functions, $\delta(s-u)$ as

$$\delta(s-u) = \frac{1}{2\pi i} \lim_{v \rightarrow 0_+} [s-w]^{-1} - \frac{1}{2\pi i} \lim_{v \rightarrow 0_-} [s-w]^{-1}$$

gives

$$b(u) = \lim_{v \rightarrow 0_+} \Sigma[w; b] - \lim_{v \rightarrow 0_-} \Sigma[w; b] = \Sigma_+ - \Sigma_-$$

where

$$\Sigma[w; b] \equiv \frac{1}{2\pi i} \int_{\partial\Omega} ds [s-w]^{-1} b(s) \quad (3-19)$$

The boundary values of Σ are found to be

$$\Sigma_{\pm}[u; b] = \pm \frac{1}{2} b(u) + \Sigma_p(u; b) \quad (3-20)$$

where Σ_p is the principal value integral, i.e., $\Sigma[u; b]$ in (3-19) with the point $s = u$ excluded. Clearly a particular solution for $B(w)$ is

$$B(w) = \Sigma[w; b] \quad (3-21)$$

3.8 THE CONSISTENCY CONDITION ON DENSITIES

Normal forms of the multivalued boundary value problems on F'_{\pm} can now be solved. From (3-14) the solution in terms of d_- is

$$F'_+ - F'_- = d_- \implies F'(w) = \Sigma[w; d_-] \quad (3-22)$$

while for d_+ , (3-16) and (3-17) yield

$$F'_+ + F'_- = d_+ \implies F'(w) = D^{-1}(w) \Sigma[w; D_+ d_+] \quad (3-23)$$

Boundary values of these solutions are

$$F'_\pm(u) = \begin{cases} \frac{1}{2}d_- + \Sigma_p[u; d_-] \\ \frac{1}{2}d_+ \pm D_+^{-1}\Sigma_p[u; D_+d_+] \end{cases} \quad (3-24)$$

which must be equal, whence, equating singlevalued parts and multivalued parts gives the consistency conditions,

$$\frac{1}{2}d_+ = \Sigma_p[u; d_-] \quad (3-25)$$

$$\frac{1}{2}d_- = D_+^{-1}\Sigma_p[u; D_+d_+] \quad (3-26)$$

This integral transform pair provides the relation between densities d_\pm on the boundary. Eliminating d_+ or d_- yields an integral equation for each as

$$\frac{1}{4}d_+ = \Sigma_p[u; D_+^{-1}\Sigma_p[s; D_+d_+]] \quad (3-27)$$

$$\frac{1}{4}d_- = D_+^{-1}\Sigma_p[u; D_+\Sigma_p[s; d_-]] \quad (3-28)$$

To complete these expressions, (3-17) is solved for $\ln D(w)$ using (3-21), as

$$\ln D(w) = \Sigma[w; i\pi I] = \frac{1}{2} \int_{\partial\Omega} ds [s-w]^{-1}$$

Taking the matrix exponential gives

$$D(w) = e^{i\pi\Sigma[w]} \quad (3-29)$$

where $\Sigma[w] \equiv \Sigma[w; I]$, and from (3-20), boundary values are

$$D_\pm(u) = e^{i\pi(\pm I/2 + \Sigma_p[u])} = \pm ie^{i\pi\Sigma_p[u]}$$

3.9 REDUCTION OF THE BOUNDARY VALUE PROBLEM TO AN INTEGRAL EQUATION

To solve the boundary condition equation, (3-12), d_+ or d_- is replaced through (3-25) or (3-26). Since the normal form of solution for $F'(w)$ is given by (3-22) in terms of d_- , it is natural to eliminate d_+ . Therefore, inserting (3-25) in (3-12) gives the integral equation.

$$2n/\rho\Sigma_p[u; d_-] + (\zeta - \rho\tau)\beta_+d_- = g \quad (3-31)$$

However, in order for this to be self-consistent, d_- must also satisfy the consistency integral equation, (3-28). These equations are combined by operating on (3-31) with $\Sigma_p[u; \rho D_+ n^{-1}]$, whence

$$2\Sigma_p[u; D_+ \Sigma_p[u; d_-]] + \Sigma_p[u; \rho D_+ n^{-1}(\zeta - \rho\tau)\beta_+ d_-] = \Sigma_p[u; \rho D_+ n^{-1}g]$$

and replacing the double integral by (3-28), giving

$$\frac{1}{2}D_+ d_- + \Sigma_p[u; \rho D_+ n^{-1}(\zeta - \rho\tau)\beta_+ d_-] = \Sigma_p[u; \rho D_+ n^{-1}g] \quad (3-32)$$

This equation is valid provided n^{-1} exists. If n is not invertible, the implication is that elements of vector d_- are linearly dependent, i.e., some degree of degeneracy exists. To proceed with this singular case, however, physics must be invoked to evaluate admissible forms of n , ζ , τ , and g .

The single integral equation, (3-32) is the final, self-consistent expression of the boundary value problem, (3-11) and (3-12). By virtue of its N-vector unknown and dependence on N complex variables, no standard analytical reduction of the problem appears possible. Thus, to determine $F'(w)$ it is necessary to solve (3-32) for d_- on $\partial\Omega$ and evaluate $\Sigma[w; d_-]$. In full, this gives $F'(w)$ as

$$F'(w) = \Sigma_p[u; d_-] \equiv \frac{1}{2\pi i} \int_{\partial\Omega} ds [s-w]^{-1} d_-(s) \quad (3-33)$$

by solving

$$\frac{1}{2}D_+ d_- + \Sigma_p[u; v^{-1}\mu d_-] = \Sigma_p[u; v^{-1}g] \quad (3-34)$$

where

$$\begin{aligned} v &= n D_+^{-1}/\rho, \quad D_+ = ie^{i\pi\Sigma_p[u]} \\ \mu &= (\zeta - \rho\tau)\beta_+, \quad \beta_+ = c(\rho\sqrt{\rho^2 I - c^2})^{-1} \end{aligned} \quad (3-35)$$

Direct integration yields $F(w)$ as

$$F(w) = \frac{1}{2\pi i} \int_{\partial\Omega} ds \ln[s-w] d_-(s) \quad (3-36)$$

where $\ln[s-w]$ is a diagonal matrix of logarithms and initial conditions are specified on the mapping of C_∞ to $\partial\Omega$.

3.10 THE CANONICAL PROBLEM, N=2

The generality of this formal solution for $F'(w)$, (3-33) in terms of a singular integral equation precludes further resolution of the actual computational problem. To proceed, it is necessary to consider a specific class of problem solutions. In particular, specializing to the lowest order vector problem, $N=2$ yields the (binary) canonical diffraction problem. This involves only two wave functions, either with both supported in one wedge, $M=1$, or one supported in each of two wedges, $M=2$. Thus, the binary problem is in terms of 2-vectors and 2×2 matrices only.

Rather than consider specific boundary conditions, i.e., values of η, ζ and τ in (3-2), because they are disjoint and 2×2 , their general structure can be determined. In particular, there are only three possible pairs of disjoint 2×2 matrices, namely

$$\begin{pmatrix} 1 & 0 \\ 0 & 1 \end{pmatrix}, \begin{pmatrix} 0 & 1 \\ 1 & 0 \end{pmatrix}$$

$$\begin{pmatrix} 1 & 1 \\ 0 & 0 \end{pmatrix}, \begin{pmatrix} 0 & 0 \\ 1 & 1 \end{pmatrix}$$

$$\begin{pmatrix} 1 & 0 \\ 1 & 0 \end{pmatrix}, \begin{pmatrix} 0 & 1 \\ 0 & 1 \end{pmatrix}$$

The first pair is invertible (nonsingular), while the other two are not (singular). Consideration of typical boundary conditions in physical problems show that the first pair of matrices corresponds to the $M=1$ case, the second pair to $M=2$, while the third corresponds to a degenerate scalar case which will be neglected. The canonical coefficients can therefore be written,

$$M=1; v = a(\rho) \begin{pmatrix} 1 & 0 \\ 0 & 1 \end{pmatrix}, \mu = b(\rho) \begin{pmatrix} 0 & 1 \\ 1 & 0 \end{pmatrix} \quad (3-37)$$

$$M=2; v = \begin{pmatrix} 1 & 1 \\ 0 & 0 \end{pmatrix} a(\rho), \mu = \begin{pmatrix} 0 & 0 \\ 1 & 1 \end{pmatrix} b(\rho) \quad (3-38)$$

where $a(\rho)$ and $b(\rho)$ are 2×2 diagonal matrices which depend on the specific application.

The M=1 case satisfies the assumptions made in deriving the integral equation, (3-34), hence, substituting (3-37) into (3-34) yields the 2-vector equation

$$\frac{1}{2} \begin{pmatrix} D_1 d_1 \\ D_2 d_2 \end{pmatrix} + \sum_p [u; \begin{pmatrix} (b_1/a_1)d_2 \\ (b_2/a_2)d_1 \end{pmatrix}] = \sum_p [u; \begin{pmatrix} g_1/a_1 \\ g_2/a_2 \end{pmatrix}] \quad (3-39)$$

where subscripts on D and d are dropped for convenience. The position reversal of d_1 and d_2 in the integral operator precludes further simplification (without introducing a multiple-integral scalar equation). However, the final system of equations is solvable using successive approximations. Writing it as

$$\begin{pmatrix} d_1 \\ d_2 \end{pmatrix} = 2D^{-1} \left\{ -\sum_p [u; \begin{pmatrix} (b_1/a_1)d_2 \\ (b_2/a_2)d_1 \end{pmatrix}] + \sum_p [u; \begin{pmatrix} g_1/a_1 \\ g_2/a_2 \end{pmatrix}] \right\} \quad (3-40)$$

and assuming starting values for d_1 and d_2 , this recurrence relation yields a new approximation for d_2 and d_1 respectively. Repeating the process yields successively better approximations for vector d.

The singular M=2 case does not satisfy the assumption leading to the formal solution (3-34), i.e., existence of v^{-1} . It is necessary therefore to directly examine boundary condition, (3-12), rewritten as

$$vd_+ + \mu d_- = g.$$

Substituting (3-38) gives two equations relating components of d_+ and d_- ,

$$\begin{aligned} a_1 d_{1-} + a_2 d_{2-} &= g_1 \\ b_1 d_{1+} + b_2 d_{2+} &= g_2 \end{aligned} \quad (3-41)$$

Eliminating d_+ in (3-41) through (3-25) gives the scalar equation

$$b_1 \sum_p [u_1; d_{1-}] - b_2 \sum_p [u_2; a_1/a_2 d_{1-}] = g_2/2 - b_2 \sum_p [u_2; g_1/a_2] \quad (3-42)$$

while eliminating d_- through (3-26) gives

$$a_1/D_1 \sum_p [u_1; D_1 d_{1+}] - a_2/D_2 \sum_p [u_2; D_2 (b_1/b_2) d_{1+}] = g_1/2 - a_2/D_2 \sum_p [u_2; D_2 g_2/b_2] \quad (3-43)$$

These integral equations can be solved for d_{1-} and d_{1+} respectively, and the other components follow from (3-41). Since the resulting solutions for d_+ and d_- are not independent, clearly one or the other is redundant. This

can only be the case if components of the g vector are dependent, i.e., $g_2 = g_2(g_1)$. Therefore, in the $M=2$ case (for which v^{-1} and μ^{-1} do not exist) this singular problem can only be solved if g is a degenerate vector.

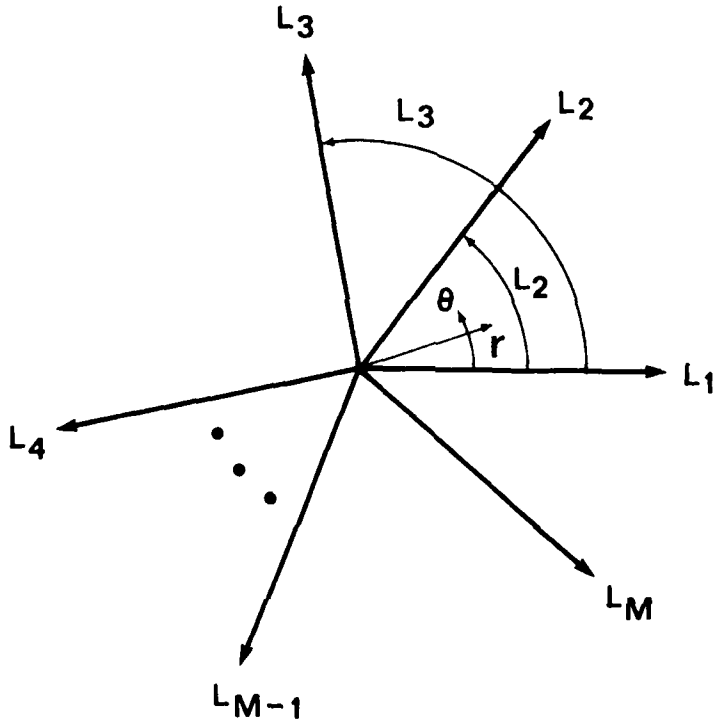


Figure 3-1. The generalized plane diffractor, consisting of M semi-infinite wedges formed by directed lines from the vertex. The lines (interfaces) are designated by their polar angles, L_m , $m = 1, M$.

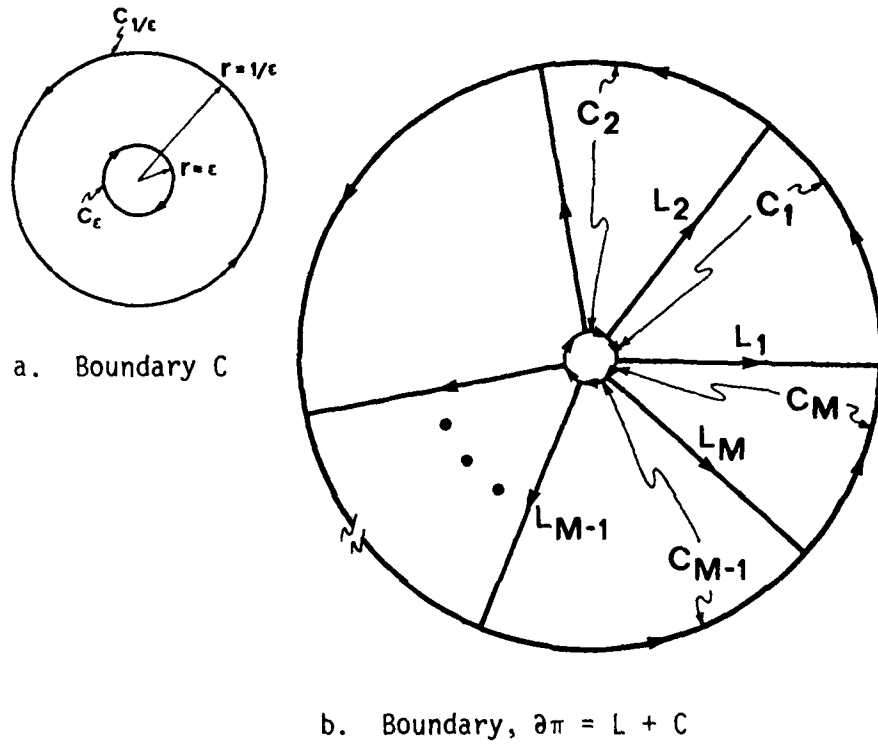


Figure 3-2. a) Definition of contour C bounding the limit points at $r = 0$ and ∞ (as $\epsilon \rightarrow 0$).
 b) Cartoon of the complete set of limit points defining the generalized diffractor.

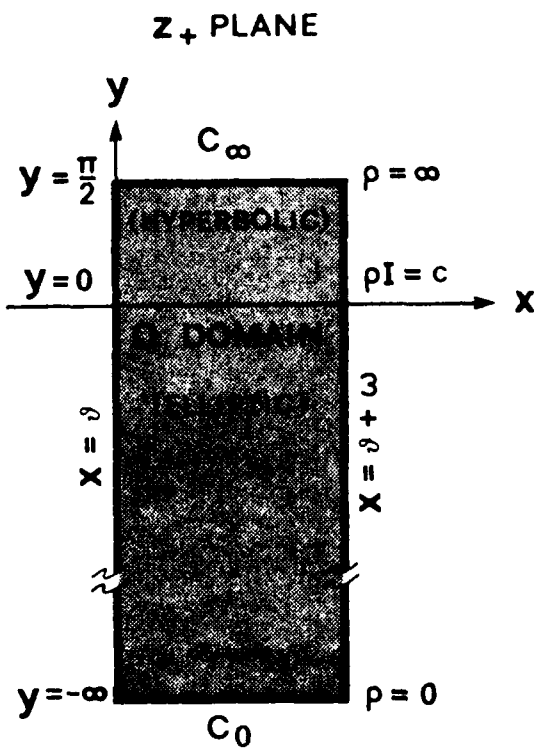


Figure 3-3. Mapping of the wave domain, Ω into the z_+ plane by the characteristic transformation.

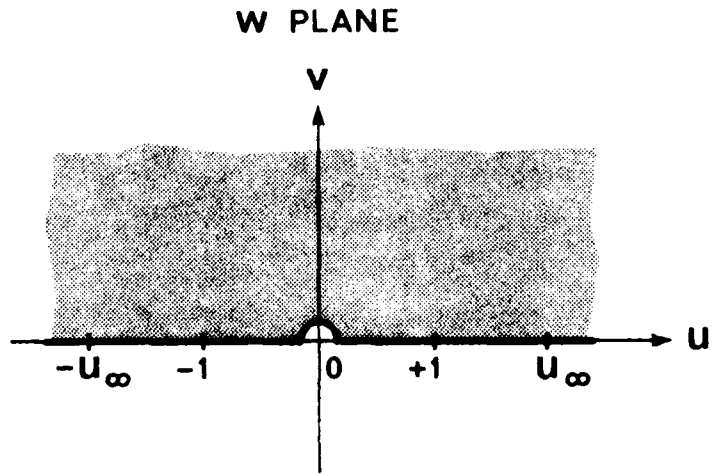


Figure 3-4. Mapping of the wave domain, Ω to the upper half-plane by conformal transformation, $w(z_+)$.

SECTION 4

DISCUSSION AND CONCLUSION

4.1 OVERVIEW

This report has addressed numerical and analytical aspects of wave diffraction from corners common to geologic and topographic structures. The numerical models examined are limited to reentrant corners (angles greater than 180 degrees); however, the mathematical analysis is completely general.

The numerical part has examined accuracy and sensitivity of numerical diffraction to discretization errors. However, a quantitative study of accuracy was only feasible for the relatively unimportant scalar case of SH-wave diffraction. Therefore, as a first major step in evaluating accuracy of P-SV numerical diffractions, the underlying mathematics were studied. The resulting analytical part of the report provides a new mathematical basis for wave diffraction from a generalized model.

4.2 NUMERICAL DIFFRACTION EXPERIMENTS

It is necessary to study elastic corner diffraction using numerical methods, since no analytical solutions are available. However, there are questions regarding accuracy which must first be answered. Discrete numerical wave solutions, using finite differences or finite elements, implicitly assume regularity of the solution. When initial data, boundary data or boundary geometry are discontinuous, the exact solutions may exhibit singularities which are excluded, i.e., not represented adequately, in the numerical solution--without special fixes. This is particularly true at corners, where the tangent exhibits a jump rather than turning continuously, especially when the corner is reentrant. This problem can be clarified by comparing finite element diffractions to existing scalar diffraction solutions.

The results of Section 2.3, comparisons of the Keller-Blank scalar diffraction solutions to SH finite element solutions, show that simple finite element corner models give good results for the predominant diffracted signal. However, the good correlation deteriorates slightly at later time due to discretization errors associated with model roughness on the sloping wedge face. These errors, although insignificant for this early time study, can be further reduced by more refined gridding or skewed elements, as demonstrated. Therefore, these experiments indicate that with no special fixes, finite elements give excellent results for the simplest case of scalar wave diffraction.

The more realistic case of P-SV diffraction is much more complicated than the scalar case since two particle velocity components are necessary to describe the field at each point. Also, the reentrant corner produces a stress singularity at later time, and excites Rayleigh surface waves in addition to diffracted body waves. Since there are no corner solutions for quantitative comparison, finite element simulations of P-SV wave diffraction were simply examined for consistency. One troublesome aspect was graphical display of the vector field. Time histories and surface plots of each component were used but the most successful display approach was the simple vector plot. Vector plots of the velocity field will be used extensively in future two-dimensional simulations.

The final group of calculations examined Rayleigh surface wave diffraction from the corner. This is a particularly interesting physical problem and has been the subject of numerous experiments and approximate analyses. Rayleigh wave diffraction is even more complicated than P-SV diffraction because of precursor body waves, as well as the surface wave's underlying structure. However, the finite element calculations are no more complicated than for plane P- or SV-wave incidence--actually simpler because the Rayleigh source is a pressure pulse acting on only part of the free-surface. Among other results, these calculations show that surface wave transmission is always much stronger than reflection back along the free-surface, even for a vertical face. Furthermore, the SV body wave diffracted into the mesa shadow zone is quite strong for reentrant corners.

The complete set of finite element calculations were performed on a minicomputer (Prime 750). Model size was typically less than 50,000 elements due to limited fast memory size. The number of available elements puts physical limits on frequency resolution of the model. This was seen in the resulting field plots as fairly long wavelet lengths, compared to model size. Some details of interest were therefore missed due to overlapping of incident and reflected or diffracted wavelets--in particular, details near the Rayleigh wave and diffracted SV wave at the surface. This lack of high resolution also tends to produce poor seismograms, since separate arrivals overlap and interfere. The solution to this problem is to perform the calculations on a supercomputer. However, for purposes of this study, the convenience of in-house computing and postprocessing outweighed the inconvenience of accessing a supercomputer on relatively low data rate telephone lines.

4.3 THEORY OF VECTOR WAVE DIFFRACTION

The major contribution of this report is the new mathematical theory of diffraction derived in Section 3. Because the analysis is completely general, in terms of M wedge domains and N wave functions, irrespective of physics, the results apply to a wide variety of unsolved wave diffraction phenomena. These include optical and other electrodynamic phenomena, as well as the baser mechanical phenomena of elastodynamics and acoustics--to which this report is addressed.

The mathematical problem of vector wave diffraction, where two or more wave functions are coupled at the generalized diffractor, has been perplexing and frustrating analysts for well over 100 years. The fundamental difficulty is essential coupling of the wave functions at the diffractor. As a consequence, separable solutions of the wave equations, the basis for much of classical wave theory, fail to satisfy the boundary conditions there.

Non-separable forms based on self-similarity, i.e., homogeneous solutions, are well-known and have been applied successfully to scalar problems--but not to the vector case. The failure is due to an incomplete vector formulation of the problem, rather than any underlying inconsistency in the mathematics. Therefore, it is necessary to completely vectorize the mathematics by expressing the governing partial differential equations as a matrix differential operator acting on a vector unknown, and logically extending the concepts of scalar boundary and initial conditions to the vector case.

With the problem vectorized, solution of the vector wave equation proceeds in much the same way as for the scalar case. It starts by transformation to characteristic coordinates, which is equivalent to diagonalizing the matrix partial differential operator, and ends by a trivial integration, yielding the solution as the sum of two characteristic functions, i.e., functions of the two characteristic matrices.

The real problem then begins, namely, finding particular forms of the characteristic functions satisfying vector boundary conditions on the union of interfaces. These conditions yield a boundary value problem involving N unknown functions in 2N characteristic variables, defined on limit points of the N wave domains.

To express this boundary value problem in a form amenable to analysis, it is necessary to further transform the wave domains so they cover the upper halfplane, with all boundaries mapping to the real axis. This is called the characteristic mapping, because it turns out that real characteristics map entirely to the real axis, effectively vanishing, except for a residual distribution on the axis. Complex characteristics then become the only spatial variables in the problem, whence the $2N$ characteristic variables reduce to N complex variables in the upper halfplane, and their N complex conjugates in the lower halfplane.

Thus, the vector boundary value problem assumes its fundamental form, i.e., given a vector of N analytic functions in N complex variables, find a particular solution satisfying boundary conditions on the real axis. Part of this fundamental form is expressed as three so-called normal boundary value problems, in order to enforce consistency between real and imaginary parts of the N -vector analytic function on the real axis. The remaining part of the problem is the vector boundary condition equation.

By virtue of their definition on the real axis, the normal forms are solved essentially by inspection, using the sifting property of the delta function. This yields all normal solution in terms of a diagonal singular integral operator in the N complex variables. The three normal problems expressing the consistency condition yield an integral transform pair relating real and imaginary parts. The pair can be reduced to a double integral equation by eliminating either the real or imaginary part of the analytic vector function. This yields either part in terms of a double singular integral of itself.

Finally, to solve the original boundary condition equation, the real or imaginary part is eliminated via the integral transform pair. Operating on the resulting integral equation with a suitable integral operator, and replacing the double singular integral yields a standard singular integral equation. This form of the boundary value problem serves as the calculational basis for numerically evaluating vector wave diffraction solutions. The form depends, however, on invertibility of two matrix coefficients in the boundary conditions. When either matrix is non-invertible, i.e., singular,

the problem is degenerate and physics has to be invoked to give a consistent integral equation.

Rather than end the analysis at this level of generality, it was useful to specialize the results to the $N = 2$ canonical problem. This so-called binary problem involves two wave functions in a single wedge, $M = 1$, or one wave function in each of two wedges, $M = 2$. The $M = 1$, problem corresponds to the fundamental P-SV elastodynamic problem examined numerically in Section 2. The $M = 2$ problem would be obtained by adding an SH wave function to the void wedge in the model used to verify numerical solutions of the scalar wave equation in Section 2. The $M = 1$ problem is of principal interest in this work, and is solved rigorously by the above mathematical theory since the boundary matrices are invertible.

4.4 CONCLUSIONS

A number of significant conclusions can be drawn from this work. First, regarding the underlying geophysical problem of diffraction into shadow zones by reentrant corners in highland-lowland topography--the strongest diffractions from the corner are due to the Rayleigh wave incidence. In addition, the observed strong transmission of Rayleigh waves around corners yields secondary diffractions as subsequent corners are encountered.

Second, regarding finite element diffraction calculations--simple Cartesian finite element models appear adequate near the corner for early time, and also near the wavefront, but not for later time (quasistatic) because of an incomplete mathematical formulation there, i.e., no explicit representation of stress singularities in the element shape function. Analytical solutions of P-SV diffraction are necessary to completely validate these results, however.

Third and most important, regarding the new mathematical theory of diffraction--the analysis yields a rigorous, formal solution of diffraction by the generalized diffractor and, in particular, yields a solution for body wave diffraction by a single wedge. This provides the future basis for validating the P-SV numerical diffractions described above, as well as solutions to a number of interesting, unsolved problems in mathematical physics.

REFERENCES

1. Holmes, A. (1965). Principles of Physical Geology, The Ronald Press Co., New York.
2. Keller, H. B. and A. Blank (1951). Diffraction and Reflection of Pulses by Wedges and Corners, Comm. Pure Appl. Math., 4.
3. Vaughan, D. K. (1984). Flex User's Guide, Weidlinger Associates, Palo Alto, CA.

E N D

D TIC

8- 86